U

Ultracold Atomic Gases: Novel States of Matter

Ludwig Mathey[1], Shan-Wen Tsai[2], Antonio H. Castro Neto[3]
[1] Harvard University, Cambridge, USA
[2] University of California, Riverside, USA
[3] Boston University, Boston, USA

Article Outline

Glossary
Definition of the Subject
Introduction
One-Dimensional Lattices
Phase-Locking Transition of Coupled Low-Dimensional Superfluids
Bose–Fermi Mixtures in Two-Dimensional Optical Lattices
Conclusions
Bibliography

Glossary

Bose–Einstein condensation (BEC) Low temperature phase of systems of identical bosons, characterized by superfluidity.

Boson Particles with integer spin $S = 0, 1, 2, \ldots$ Mediators of interactions, such as photons and gluons are bosons. Objects made of an even number of fermions are bosons: positronium (electron + positron), meson (two quarks), ^{87}Rb (37 protons, 48 neutrons and 37 electrons), ^{7}Li (3 protons, 4 neutrons, 3 electrons).

Cooper pairs At low temperatures and for attractive interactions fermions form a superconducting state, in which fermions form pairs which condense.

Fermi surface Since fermions obey Pauli's exclusion principle, the ground state of N non-interacting fermions in d-dimensions is the state with the N lowest energy states occupied. In momentum space the last occupied state and the first unoccupied state define a surface of dimensions $d - 1$, called the Fermi surface.

Fermion Particles with half-odd integer spin $S = 1/2, 3/2, 5/2, \ldots$ Examples include elementary particles such as electrons and quarks. Objects made of an odd number of fermions are also fermionic, such as protons, ^{40}K (19 protons, 21 neutrons, and 19 electrons), and ^{6}Li (3 protons, 3 neutrons, and 3 electrons).

Laser cooling In a typical experimental setup, the atoms are cooled to the regime of $10^2 \mu K$, by using pairs of counterpropagating laser beams that are slightly red-detuned below an atomic transition. Due to the Doppler effect the atoms can only absorb a photon if they travel towards the beam with a high velocity. From that process the atoms experience a recoil, which slows them down.

Evaporative cooling To slow the atoms down further, to the μK regime, one applies radio frequency radiation that flips the internal state to a high-field seeking, i. e. non-trapped, state in such a way, that only atoms of high kinetic energy can escape. Due to thermalization, this leads to cooling of the remaining atomic ensemble.

Magnetic trap The atoms are trapped by applying a spatially inhomogeneous magnetic field. This field leads to an energy shift due to the Zeeman effect, which the atoms experience as an external potential, for large energy splittings of the magnetic levels. Different geometric designs are in use, such as the TOP trap, or the Ioffe–Pritchard trap.

Optical lattice Counterpropagating laser beams create a standing wave field, which the atoms experience as a periodic potential, due to the ac Stark shift. If the temperature and all energy scales are small compared to the energy splitting due the spatial confinement in each well, this system is well approximated by a Hubbard model, i. e. by taking into account nearest-neighbor hopping and on-site interaction.

Nesting Fermi surface with portions that are parallel. The vector that connects different parallel portions is called the nesting vector $\vec{Q}$.

Definition of the Subject

The work presented in this article belongs to the recently emerging interface of atomic physics and condensed matter theory. One of the crucial connections between these fields is the fact that ultra-cold atom ensembles in optical lattices, i. e. periodic potentials provided by standing waves of laser light, are well described by Hubbard models, the quintessential model of many-body theory. Therefore, these experiments allow for the study of many-body effects in a well-defined and tunable environment.

The subject of this article is the study of quantum phases of ultra-cold atoms in optical lattices. The objective is to propose experimental configurations, such as what lattice geometry or which types of atoms to use, for which unusual many-body effects can be found. Besides the applicability to ultra-cold atom systems, and given the generic nature of the underlying models, the resulting phases are also of interest in solid state systems.

Using techniques such as a numerical implementation of functional renormalization group equations and Luttinger liquid theory, we find the phase diagrams of various low-dimensional systems of different geometry, and discuss how the various phases could be detected.

Introduction

The technology of cooling and trapping atomic ensembles has been one of the most important developments in physics over the last decades. It has been a critical ingredient in creating Bose–Einstein condensates [4,14], improving atomic clocks [79], and studying atomic properties [43,55]. A new direction in this development was the realization of the Mott insulator transition [27] with ultra-cold atoms, which demonstrated that these systems can be used to create various types of quantum phases in a tunable and well-defined environment. The subsequent progress that has been made in controlling and manipulating ensembles of ultra-cold atoms [52,58,59,92], was followed by a number of experiments to create and study more and more sophisticated many-body effects, such as fermionic superfluids [28,42,109], one-dimensional strongly correlated Fermi and Bose systems [47,70,77], or noise correlations in interacting atomic systems [3,18,29,61] . These developments established the notion of 'engineering' many-body states in a tunable environment, i. e. manipulating ensembles of ultra-cold atoms in optical lattices.

This article further explores this development. The first step of creating novel states of matter is to determine the phase diagram of the system under consideration. For this purpose we use Luttinger liquid theory for studying one-dimensional quantum systems and two-dimensional thermal systems, and functional renormalization group equations to study two-dimensional quantum systems, which are both sophisticated methods that generate a lot of insight into the physics of these systems.

This article contains three main sections, which can be read independently of each other, organized as follows: In Sect. "One-Dimensional Lattices" we first study the phase diagram of an incommensurate Bose–Fermi mixture in one dimension, which can be understood as a Luttinger liquid of polarons (see [60,64]). We then broaden the scope of this study to include the effects of commensurate densities (see [63]). In Sect. "Phase-Locking Transition of Coupled Low-Dimensional Superfluids", we study the phases of two coupled two-dimensional superfluids, and we propose how the phase-locking transition of such systems can be used to realize the Kibble–Zurek mechanism, i. e. to create topological defects by ramping across a phase transition (see [66]). In Sect. "Bose–Fermi Mixtures in Two-Dimensional Optical Lattices", we use a numerical implementation of functional renormalization group equations to study the phase diagrams of Bose–Fermi mixtures in optical lattices in two dimensions. For both, a square and a triangular lattice, we find a rich structure of competing phases (see [50,62,65]).

One-Dimensional Lattices

The theory of one-dimensional many-body systems has been a highly active and fascinating field of physics for many decades, the centerpiece of which is the notion of the Luttinger liquid [22,24,90]. In this section, we propose several systems that display various features of Luttinger liquids, such as quasi-long range order, competing orders, and Kosterlitz–Thouless transitions due to commensurate densities, as will be explained.

Recent advances in controlling ultra-cold atoms lead to the realization of truly one-dimensional systems, and the study of many-body effects therein. Important benchmarks, such as the Tonks–Girardeau gas [47,77] and the Mott transition in one dimension [92], have been achieved by trapping bosonic atoms in tight tubes formed by an optical lattice potential. Novel transport properties of one-dimensional lattice bosons have been studied using these techniques [17]. More recently, a strongly interacting one-dimensional Fermi gas was realized using similar trapping methods [70]. Interactions between the fermion atoms were controlled by tuning a Feshbach resonance in these experiments. On the theory side, numerous proposals were given for realizing a variety of different phases in ultra-cold Fermi systems [10,19,83], Bose–

Fermi mixtures [9,60,64,88], as well as Bose–Bose mixtures [37,38].

In the first part of this section, we describe the phase diagram of an incommensurate Bose–Fermi mixture, in the second part we consider the effect of commensurate fillings.

Luttinger Liquid of Polarons in One-Dimensional Bose–Fermi Mixtures

In this section we investigate one-dimensional (1D) Bose–Fermi mixtures (BFM) using bosonization [8,32]. The resulting quantum phases can be understood by introducing polarons, i. e. atoms of one species surrounded by screening clouds of the other species. In our analysis the polarons emerge as the most well-defined quasi-particles in the interacting system while quantum phases of the system arise from a competition of various ordering instabilities of such polarons. The phase diagrams we obtain show a remarkable similarity to the Luttinger liquid phase diagrams of 1D interacting electron systems [90,102], suggesting that 1D BFM may be understood as Luttinger liquids of polarons.

To illustrate the results of this section, we show a typical phase diagram for a BFM in an optical lattice in Fig. 1, as a function of experimentally controlled parameters. We consider two types of atoms, one fermionic and one bosonic, moving in a lattice potential with the amplitude $V_{b,\parallel}$ (see [64]), and interacting via a short-ranged interaction characterized by the scattering length a_{bf} between bosons and fermions. We use these parameters, the scattering length a_{bf} and the strength of the longitudinal optical lattice for bosonic atoms ($V_{b,\parallel}$)[1], as tuning parameters in Fig. 1. For relatively weak interactions and slow bosons (i. e. large $V_{b,\parallel}$) the system is in the charge-density-wave (CDW) phase, in which the densities of fermions and bosons have a periodic modulation[2]. For very strong interactions the system is unstable to phase separation (PS) [1,7,9]. The two regimes are separated by a p-wave pairing phase of fermionic polarons (f-PP). Our analysis is carried out for the most promising system of atoms in an optical lattice. However, qualitative results should also apply to atoms in a tight 1D cigar-shaped magnetic trap [23]. A sketch of the two phases is shown in Fig. 2.

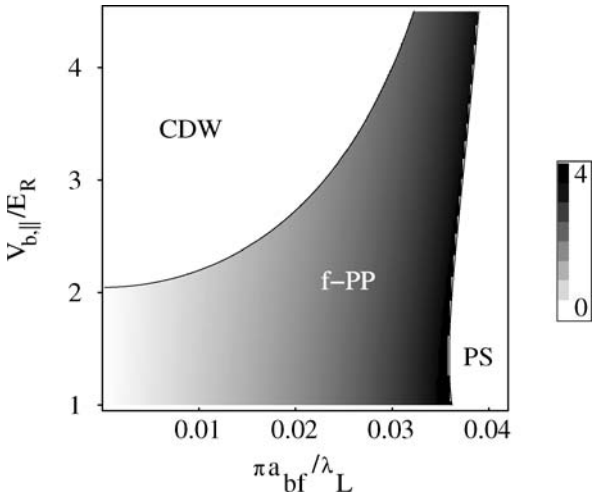

Ultracold Atomic Gases: Novel States of Matter, Figure 1
Phase diagram for a mixture of bosonic and spinless fermionic atoms in a 1D optical lattice. *Shading* in the f-PP phase describes the strength of the bosonic screening cloud (2λ, see Eq. (4)) around a pair of fermions. λ_L and E_R are respectively the lattice period and recoil energy. Other parameters used for this figure are (see text for notations, [64] for details): $\nu_b = 4$, $\nu_f = 0.5$, $V_{b,\perp} = V_{f,\perp} = 20E_R$, $V_{f,\parallel} = 2E_R$, boson-boson scattering length $a_{bb} = 0.01\lambda_L$

The essence of the bosonization procedure is to diagonalize the effective low-energy Hamiltonian, which allows for the exact calculation of all relevant correlation functions. The phase diagrams are determined by finding the order parameter which has the most divergent susceptibility [90,102]. Bosonization approach has been applied to BFM in [9]. However, that work did not consider the formation of polarons and, as a result, did not describe most of the quantum phases discussed here. The present system also has a close analogy to 1D electron–phonon systems discussed previously (see e. g. [101]). A qualitative difference of the electron–phonon system is that the sound velocity is usually much smaller than the Fermi velocity, whereas for a BFM the velocity of the phonon modes (of the bosonic condensate) can be larger than the Fermi velocity. We also note that the 1D p-wave superfluid we obtain here may be of relevance to a recent proposal for quantum computation [48].

We now give an overview over the, somewhat technical, derivation of this phase diagram, before we discuss issues concerning the experimental realization and detection of these phases, and conclude. We consider a mixture of spinless fermionic (f) and bosonic (b) atoms. For a sufficiently strong optical potential the microscopic

[1] In this paper, we use $V_{f/b,\parallel(\perp)}$ to denote the optical lattice potential experienced by fermionic/bosonic atoms in the longitudinal (perpendicular) directions. Independent tuning of the optical lattices for two species of atoms can be achieved even with a single pair of lasers by controlling the laser detuning and intensity separately.

[2] We note that in a homogeneous 1D system only quasi-long-range order for CDW phase is possible. However, the inhomogeneous trap boundary in a realistic experiment can pin the CDW phase to generate a true density modulation.

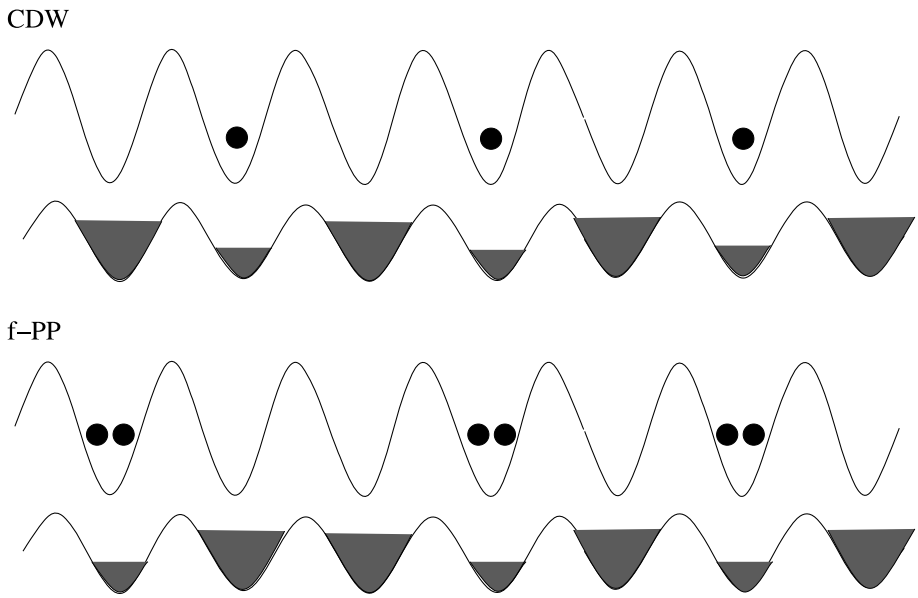

Ultracold Atomic Gases: Novel States of Matter, Figure 2
Illustration of the two phases that occur in a BFM with spinless fermions, CDW and *f*-PP. In the CDW phase the system develops a $2k_f$ density modulation in both the fermionic and the bosonic liquid. In the *f*-PP phase, the fermions form polarons, indicated by the reduced bosonic density in their vicinity, that is, their polarization cloud. This polarization leads to an effective attractive interaction, which causes these fermionic polarons to pair up and form a superfluid state

Hamiltonian is given by a single band Hubbard model

$$H = -\sum_{\langle ij\rangle}\left(t_b b_i^\dagger b_j + t_f f_i^\dagger f_j\right) - \sum_i \left(\mu_f n_{f,i} + \mu_b n_{b,i}\right) + \frac{U_b}{2}\sum_i n_{b,i}(n_{b,i}-1) + U_{bf}\sum_i n_{b,i} n_{f,i}\,, \quad (1)$$

where $n_{b/f,i}$ are the boson/fermion density operators with $\mu_{b/f}$ being their chemical potentials. The tunneling amplitudes $t_{f/b}$, and the particle interactions U_b and U_{bf} can be expressed explicitly in terms of the *s*-wave scattering lengths, the laser beam intensities and atomic masses [39]. For simplicity we assume that the filling fraction of fermions $\nu_f \equiv \langle n_{f,i}\rangle$ is not commensurate with the lattice or with the filling fraction of bosons ν_b. Therefore, we can neglect lattice-assisted backward/Umklapp scattering. The Fermi momentum and velocity are given by $k_f = \pi\nu_f$ and $v_f = 2t_f \sin(k_f)$, respectively.

In Haldane's bosonization approach [8,32] 1D fermion and boson operators can be represented by $f(x) = [\nu_f + \Pi_f]^{1/2}\sum_{m=-\infty}^{\infty} e^{(2m+1)i\Theta_f} e^{i\Phi_f}$ and $b(x) = [\nu_b + \Pi_b]^{1/2}\sum_{m=-\infty}^{\infty} e^{2mi\Theta_b} e^{i\Phi_b}$, where x is a continuous coordinate that replaces the site index i. The operators $\Pi_{f/b}(x)$ and $\Phi_{f/b}(x)$ are the bosonized density and phase fluctuation operators. The $\Theta_{f/b}(x)$ fields are given by $\Theta_{f/b} \equiv \pi\nu_{f/b}x + \pi\int^x dy\,\Pi_{f/b}(y)$. The low-energy effective Hamiltonian thus can be written as:

$$H_{eff} = \sum_{\alpha=b,f}\frac{v_\alpha}{2}\int dx\left[\frac{K_\alpha}{\pi}(\partial_x\Phi_\alpha)^2 + \frac{\pi}{K_\alpha}\Pi_\alpha^2\right] + U_{bf}\int dx\,\Pi_b\Pi_f + \frac{2G}{2\pi}\int dx\left[\pi^2\Pi_f^2 - (\partial_x\Phi_f)^2\right]. \quad (2)$$

where v_b and K_b are the phonon velocity and Luttinger exponent of the bosons and $K_f = 1$ for noninteracting fermion atoms.

To obtain the last term of H_{eff} we have integrated out the high energy ($2k_f$) phonons within the instaneous approximation (i. e. assuming $v_b \gg v_f$). $G \equiv g_{2k_f}^2/\omega_{2k_f}$, where ω_k is the (Bogoliubov) phonon energy dispersion [98] and $g_k = U_{bf}\sqrt{\nu_b\,\varepsilon_{b,k}/2\pi\omega_k}$ is the fermion–phonon (FP) coupling vertex with $\varepsilon_{b,k}$ being the noninteracting boson band energy. In the long wavelength limit we have a conventional FP coupling $g_k = g|k|^{1/2}$ with $g \equiv U_{bf}\sqrt{K_b}/2\pi$. The effective Hamiltonian, Eq. (2), is quadratic and can be diagonalized [16]. The resulting two eigenmode velocities are given by [9]

$$v_{a,A}^2 = \frac{1}{2}(v_b^2 + \tilde{v}_f^2) \pm \frac{1}{2}\sqrt{(v_b^2 - \tilde{v}_f^2)^2 + 16\tilde{g}^2 v_b \tilde{v}_f}\,, \quad (3)$$

where $\tilde{v}_f \equiv (v_f^2 - 4G^2)^{1/2}$ and $\tilde{g} \equiv g\,e^\theta$ with $e^\theta = ((v_f - 2G)/(v_f + 2G))^{1/4}$. When the FP coupling g becomes suf-

ficiently strong the eigenmode velocity v_A becomes imaginary, indicating an instability of the system. This instability corresponds to phase separation (global collapse) for positive (negative) $U_{\rm bf}$ [9].

To understand the nature of the many-body state of BFM outside of the instability region we analyze the long distance behavior of the correlation functions. For the bare bosonic and fermionic particles we find $\langle b(x)b^\dagger(0)\rangle \sim |x|^{-\frac{1}{2}K_\epsilon^{-1}}$ and $\langle f(x)f^\dagger(0)\rangle \sim \cos(k_{\rm f}x)|x|^{-\frac{1}{2}(K_\beta+K_\gamma^{-1})}$ [3]. To describe particles dressed by the other species we introduce the composite operators

$$\tilde{f}(x) \equiv {\rm e}^{-i\lambda\Phi_{\rm b}(x)}f(x)\,, \quad \tilde{b}(x) \equiv {\rm e}^{-i\eta\Phi_{\rm f}(x)}b(x)\,, \qquad (4)$$

with λ and η being some real numbers. The correlation functions of these operators are given by $\langle\tilde{f}(x)\tilde{f}^\dagger(0)\rangle \sim \cos(k_{\rm f}x)|x|^{-\frac{1}{2}(K_\beta+\lambda^2K_\epsilon^{-1}+K_\gamma^{-1}-2\lambda K_{\gamma\epsilon}^{-1})}$ and $\langle\tilde{b}(x)\tilde{b}^\dagger(0)\rangle \sim |x|^{-\frac{1}{2}(K_\epsilon^{-1}+\eta^2K_\gamma^{-1}-2\eta K_{\gamma\epsilon}^{-1})}$ [3]. We observe that the exponents of the correlation functions are maximized for $\lambda_{\rm c} = K_\epsilon/K_{\gamma\epsilon}$ and $\eta_{\rm c} = K_\gamma/K_{\gamma\epsilon}$. From now on we will use Eq. (4) with $\lambda_{\rm c}$ and $\eta_{\rm c}$ to construct polaronic particles. In the limit of weak interactions we have $\lambda_{\rm c} \to U_{\rm bf}/U_{\rm b}$ and $\eta_{\rm c} \to 2U_{\rm bf}/\pi v_{\rm b}$. This result can be understood by a simple density counting argument that a fermionic polaron (f-polaron) locally suppresses (enhances) a bosonic cloud by $\lambda_{\rm c}$ particles, whereas a bosonic polaron (b-polaron) depletes (enhances) the fermionic system by $\eta_{\rm c}$ atoms for positive (negative) g.

The polaronic operators defined in Eq. (4) can also be introduced via the canonical polaron transformation (CPT), which is often used in polaron theory [2,57]. The CPT operator is given by $U = {\rm e}^{-i\lambda\sum_{k\neq0}(F_k\beta_k\rho_k^\dagger+{\rm h.c.})}$, where β_k is the phonon annihilation operator, ρ_k is the fermion density operator, F_k is some function of wavevector k, and λ specifies the strength of the phonon dressing. When applied to a fermion operator, the CPT transforms it to a polaron operator, $U^{-1}f(x)U = f(x)\exp[-i\lambda\sum_{k\neq0}(F_k\beta_k{\rm e}^{-ik\cdot x}+{\rm h.c.})]$ [2,57], which is the same as Eq. (4), provided that one takes $F_k = \sqrt{2\pi/(K_{\rm b}|k|L)}\,{\rm sgn}(k)$. (Note that in 1D fermionic systems density operators correspond to Luttinger bosons.) We note, however, unlike in ordinary polaron theory, where further approximations after the CPT have to be made [2,57], in the 1D BFM system we consider here, the full low energy quantum fluctuations have been included via bosonization method and exact diagonalization of the resulting Hamiltonian Eq. (2). This allows for an essentially exact determination of the polarization parameter λ.

Now we study the many-body ground state phase diagram of a 1D BFM, which is characterized by specifying the order parameters that have the slowest long distance decay of the correlation functions [90,102]. Two types of ordering were found to occur: $2k_{\rm f}$-ordering due to a Peierls-type instability and f-polaron pairing due to their effective attractive interactions induced by the screening clouds, see Fig. 2. For the $2k_{\rm f}$ CDW order parameter, $O_{\rm CDW} = f_{\rm L}^\dagger f_{\rm R}$, we find $\alpha_{\rm CDW} = 2 - 2K_\beta$, and for the f-polaron pairing field, $O_{f-{\rm PP}} = \tilde{f}_{\rm L}\tilde{f}_{\rm R}$, we obtain $\alpha_{f-{\rm PP}} = 2 - 2[\lambda_{\rm c}^2K_\epsilon^{-1} + K_\gamma^{-1} - 2\lambda_{\rm c}K_{\gamma\epsilon}^{-1}]$. We did not include polaron dressing in $O_{\rm CDW}$, since this operator has no net fermionic charge and the exponent of $O_{\rm CDW}$ does not change if we replace f by $\tilde{f}$. Scaling exponents shown in Fig. 3a demonstrate that divergencies of the CDW and f-PP susceptibilities (corresponding to positive α) are mutually exclusive and cover the entire phase diagram outside the PS regime. In the same figure, we also show the scaling exponents calculated for bare fermion pairing ($O_{BFP} = f_{\rm L}f_{\rm R}$), bare boson condensate ($O_{BB} = b$), and b-polaron condensate ($O_{{\rm b}-P} = \tilde{b}$). It is easy to see that the polaronic order parameters always have larger exponents than their counterparts constructed with bare atoms, showing the stability of polaronic quasi-particle in a 1D BFM system. Moreover, the necessity to consider f-polaron pairing instead of bare fermion pairing is further supported by considering the stability of superfluidity: we introduce a single weak impurity potential in the 1D BFM and determine its relevance by a renormalization group (RG) calculation [44]. We find that the impurity potential is relevant within the CDW phase and irrelevant outside of it. This indicates that there should be a superfluid phase outside of the insulating CDW phase, which supports the existence of f-polaron pairing instead of bare fermion pairing according to Fig. 3a.

In Fig. 3b we show a global phase diagram of a BFM considering the FP coupling (g) and effective fermion–fermion interaction (G) as independent variables. One can see that the polaronic effects and the associated pairing phase are important when FP coupling (g) is large, while the CDW phase dominates when the effective fermion interaction (G) is increased. This phase diagram is very similar to what one finds for spinless electrons in Luttinger liquid theory [90,102], where CDW and pairing phase compete with each other in the whole phase diagram. Therefore one can introduce a Luttinger liquid of

[3] Here we defined $K_\beta \equiv {\rm e}^{2\theta}\tilde{v}_{\rm f}(\cos^2\psi/v_A + \sin^2\psi/v_{\rm a})$, $K_\delta \equiv K_{\rm b}v_{\rm b}(\sin^2\psi/v_A + \cos^2\psi/v_{\rm a})$, $K_\gamma^{-1} \equiv {\rm e}^{-2\theta}/\tilde{v}_{\rm f}(v_A\cos^2\psi + v_{\rm a}\sin^2\psi)$, $K_\epsilon^{-1} \equiv K_{\rm b}^{-1}/v_{\rm b}(v_A\sin^2\psi + v_{\rm a}\sin^2\psi)$, $K_{\beta\delta} = {\rm e}^\theta\sqrt{K_{\rm b}\tilde{v}_{\rm f}v_{\rm b}}\sin(2\psi)/2(1/v_{\rm a} - 1/v_A)$, and $K_{\gamma\epsilon}^{-1} = {\rm e}^{-\theta}/\sqrt{K_{\rm b}\tilde{v}_{\rm f}v_{\rm b}}\sin(2\psi)/2(v_{\rm a} - v_A)$. ψ is given by $\tan 2\psi = 4\tilde{g}(v_{\rm b}\tilde{v}_{\rm f})^{1/2}/(v_{\rm b}^2 - \tilde{v}_{\rm f}^2)$. These expressions are obtained from diagonalizing $H_{\rm eff}$. For details see [64].

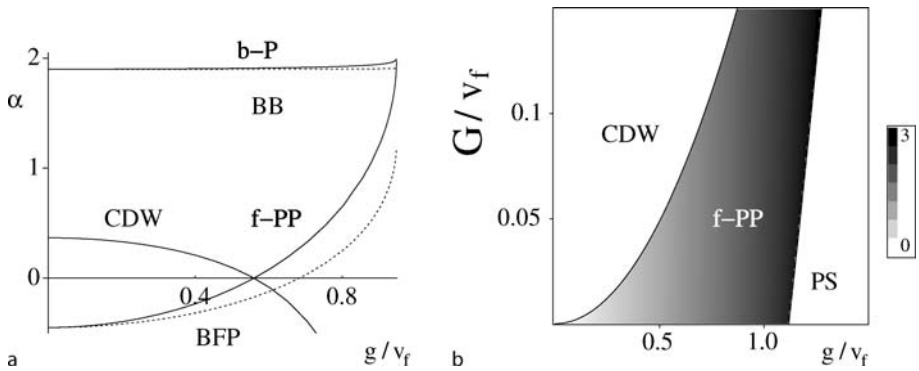

Ultracold Atomic Gases: Novel States of Matter, Figure 3

Ground state of a BFM with spinless fermions. a Scaling exponents of different order parameters (see the text). Parameters are chosen to be $v_b/v_f = 3$, $K_b = 5$ and $G/v_f = 0.1$. b Global phase diagram for $v_b/v_f = 5$ and $K_b = 10$. *Shading* density indicates the strength of the screening clouds of a polaron pair, $2\lambda_c$

polarons to describe BFM in 1D systems. The phase diagram in terms of experimentally controlled parameters was shown in Fig. 1. When considering finite temperature effects in a realistic experiment, we note that the correlation function is cut-off by thermal correlation lengths, which are approximately given by $\xi \sim v_f/k_B T$. Therefore the zero temperature ground states should appear when $\xi > L$ with L being the system size. This corresponds to a temperature regime of 1% of the Fermi temperature for systems of approximately 100 sites in the longitudinal direction.

Several approaches can be used to detect the quantum phases discussed above. First, in the CDW phase the fermion density modulation will induce a $2k_f$ density wave in the boson field in addition to the zero momentum condensation so that the CDW phase can be observed as interference peaks at momentum $k = 2k_f$ in a standard time-of-flight (TOF) measurement for bosons[4]. Secondly, the polaron pairing phase can be observed by measuring the noise correlation of fermions in a TOF experiment as proposed in [3]. Thirdly, a laser stirring experiment [72,82] can be used to probe the phase transition between the insulating (pinned by trap potential) CDW and the superfluid f-PP phase: one can use a laser beam focused at the center of the cloud and stir such local potential to measure the response of the BFM. If the system is in the pairing phase, the laser beam can be moved through the system without dissipation if only its velocity is slower than some critical value [72,82]. At the f-PP/CDW phase boundary this critical velocity goes to zero, reflecting a transition to the insulating (CDW) state. This scenario follows from the above described RG analysis of a single impurity potential [44]. Finally, a way to probe the PS boundary could be to measure the dipolar collective oscillations of the system, generated by a sudden displacement of the harmonic trap potential with respect to the lattice potential [21,56,100]. When the system is near the PS boundary, fermion–boson interaction will strongly reduce the frequency of the dipolar mode.

In summary, we used bosonization to investigate the quantum phases of 1D mixtures of bosonic and fermionic atoms involving spinless fermions. The phase diagram that we found can be understood in terms of a Luttinger liquid of polarons. We also described several experimental techniques for probing these quantum phases.

Commensurate Mixtures of Ultra-Cold Atoms in One Dimension

In this section we explore the behavior of ultra-cold atomic mixtures, confined to one-dimensional (1D) motion in an optical lattice, that exhibit different types of commensurability, by which we mean that the atomic densities and/or the inverse lattice spacing have an integer ratio. Commensurable fillings arise naturally in many ultra-cold atom systems, because the external trap potential approximately corresponds to a sweep of the chemical potential through the phase diagram, and therefore passes through points of commensurability. At these points the system can develop an energy gap, which fixes the density commensurability over a spatially extended volume. This was demonstrated in the celebrated Mott insulator experiment by Greiner et al. [27], where Mott phases with integer filling occurred in shell-shaped regions in the atom trap. These gaped

[4]We note that in a homogeneous 1D system only quasi-long-range order for CDW phase is possible. However, the inhomogeneous trap boundary in a realistic experiment can pin the CDW phase to generate a true density modulation.

phases gave rise to the well-known signature in the time-of-flight images[5], and triggered the endeavor of 'engineering' many-body states in optical lattices. Further examples include the recently created density-imbalanced fermion mixtures [78,110] in which the development of a balanced, i. e. commensurate, mixture at the center of the trap is observed.

In 1D, this phenomenon is of particular importance, because it is the only effect that can lead to the opening of a gap, for a system with short-range interactions. In contrast to higher-dimensional systems, where, for instance, pairing can lead to a state with an energy gap, in 1D only discrete symmetries can be broken, due to the importance of fluctuations. Orders that correspond to a continuous symmetry can, at most, develop quasi long range order (QLRO), which refers to a state in which an order parameter $O(x)$ has a correlation function with algebraic scaling, $\langle O(x)O(0)\rangle \sim |x|^{-(2-\alpha)}$, with a positive scaling exponent α.

Due to its importance in solid state physics, the most thoroughly studied commensurate 1D system is the SU(2) symmetric system of spin-1/2 fermions. This system develops a spin gap for attractive interaction and remains gapless for repulsive interaction, as can be seen from a second order RG calculation. However, the assumed symmetry between the two internal spin states, which is natural in solid state systems, does not generically occur in Fermi–Fermi mixtures (FFMs) of ultra-cold atoms, where the 'spin' states are in fact different hyperfine states of the atoms. An analysis of the generic system is therefore highly called for. Furthermore, we will extend this analysis to both Bose–Fermi (BFMs) and Bose–Bose mixtures (BBMs), as well as to the dual commensurability, in which the charge field, and not the spin field, exhibits commensurate filling, as will be explained below.

The main results of this section are the phase diagrams shown in Figs. 4 and 5. We find that both attractive and repulsive interactions can open an energy gap. For FFMs the entire phase diagram is gaped, except for the repulsive SU(2) symmetric regime (cf. [10]), for BFMs or BBMs the bosonic liquid(s) need(s) to be close to the hard-core limit, otherwise the system remains gapless. Furthermore, we find a rich structure of quasi-phases, including charge and spin density wave order (CDW, SDW), singlet and triplet pairing (SS, TS), polaron pairing [60,64], and a supersolid phase, which is the first example of a supersolid phase in 1D. These results are derived within a Luttinger liquid (LL) description, which treats bosonic and fermionic liquids on equal footing.

We will now classify the types of commensurability that can occur in a system with short-ranged density–density interaction. We consider Haldane's representation [8,32] of the densities for the two species:

$$n_{1/2} = [\nu_{1/2} + \Pi_{1/2}] \sum_m \mathrm{e}^{2mi\Theta_{1/2}} \,. \tag{5}$$

ν_1 and ν_2 are the densities of the two liquids, $\Pi_{1/2}(x)$ are the low-k parts (i. e. $k \ll 1/\nu$) of the density fluctuations; the fields $\Theta_{1/2}(x)$ are given by $\Theta_{1/2}(x) = \pi\nu_{1/2}x + \theta_{1/2}(x)$, with $\theta_{1/2}(x) = \pi\int^x \mathrm{d}y\Pi_{1/2}(y)$. These expressions hold for both bosons and fermions. If we use this representation in a density–density interaction term $U_{12}\int \mathrm{d}x n_1(x)n_2(x)$, we generate to lowest order a term of the shape $U_{12}\int \mathrm{d}x\Pi_1(x)\Pi_2(x)$, but in addition an infinite number of nonlinear terms, corresponding to all harmonics in the representation. However, only the terms for which the linear terms $(2\pi m_{1/2}\nu_{1/2}x)$ cancel, can drive a phase transition. For a continuous system this happens for $m_1\nu_1 - m_2\nu_2 = 0$, whereas for a system on a lattice we have the condition $m_1\nu_1 - m_2\nu_2 = m_3$, where m_1, m_2 and m_3 are integer numbers. In general, higher integer numbers correspond to terms that are less relevant, because the scaling dimension of the non-linear term scales quadratically with these integers. We are therefore lead to consider small integer ratios between the fillings and/or the lattice if present. In [64], we considered two cases of commensurabilities: A Mott insulator transition coupled to an incommensurate liquid, and a fermionic liquid at half-filling coupled to an incommensurate bosonic liquid. In both cases the commensurability occurs between one species and the lattice, but does not involve the second species. Here, we consider the two most relevant, i. e. lowest order, cases which exhibit a commensurability that involves both species. The first case is the case of equal filling $\nu_1 = \nu_2$, the second is the case of the total density being unity, i. e. $\nu_1 + \nu_2 = 1$, where the densities ν_1 and ν_2 themselves are incommensurate. The first case can drive the system to a spin-gaped state, the second to a charge gaped state. We will determine in which parameter regime these transitions occur, and what type of QRLO the system exhibits in the vicinity of the transition. These two cases can be mapped onto each other via a dual mapping, which enables us to study only one case and then infer the results for the second by using this mapping. We will write out our discussion for the case of equal filling and merely state the corresponding results for complementary filling.

[5] Due to the confining trap the transition is, while visible, 'blurred' into a gradual cross-over, due to finite size effects, and, more importantly, due to the coexistence of several phases in the trap. This can also be expected for the phase transitions predicted in this paper.

The action of a two-species mixture with equal filling in bosonized form is given by:

$$S = S_{0,1} + S_{0,2} + S_{12} + S_{\text{int}} \,. \tag{6}$$

The terms $S_{0,j}$, with $j = 1, 2$, are given by

$$S_{0,j} = \frac{1}{2\pi K_j} \int \mathrm{d}^2 r \Big(\frac{1}{v_j} (\partial_\tau \theta_j)^2 + v_j (\partial_x \theta_j)^2 \Big) \,. \tag{7}$$

Each of the two types of atoms, regardless of being bosonic or fermionic, are characterized by a Luttinger parameter $K_{1/2}$ and a velocity $v_{1/2}$. Here we integrate over $\mathbf{r} = (v_0 \tau, x)$, where we defined the energy scale $v_0 = (v_1 + v_2)/2$. The term S_{12} describes the acoustic coupling between the two species, and is bilinear:

$$S_{12} = \frac{U_{12}}{\pi^2} \int \mathrm{d}^2 r \partial_x \theta_1 \partial_x \theta_2 + \frac{V_{12}}{\pi^2} \int \mathrm{d}^2 r \partial_\tau \theta_1 \partial_\tau \theta_2 \,. \tag{8}$$

The second term is created during the RG flow; its prefactor therefore has the initial value $V_{12}(0) = 0$. We define $S_0 = S_{0,1} + S_{0,2} + S_{12}$, which is the diagonalizable part of the action. S_{int} corresponds to the non-linear coupling between the two liquids, which we study within an RG approach:

$$S_{\text{int}} = \frac{2 g_{12}}{(2\pi\alpha)^2} \int \mathrm{d}^2 r \cos(2\theta_1 - 2\theta_2) \,. \tag{9}$$

This bosonized description applies to a BBM, a BFM, and a FFM. Depending on which of these mixtures we want to describe we either construct bosonic or fermionic operators according to Haldane's construction [8,32]:

$$f/b = [v_0 + \Pi]^{1/2} \sum_{m \text{ odd/even}} \mathrm{e}^{mi\Theta} \mathrm{e}^{i\Phi} \,. \tag{10}$$

v_0 is the zero-mode of the density, $\Phi(x)$ is the phase field, which is the conjugate field of the density fluctuations $\Pi(x)$. The action for a mixture with complementary filling, $\nu_1 + \nu_2 = 1$, is of the form $S_0 + S'_{\text{int}}$, where the interaction S'_{int} is given by:

$$S'_{\text{int}} = \frac{2 g_{12}}{(2\pi\alpha)^2} \int \mathrm{d}^2 r \cos(2\theta_1 + 2\theta_2) \,. \tag{11}$$

To map the action in Eq. (6) onto this system we use the mapping: $\theta_2 \to -\theta_2$, $\phi_2 \to -\phi_2$, and $g_{12} \to -g_{12}$, which evidently maps a mixture with complementary filling and attractive (repulsive) interaction and onto a mixture with equal filling with repulsive (attractive) interaction.

To study the action given in Eq. (6), we perform an RG calculation along the lines of the treatment of the sine-Gordon model in [24,51]. In our model, a crucial modification arises: The linear combination $\theta_1 - \theta_2$, that appears in the non-linear term, is not proportional to an eigenmode of S_0, and therefore the RG flow does not affect only one separate sector of the system, as in an SU(2)-symmetric system. The RG scheme that we use here proceeds as follows: First, we diagonalize S_0 through the transformation (see [63]) $\theta_1 = B_1 \tilde{\theta}_1 + B_2 \tilde{\theta}_2$, and $\theta_2 = D_1 \tilde{\theta}_1 + D_2 \tilde{\theta}_2$, where $B_{1/2}$ and $D_{1/2}$ are some coefficients, and $\tilde{\theta}_{1/2}$ are the eigenmode fields with velocities $\tilde{v}_{1/2}$. Now we introduce an energy cut-off Λ on $\tilde{\theta}_{1/2}$ according to $\omega^2/\tilde{v}_{1/2} + \tilde{v}_{1/2} k^2 < \Lambda^2$. We shift this cut-off by an amount $\mathrm{d}\Lambda$, and correct for this shift up to second order in g_{12}. At first order, only g_{12} is affected, its flow equation is given by:

$$\frac{\mathrm{d} g_{12}}{\mathrm{d} l} = \Big(2 - K_1 - K_2 - \frac{2}{\pi} \frac{U_{12} + V_{12} v_1 v_2}{v_1 + v_2} \Big) g_{12} \,, \tag{12}$$

with $\mathrm{d}l = \mathrm{d}\Lambda/\Lambda$. At second order several terms are created that are quadratic in the original fields θ_1 and θ_2. We undo the diagonalization, and absorb these terms into the parameters of the action, which concludes the RG step. By iterating this procedure we obtain these flow equations at second order in g_{12}:

$$\frac{\mathrm{d} K_{1/2}}{\mathrm{d} l} = -\frac{g_{12}^2}{16\pi^2} \Big(2 + \Big(\frac{v_2}{v_1} + \frac{v_1}{v_2} \Big) \Big) \,, \tag{13}$$

$$\frac{\mathrm{d} v_1}{\mathrm{d} l} = v_1 \frac{g_{12}^2}{16\pi^2} \Big(\frac{v_2}{v_1} - \frac{v_1}{v_2} \Big) \,, \tag{14}$$

$$\frac{\mathrm{d} v_2}{\mathrm{d} l} = v_2 \frac{g_{12}^2}{16\pi^2} \Big(\frac{v_1}{v_2} - \frac{v_2}{v_1} \Big) \,, \tag{15}$$

$$\frac{\mathrm{d} U_{12}}{\mathrm{d} l} = -\frac{g_{12}^2}{8\pi} (v_1 + v_2) \,, \tag{16}$$

$$\frac{\mathrm{d} V_{12}}{\mathrm{d} l} = -\frac{g_{12}^2}{8\pi} (1/v_1 + 1/v_2) \,. \tag{17}$$

The system of differential equations, Eqs. (12) to (17), can show two types of qualitative behavior: The coefficient g_{12} of the non-linear term (9) can either flow to zero, i. e. S_{int} is irrelevant, or it diverges, leading to the formation of an energy gap. In the first case, the system flows to a fixed point that is described by a renormalized diagonalizable action of the type S_0, from which the quasi-phases can be determined.

When S_{int} is relevant, we introduce the fields [102] $\theta_{\rho/\sigma} = \frac{1}{\sqrt{2}} (\theta_1 \pm \theta_2)$, which define the charge and the spin sector of the system. In this regime, these sectors decouple. Each of the two sectors is characterized by a Luttinger parameter and a velocity, $K_{\rho/\sigma}$ and $v_{\rho/\sigma}$, which are related to

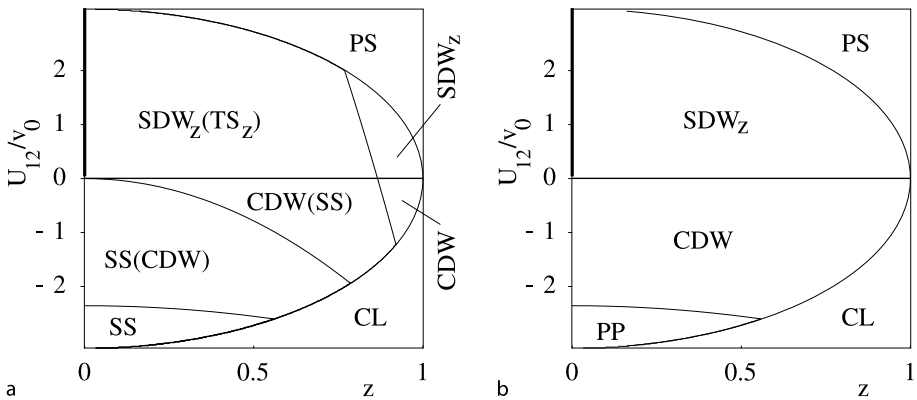

Ultracold Atomic Gases: Novel States of Matter, Figure 4

a Phase diagram of a commensurate FFM or a BBM of hardcore bosons (with the replacement $TS_z \rightarrow SS$), b phase diagram of a BFM with hardcore bosons, in terms of the interaction U_{12} and the parameter $z = |v_1 - v_2|/(v_1 + v_2)$. For both attractive and repulsive interactions a spin gap opens, except for $z = 0$ and positive interaction. In the attractive regime, a FFM or a BBM shows either singlet pairing or CDW order, or a coexistence of these phases, a BFM shows either CDW order or polaron pairing. For repulsive interaction all mixtures show SDW ordering, with FFMs and BBMs showing subdominant triplet or singlet pairing, respectively, for a large range of z. In the gapless regime, a FFM shows degenerate SDW and CDW order, a BFM shows CDW order for the fermions and SF for the bosons, and a BBM shows SF with subdominant CDW, i. e. supersolid behavior. For very large positive values of U_{12} the system undergoes phase separation (PS); for very large negative values it collapses (CL)

the original parameters in S_0 in a straightforward way. Using the numerical solution of the flow equations, we find that $K_\sigma \rightarrow 0$, as can be expected for an ordering of the nature of a spin gap, leaving K_ρ the only parameter characterizing the QLRO in this phase.

In order to determine the QLRO in the system we will determine the scaling exponents of various order parameters. The order parameter with the largest positive scaling exponent shows the dominant order, whereas other orders with positive exponent are subdominant.

We will now apply this procedure to the different types of mixtures. For a FFM we find that the system always develops a gap, with the exception of the repulsive SU(2) symmetric regime (cf. [10]). To determine the QLRO we introduce the following operators [22,102]:

$$O_{\mathrm{SS}} = \sum_{\sigma,\sigma'} \tilde{\sigma} f_{R,\sigma} \delta_{\sigma,\sigma'} f_{L,3-\sigma'} ,$$

$$O^a_{TS} = \sum_{\sigma,\sigma'} \tilde{\sigma} f_{R,\sigma} \sigma^a_{\sigma,\sigma'} f_{L,3-\sigma'} ,$$

$$O_{\mathrm{CDW}} = \sum_{\sigma,\sigma'} f^\dagger_{R,\sigma} \delta_{\sigma,\sigma'} f_{L,\sigma'} , \text{ and}$$

$$O^a_{SDW} = \sum_{\sigma,\sigma'} \tilde{\sigma} f^\dagger_{R,\sigma} \sigma^a_{\sigma,\sigma'} f_{L,\sigma'} ,$$

with $\sigma, \sigma' = 1, 2$, $\tilde{\sigma} = 3 - 2\sigma$, and $a = x, y, z$. In the gapless SU(2) symmetric regime, both CDW and SDW show QLRO, with both scaling exponents of the form $\alpha_{\mathrm{SDW/CDW}} = 1 - K_\rho$ [102], which shows that these orders are algebraically degenerate. Within the gaped regime the scaling exponents of these operators are given by $\alpha_{SS,TS_z} = 2 - K_\rho^{-1}$ and $\alpha_{\mathrm{CDW,SDW}_z} = 2 - K_\rho$. As discussed in [22], the sign of g_{12} determines whether CDW or SDW_z, and SS or TS_z appears. In Fig. 4a, we show the phase diagram based on these results. In addition to these phases we indicate the appearance of the Wentzel–Bardeen instability, shown as phase separation for repulsive interaction and collapse for attractive interaction.

We will now use the dual mapping to obtain the phase diagram of a FFM with complementary filling from Fig. 4a. Under this mapping, the attractive and repulsive regimes are exchanged with the following replacements: $\mathrm{CDW} \rightarrow \mathrm{SDW}_z$, $\mathrm{SDW}_z \rightarrow \mathrm{CDW}$, $\mathrm{SS}, \mathrm{TS}_z \rightarrow \mathrm{SDW}$, and $\mathrm{SDW} \rightarrow \mathrm{SS}$. Note that the gapless regime is now on the attractive side, with degenerate CDW and SS pairing.

For BBMs we proceed in the same way as for FFMs. We introduce the following set of order parameters: $O_{\mathrm{CDW}} = b_1^\dagger b_1 + b_2^\dagger b_2$, $O_{\mathrm{SS}} = b_1 b_2$, $O_{\mathrm{SDW}_z} = b_1^\dagger b_1 - b_2^\dagger b_2$, $O_{\mathrm{SDW}_x} = b_1^\dagger b_2 + b_2^\dagger b_1$, $O_{\mathrm{SDW}_y} = -i(b_1^\dagger b_2 - b_2^\dagger b_1)$, and in addition the superfluid (SF) order parameters b_1 and b_2. In Fig. 4a we show the phase diagram of a mixture of a BBM of hardcore bosons, which is almost identical to the one of a FFM. The phase diagram of the mixture with complementary filling, as obtained from the dual mapping, is

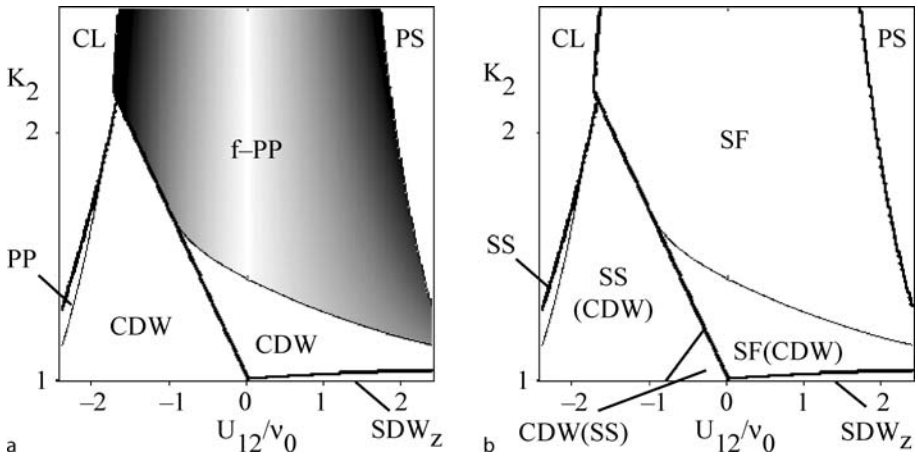

Ultracold Atomic Gases: Novel States of Matter, Figure 5

a Phase diagram of a BFM, b phase diagram of a BBM with the first species being in the hardcore limit, in terms of U_{12}, and the Luttinger parameter of the second species (K_2), at the fixed velocity ratio $|v_1 - v_2|/(v_1 + v_2) = 0.5$. For large repulsive interaction the system undergoes phase separation (PS), for large attractive interaction the system collapses (CL). In the regime below the *thick line* the system opens a gap, i. e. if species 2 is close to the hardcore limit. However, for larger values of K_2, the gapless phase is restored. Close to the transition, the properties of the fermions, respectively hardcore bosons, are still affected by the RG flow, leading to CDW order for the fermions and to supersolid behavior for the bosons

also of the same form as its fermionic equivalent, with the exception of the gapless regime, in which BBMs show supersolid behavior (coexistence of SF and CDW order), and with the replacement $TS_z \to SS$.

In Fig. 5b, we show the phase diagram of a mixture of hardcore bosons (species 1) and bosons in the intermediate to hardcore regime (species 2). If species 2 is sufficiently far away from the hardcore limit, the system remains gapless. However, in the vicinity of the transition the scaling exponents of the liquids are affected by the RG flow. As indicated, the effective scaling exponent of the hardcore bosons is renormalized to a value that is smaller than 1, and therefore we find both SF and CDW order, i. e. supersolid behavior. The phase diagram of the dual mixture is of the following form: the attractive and the repulsive regime are exchanged, and in the gaped phase we again have the mapping: $CDW \to SDW_z$, $SDW_z \to CDW$, $SS \to SDW$, and $SDW \to SS$. The gapless regime is unaffected.

For a BFM we find that the order parameters O_{CDW}, O_{SDW_z}, $O_{f-PP} = f_R f_L e^{-2i\lambda\Phi_b}$ [60,64], and b can develop QLRO in the gapless regime. In the gaped regime, the order parameters $O_{PP} \equiv f_R b f_L b$ and $O_{PP'} \equiv f_R b^\dagger f_L b^\dagger$, in addition to O_{CDW}, show QLRO. ($O_{PP/PP'}$ are special cases of the polaron pairing operators discussed in [60,64].) In Fig. 4b we show the phase diagram of a BFM with hardcore bosons, and in Fig. 5a, we vary the Luttinger parameter of the bosons. In both the gapless phase and the gaped phase, we find that CDW and f-PP or PP, respectively, are mutually exclusive and cover the entire phase diagram, cf. [60,64]. The dual mapping again maps attractive and repulsive regimes onto each other. Within the gaped phase we find the mapping $CDW \to SDW_z$, $SDW_z \to CDW$, and $PP \to PP'$, the gapless regime is unaffected.

Before we conclude, we discuss how these predictions could be measured experimentally. CDW order will create additional peaks in TOF images, corresponding to a wavevector $Q = 2k_f$. As demonstrated and pointed out in [3,18,29,61], the noise in TOF images allows to identify the different regimes of both gaped and gapless phases. As discussed in [60,64], a laser stirring experiment could determine the onset of CDW order for fermions, or the supersolid regime for bosons. RF spectroscopy [12] can be used to determine the presence and the size of an energy gap.

In conclusion, we have studied mixtures of ultra-cold atoms in 1D with commensurate filling. We used a Luttinger liquid description which enables us to study FFMs, BFMs, and BBMs in a single approach. We find that FFMs are generically gaped for both attractive and repulsive interactions, whereas for BFMs and BBMs the bosons need to be close to the hardcore limit. We find a rich structure of quasi-phases in the vicinity of these transitions, in particular a supersolid phase for BBMs, that occurs close to the hardcore limit. Experimental methods to detect the predictions were also discussed.

Phase-Locking Transition of Coupled Low-Dimensional Superfluids

Most phase transitions that have been realized in ultracold atom systems are generic first or second order transitions. However, the paradigm of phase transitions in two dimensions at finite temperature is of a more intricate type, a Kosterlitz–Thouless transition, which is characterized by a change of the functional form of the correlation function of the order parameter, from algebraic decay to exponential decay. In an intriguing new development in studying low-dimensional strongly correlated systems, such a Kosterlitz–Thouless (KT) transition [11] was indeed realized and observed [30]. In this experiment the interference amplitude between two independent two-dimensional (2D) Bose systems was studied as a function of temperature. This analysis revealed the jump in the superfluid stiffness (see also [80]) and the emergence of unpaired isolated vortices as they crossed the phase transition.

The other focus of this section, the physics of ramping across a phase transition, is also triggered by a recent experiment: Sadler et al. observed spontaneous generation of topological defects in the spinor condensate after a sudden quench (i. e. a rapid, non-adiabatic ramp) through a quantum phase transition [84]. A similar experiment in a double-layer system was reported in [85]. The topological defects are generated [45] at a density which is related to the rate at which the transition is crossed [108]. Later it was argued that the dependence of the number of such defects on the swipe rate across a quantum critical point can be used as a probe of the critical exponents characterizing the phase transition [81]. This Kibble–Zurek (KZ) mechanism was originally considered as an early universe scenario creating cosmic strings, which would serve as an ingredient for the formation of galaxies[6]. Cold atom systems appear to be a very suitable laboratory for performing such "cosmological experiments", since these systems are highly tunable and well isolated from the environment. So far the experiments and the theoretical proposals addressed the KZ scenario across a quantum phase transition. The main reason is that it is generally hard to cool such systems sufficiently fast to observe non-equilibrium effects. In this work we provide an example of a particular system where this difficulty can be easily overcome by quenching the transition temperature T_c instead of T. Thus the relevant ratio T/T_c can be tuned with an arbitrary rate and the KZ mechanism can be observed. Specifically, we examine a system of two superfluids (SF): As we show below, by turning on tunneling between the two systems the transition temperature increases rapidly, and the system attempts to create long-range order (LRO). However, in this process, defects in the SF phase are created, which develop into long-lived vortex-anti-vortex pairs or in finite system unbalanced population between vortices and anti-vortices. We note that because the systems are isolated and there is no external heat bath, the temperature itself also changes due to the quench. However, the long-wavelength fluctuations relevant for the KT transition are only a small subset of all degrees of freedom, majority of which are only weakly affected by small inter-layer tunneling. So we believe that the change of the T_c is the main effect of the quench.

In this section we consider two SFs coupled via tunneling and/or interactions. In the experiments the hopping or tunneling rate between two systems can be tuned to a high precision [30,31,77,87]. Interactions between the atoms in different systems can either be realized in ensembles of polar molecules or by using mixtures of two hyperfine states, where the tunneling rate is controlled by an infrared light source [41], which induces spin-flipping between the hyperfine states. In this case the atoms in different states naturally interact with each other since they are not physically separated in space. The main results of our analysis are the phase diagrams of coupled SFs in Figs. 6 and 7, the behavior of T_c and the energy gap shown in Fig. 8, as well as the

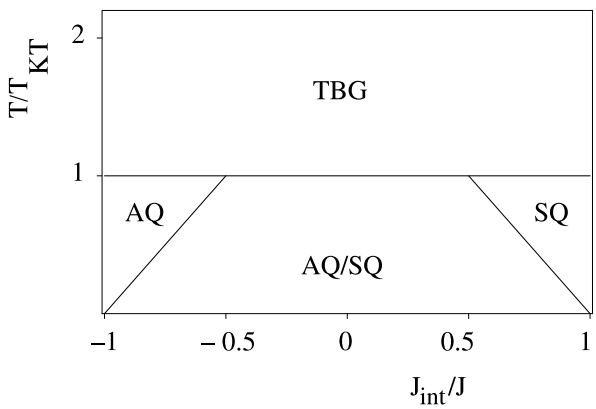

Ultracold Atomic Gases: Novel States of Matter, Figure 6
Phase diagrams of two 2D SFs, coupled through a term of the form S_{12}, Eq. (22), in terms of J_{int}/J and T/T_{KT}. For low temperatures we find antisymmetric quasi-order (AQ) and/or symmetric quasi-order (SQ), which either simultaneously undergo a KT transition due to single vortices (AQ/SQ to thermal Bose gas (TBG) phase), or individually due to correlated vortex pairs: symmetric (anti-symmetric) vortex pairs drive the AQ/SQ to AQ (SQ) transition

[6] Since then, it has been established that cosmic strings can only contribute a small fraction of the initial density perturbations. We thank T. Kibble for this comment.

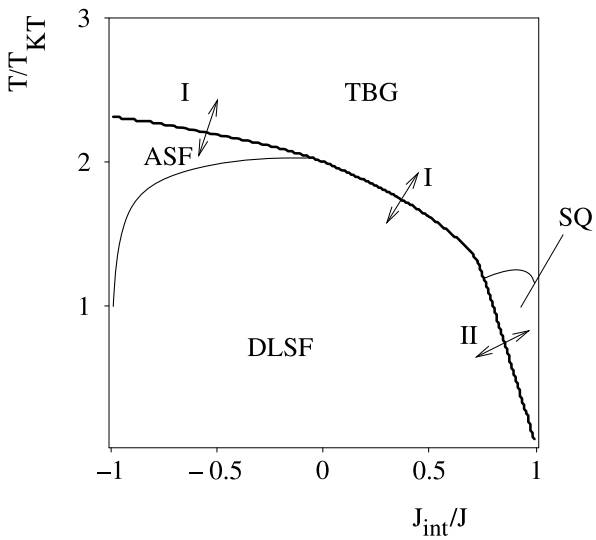

Ultracold Atomic Gases: Novel States of Matter, Figure 7
Phase diagram, temperature (in units of T_{KT}) versus interaction (in units of J). We assume $J_\perp/J \sim 10^{-3}$ and $A_1/J \sim 10^{-3}$. DLSF: double layer superfluid; TBG: thermal Bose gas; ASF: anti-symmetric superfluid; SQ: symmetric quasi-order. The order of the transition lines are either first (I), second order (II), or KT (*thin lines*)

proposal of realizing the KZ mechanism by switching on the tunneling between two SFs.

2D Superfluids

In this section we consider two 2D SFs, each characterized by a KT temperature T_{KT}. We write the bosonic operators $b_{1/2}$ in the two layers in a phase-density representation [11,24], $b_{1/2} \sim \sqrt{\rho_{1/2}}\exp(i\phi_{1/2})$, where $\rho_{1/2}$ are the density operators of the two systems, and $\phi_{1/2}$ the phases. The low-momentum fluctuations of the phase fields are described by Gaussian contributions to the Hamiltonian $\mathcal{H}_0$. Because of the formal analogy between the quantum 1D and thermal 2D systems [22] we adopt the quantum terminology throughout the paper and refer to the ratio of the Hamiltonian and the temperature as the action. Then

$$S_0 \equiv \frac{\mathcal{H}_0}{T} = \frac{J}{2T}\int \mathrm{d}^2 r\left[(\nabla\phi_1)^2 + (\nabla\phi_2)^2\right] . \qquad (18)$$

The energy scale J here is related to T_{KT} by $J = 2T_{KT}/\pi$. Besides these long-wavelength fluctuations, the system also contains additional degrees of freedom, vortex-anti-vortex pairs [11]. The corresponding term in the action is expressed through the dual fields $\theta_{1,2}$ [24]:

$$S_1 = \frac{2A_1}{T}\int \frac{\mathrm{d}^2 r}{(2\pi\alpha)^2}\left[\cos(2\theta_1) + \cos(2\theta_2)\right] , \qquad (19)$$

where α is a short-distance cut-off of the size of the vortex core, and A_1 is proportional to the single-vortex fugacity: $A_1 \sim J\exp(-J/T)$, where we assume both SFs to have the same effective parameters J and A_1. Operators of the type $\exp(2i\theta)$ create kinks in the field ϕ: $\exp(-2i\theta(x))\phi(x')\exp(2i\theta(x)) \sim \phi(x') + 2\pi\Theta(x - x')$, $\Theta(x)$ being the step function, which corresponds to the effect of vortices in the original 2D problem ([22], p 92).

In addition, the two systems are coupled by a hopping term $\sim t_\perp b_1^\dagger b_2 + \text{h.c.}$, which results in the following con-

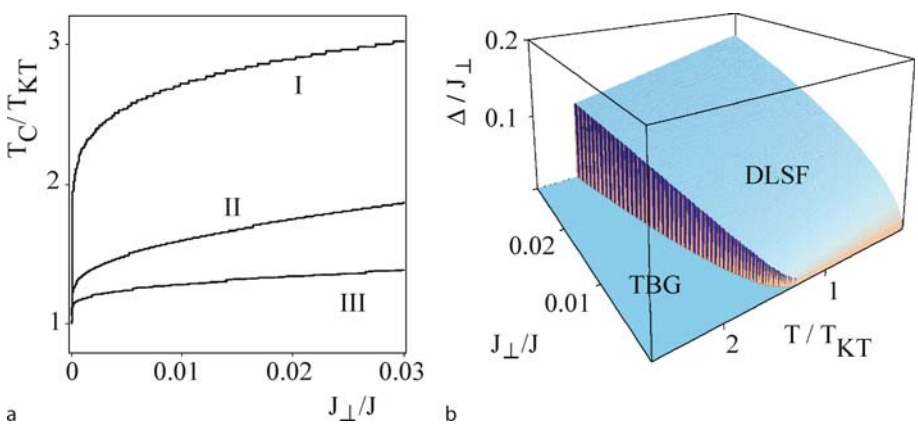

Ultracold Atomic Gases: Novel States of Matter, Figure 8
a Critical temperature T_c of the DLSF-TBG transition (in units of T_{KT}) for different values of A_1/J: 10^{-3}, 0.1, 0.4 (I–III), and for $J_{int} = 0$. b Energy gap in the anti-symmetric sector (in units of $J_\perp$) as a function of $J_\perp/J$ and temperature (in units of T_{KT}). We have set $A_1/J = 0.1$ and $J_{int} = 0$

tribution to the action:

$$S_\perp = \frac{2J_\perp}{T}\int \frac{\mathrm{d}^2 r}{(2\pi\alpha)^2}\cos(\phi_1-\phi_2)\,, \tag{20}$$

where the bare value of $J_\perp$ corresponds approximately to $t_\perp\rho_0$. In principle, the hopping term is modified by the vortex contributions, however, these corrections are always irrelevant under renormalization group (RG).

For most of the discussion in this paper we use the symmetric and anti-symmetric combinations of $\phi_{1/2}$ and $\theta_{1/2}$:

$$\phi_{\mathrm{s/a}} = (\phi_1 \pm \phi_2)/\sqrt{2}\,, \quad \theta_{\mathrm{s/a}} = (\theta_1 \pm \theta_2)/\sqrt{2}\,. \tag{21}$$

Written in these fields, the term S_0 in Eq. (18) is again a sum of Gaussian models, now in the fields ϕ_{s} and ϕ_{a}, with the same energy scale J. However, we will consider a broader class of actions, in which the energy scales of the symmetric and anti-symmetric sector differ. We include the following term in the action:

$$S_{12} = \frac{J_{\mathrm{int}}}{T}\int \mathrm{d}^2 r \nabla\phi_1\nabla\phi_2\,. \tag{22}$$

With this, the quadratic part of the action is given by:

$$S_0 + S_{12} = \frac{J_{\mathrm{s}}}{2T}\int \mathrm{d}^2 r(\nabla\phi_{\mathrm{s}})^2 + \frac{J_{\mathrm{a}}}{2T}\int \mathrm{d}^2 r(\nabla\phi_{\mathrm{a}})^2\,, \tag{23}$$

where J_{s} and J_{a} are given by $J_{\mathrm{s/a}} = J \pm J_{\mathrm{int}}$.

We now motivate the existence of such a term S_{12} in ultra-cold atom systems, by considering two BECs coupled by a short-range density–density interaction. Starting from a Hamiltonian of the form $H = \sum_k[\epsilon_{\mathbf{k}} b^\dagger_{\mathbf{k}} b_{\mathbf{k}} + (g/2V)\rho^\dagger_{\mathbf{k}}\rho_{\mathbf{k}}]$, where $b_{\mathbf{k}}$ is the boson operator, $\epsilon_{\mathbf{k}}$ the free dispersion $\epsilon_{\mathbf{k}} = \mathbf{k}^2/2m$, g is the interaction strength of the contact interaction, V the volume, and $\rho_{\mathbf{k}}$ is the density operator of momentum $\mathbf{k}$, given by $\rho_{\mathbf{k}} = \sum_{\mathbf{p}} b^\dagger_{\mathbf{p}} b_{\mathbf{p}+\mathbf{k}}$, we assume that the zero momentum mode is macroscopically occupied, and formally replace the operator b_0 by a number, $b_0 \to \sqrt{N_0}$, where N_0 is the number of condensed atoms which is comparable to the total atom number N, i. e. $N_0 \sim N$. Next we keep all terms that are quadratic in $b_{\mathbf{k}}$ (with $\mathbf{k} \neq 0$), and perform a Bogoliubov transformation, given by: $b_{\mathbf{k}} = u_{\mathbf{k}}\beta_{\mathbf{k}} + v_{\mathbf{k}}\beta^\dagger_{-\mathbf{k}}$, to diagonalize the Hamiltonian. The eigenmodes $\beta_{\mathbf{k}}$ have a dispersion relation $\omega_{\mathbf{k}} = \sqrt{\epsilon_{\mathbf{k}}(\epsilon_{\mathbf{k}} + 2gn)}$, with n being the density N/V. The low-$\mathbf{k}$ limit is given by $\omega^2_{\mathbf{k}} \sim v^2|\mathbf{k}|^2$, with $v = \sqrt{gn/m}$, which corresponds to the contribution in Eq. (18) of the action. Next, we consider the sum of two copies of the previous Hamiltonian with boson operators $b_{1/2}$. In addition we consider an interaction $H_{12} = g_{12}/V\sum_{\mathbf{k}}\rho^\dagger_{1,\mathbf{k}}\rho_{2,\mathbf{k}}$, where the density operators $\rho_{1/2,\mathbf{k}}$ are given by $\rho_{1/2,\mathbf{k}} = \sum_{\mathbf{p}} b^\dagger_{1/2,\mathbf{p}} b_{1/2,\mathbf{p}+\mathbf{k}}$. Following the same procedure as before, we find two eigenmode branches, corresponding to in-phase and out-of-phase superpositions of the modes of each condensate, with the dispersions $\omega^2_{\mathrm{s/a},\mathbf{k}} \sim v^2_{\mathrm{s/a}}|\mathbf{k}|^2$, with the velocities $v_{\mathrm{s/a}} = \sqrt{(g \pm g_{12})n/m}$. Therefore, for this example, the energy scale J_{int} is related to $g_{12}n/m$, which would be of similar order as J for a system interacting via contact interaction, for small temperatures. This discussion only applies to the weakly interacting limit of a true condensate. However, it demonstrates that a density–density contact interaction term can lead to a substantial energy splitting of the in-phase and out-of phase modes.

Finally, in addition to single vortices in each SF, we have to consider the possibility of correlated vortex pairs, i. e. one vortex in each layer at the same location of either the same or of opposite vorticity. We will refer to these vortex configurations as *symmetric* or *anti-symmetric vortex pairs*, respectively. These excitations appear as the following terms in the action:

$$S_{\mathrm{s,a}} = \frac{2A_{\mathrm{s,a}}}{T}\int \frac{\mathrm{d}^2 r}{(2\pi\alpha)^2}\cos(2\sqrt{2}\,\theta_{\mathrm{s,a}})\,. \tag{24}$$

These correlated vortex terms, which describe new degrees of freedom, can be the most relevant non-linear terms in the action, which derives from the possibility that the vortices in different layers interact with each other, through the terms (20) and (22). The effect of these terms is the following: At low temperatures the energy between two single vortices of opposite vorticity due to tunneling grows as the square of the distance D between them, i. e. as $J_\perp(D/\alpha)^2$. As a result, the tunneling term attempts to confine vortices of opposite vorticity, leading to phase-locking between the layers, which we describe further later on. The interaction S_{12} changes the energy of correlated vortex pairs as follows: The energy of a single vortex is given by $2\pi J \log L/\alpha$, where L is the system size, whereas a symmetric/anti-symmetric vortex pair has an energy of $4\pi(J \pm J_{\mathrm{int}})\log L/\alpha$. Therefore, symmetric vortex pairs are the lowest energy vortex excitations for $J_{\mathrm{int}} < -J/2$, whereas for $J_{\mathrm{int}} > J/2$ anti-symmetric vortex pairs are the lowest energy excitations. As we will see below, in these regimes correlated vortex pairs drive transitions to phases, in which one sector is (quasi-)SF whereas the other is disordered. We will also see that these terms are generated under the RG flow, even if not present at the onset.

We note that a similar system has been studied in [8]. Here, we consider a larger class of systems by including the interaction term (22), which in turn requires us to include

the correlated vortex excitations (24). These terms give rise to additional phases as we will see in the following.

Next we analyze our system within the RG approach. This RG flow is perturbative in the vortex fugacities A_1, A_s, and A_a, and the tunneling energy $J_\perp$, and therefore applies to the weak-coupling limit (in particular $J_\perp \to +0$). At second order the flow equations are given by [6]:

$$\frac{\mathrm{d}J_\perp}{\mathrm{d}l} = \left(2 - \frac{T}{2\pi J_a}\right) J_\perp \,, \tag{25}$$

$$\frac{\mathrm{d}A_s}{\mathrm{d}l} = \left(2 - 2\pi\frac{J_s}{T}\right) A_s + \alpha_3 \frac{A_1^2(J_a - J_s)}{2T^2} \,, \tag{26}$$

$$\frac{\mathrm{d}A_a}{\mathrm{d}l} = \left(2 - 2\pi\frac{J_a}{T}\right) A_a + \alpha_3 \frac{A_1^2(J_s - J_a)}{2T^2} \,, \tag{27}$$

$$\frac{\mathrm{d}A_1}{\mathrm{d}l} = \left(2 - \frac{\pi(J_s + J_a)}{2T} + \alpha_3 \frac{A_s J_s + A_a J_a}{T^2}\right) A_1 \,, \tag{28}$$

$$\frac{\mathrm{d}J_a}{\mathrm{d}l} = \alpha_2 \left(\frac{J_\perp^2}{4\pi^4 J_a} - 4\frac{A_a^2}{T^4} J_a^3 - \frac{A_1^2}{2T^4}(J_s + J_a) J_a^2\right) \,, \tag{29}$$

$$\frac{\mathrm{d}J_s}{\mathrm{d}l} = -\alpha_2 \left(2\frac{A_s^2}{T^4} J_s^2 + \frac{A_1^2}{4T^4}(J_s + J_a) J_s\right) 2J_s \,. \tag{30}$$

The coefficients $\alpha_{2/3}$ are non-universal parameters that appear in the RG procedure [51], and which do not affect the results qualitatively. For consistency, we have to expand the right-hand site of the above equations up to second order, around the resulting Gaussian fixed point: $J_{s/a} = J \pm J_{\mathrm{int}} + j_{s/a}$. We emphasize again that J_{int} near the fixed point can be generated by RG and be nonzero even if it is not present at the onset.

Before we consider the full RG flow, we consider the simpler case of no tunneling, i. e. we solve the RG equations while setting $J_\perp = 0$. In Fig. 6 we show the phase diagram of two 2D SFs coupled by S_{12}, Eq. (22). Such a system would be realized by a 2D mixture of bosonic atoms in two different hyperfine states, interacting via some short-range potential. The order parameters we consider are $O_s(x) = b_1(x)b_2(x)$ and $O_a(x) = b_1^\dagger(x)b_2(x)$. To obtain the phase diagram we consider the correlation functions of each of these order parameters, which can either scale algebraically or exponentially. In Fig. 6 we refer to algebraic scaling of $O_s(x)$ as symmetric quasi-order (SQ), and of $O_a(x)$ as anti-symmetric quasi-order (AQ). In each of the sectors a KT transition marks the transition from the algebraic to the exponential regime, which occur either simultaneously and are driven by single-vortex excitations, or at different temperatures and are driven by correlated vortex pairs. As a result we find four regimes: At temperatures above T_{KT}, both sectors are disordered, giving rise to a thermal Bose gas (TBG) phase. For temperatures below T_{KT}, and for a wide range of J_{int}, we find that both sectors are quasi SF (AQ/SQ), which is the only phase in which the correlation function of the single boson operators show algebraic scaling. We also find regimes in which only one sector shows algebraic scaling, whereas the other is disordered (AQ and SQ). From the perspective of vortices, the TBG phase is a gas of free single vortices in each layer, whereas the AQ (SQ) phase is a gas of symmetric (anti-symmetric) vortex pairs.

We now consider the full RG system, including $J_\perp$. We numerically integrate the RG equations, and find the phase diagram shown in Fig. 7 in terms of the temperature T and the interaction J_{int}. We again find four different phases that are different combinations of LRO, QLRO, and disorder in the symmetric and anti-symmetric sector. At high temperatures we find that both sectors are disordered in a TBG phase, as before. For lower temperatures, and for a wide range of J_{int}, the system is in a double-layer SF phase (DLSF): The symmetric sector shows algebraic scaling, whereas the exponent of the anti-symmetric sector is renormalized to zero, i. e. we find two SFs that are phase-locked due to $J_\perp$. Note that the transition temperature T_c between DLSF and TBG has been noticeably increased relative to the decoupled value T_{KT}, as we will discuss further later on. We also find two additional phases, which are partially (quasi-)SF and partially disordered. One of them is the SQ phase, as before, whereas the other one (ASF), now shows true LRO in the anti-symmetric sector due to $J_\perp$, whereas the symmetric sector remains disordered. We note that the generic double-layer action that we discuss in this paper does not show a sliding phase [71], for any non-zero $J_\perp$. Either S_1 or S_a, which is generated by RG, drives the anti-symmetric sector to a disordered state, or $S_\perp$ creates true LRO in the field ϕ_a.

We also use the RG flow to find the order of the phase transitions in the weak-coupling limit that the anti-symmetric sector undergoes, by determining the energy gap using a 'poor-man's scaling' argument: when the coupling amplitude $J_\perp(l^*)$ is of order unity the corresponding gap is given by the expression $\Delta \sim J_\perp \exp(-l^*)$. From the behavior of Δ at the phase transition we can read off whether it is of first or second order, as indicated in Fig. 7.

Given the nature of an effective theory, only approximate statements can be made about how the different regimes of the phase diagram relate to the microscopic interactions. To create the ASF or AQ phase an attraction between the two atom species is needed that is of order J, whereas to create the SQ phase, a repulsion of that order would be needed. To detect the different phases, one could use the interference method used in [30] to distinguish the phase-locked phases (DLSF and ASF), which would show a well-defined interference pattern, from the uncorrelated

phases. Another approach would be time-of-flight images: The DLSF phase would display a quasi-condensate signature, whereas the other phases would appear disordered. However, at the transition from ASF or SQ to TBG, the width of the distribution would abruptly increase.

Kibble–Zurek Mechanism

In this section we discuss how the phase-locking transition found in the previous section could be used to realize the KZ mechanism. The defining property of this mechanism is the generation of topological defects by ramping across a phase transition, coming from the disordered phase. The disordered phase that we propose to use is the TBG phase of the *decoupled* 2D systems, that is, we consider the experimental setup reported in ref. [30] for a temperature T above the KT temperature T_{KT}. The ordered phase we consider is the DLSF phase, i. e. the phase-locked phase of two *coupled* SFs. The ramping is achieved by turning on the tunneling between the two layers, which can be done by lowering the potential barrier between them. For this procedure the critical temperature T_{c} of the DLSF-TBG transition needs to be above the KT temperature of the uncoupled systems. We now show that the RG flow indeed predicts such a scenario. In the experiments in [30], the atoms in different layers do not interact with each other. Therefore, it can be expected that J_{int} is small, of order $J_{\perp}$, which motivates us to discuss the case $J_{\mathrm{int}} = 0$ here. We note however, that the desired scenario of an increased critical temperature, is found for a wide range of J_{int}, as can be seen in Fig. 7. In Fig. 8a we show how the critical temperature of the DLSF-TBG transition behaves, predicted by the RG flow, for different values of A_1. The critical temperature shows a sizable increase, due to the phase-locking transition. Due to the perturbative nature of the RG scheme, the RG flow underestimates the effects of the term S_1, and predicts a finite jump of the critical temperature when $J_{\perp}$ is turned on. However, to lock the SFs together in the regime slightly above T_{KT}, $J_{\perp}$ needs to be at least of the order of the vortex core energy, giving rise to a finite slope of T_{c} instead of a jump. The energy gap of this transition is shown in Fig. 8 from which we can see that the transition is of first order, in contrast to the second order transition described in [45,108], which is advantageous because the onset of order is instantaneous rather than continuous. We note that the phase diagram was obtained using the assumption that the bare parameters of the model, in particular J, do not depend on temperature. This is true only if temperature is close to T_{KT}. Here we find that the ratio $T_{\mathrm{c}}/T_{\mathrm{KT}}$ can be relatively large. In fact $T_{\mathrm{c}}/T_{\mathrm{KT}}$ will be always smaller than that shown in Fig 8a, however, qualitatively the behavior of $T_{\mathrm{c}}/T_{\mathrm{KT}}$ as a function of $J_{\perp}$ should remain intact. We point out that our results can be generalized to a system of $N > 2$ coupled SFs. One finds that the SFs still show a strong tendency to phase-lock together. As a result the critical temperature should approximately satisfy the equality $\pi J(T_{\mathrm{c}})N = 2T_{\mathrm{c}}$. Thus as N increases T_{c} approaches the mean-field critical temperature at which the stiffness J vanishes and we recover the usual 3D result.

In finite size systems there is another constraint on the minimum value of $J_{\perp}$: We consider the free energy of a single vortex in the anti-symmetric field: $\phi_{\mathrm{a}} \sim \arctan(x/y)$. For the decoupled system we get for the free energy [51]: $F \sim 2(\pi J - 2T)\log L/\alpha$, where L is the system size. The coupling term gives a free energy contribution $F_{\perp} \sim J_{\perp}(L/\alpha)^2$. In the thermodynamic limit, $L \to \infty$, this term diverges faster than the others, which is consistent with our finding of LRO in the antisymmetric sector. For a finite system, comparing these terms gives the estimate $J_{\perp} \sim J\log(L/\alpha)/(L/\alpha)^2$, that is required for this order to develop. With a system size $L/\alpha \sim 10^2$, that would require $J_{\perp} \sim 10^{-3}J$, which, for the setup in [30], would be around $10^2 s^{-1}$.

As an estimate of the number of domains that would be created, we follow the argument in [45]: The coherence scale of the DLSF phase is given by $(J/\Delta)^{1/2}\alpha$, which is the scale of a Klein–Gordon model with a kinetic energy scale J and a 'mass-term' with a prefactor Δ/α^2. The domain size is then given by $(J/\Delta)\alpha^2$, and the number of domains by $\sim (\Delta/J)L^2/\alpha^2$. As we show in Fig. 8b for $J_{\perp}/J \approx 10^{-2}$, we find $\Delta/J_{\perp} \sim 10^{-1}$, and therefore $J/\Delta \sim 10^3$. With $L/\alpha \sim 10^2$, we would get $N_{\mathrm{dom}} \sim 10^1 - 10^2$, which would generate a similar number of vortices. We estimate the vortex-antivortex imbalance by considering the number of domains around the periphery of the system, which scales as L/ξ. If we imagine that the phase behaves like a random walk, the total phase mismatch, corresponding to the vortex-antivortex imbalance, will scale as $\sqrt{L/\xi} \sim N_{\mathrm{dom}}^{1/4}$, which, for $L/\alpha \sim 10^2$, is of the order 10^0–10^1.

In summary, we propose the following procedure: i) Prepare two uncoupled SFs at a temperature T slightly above T_{KT}. ii) Switch on the tunneling between the two layers, which creates a DLSF phase with a critical temperature T_{c} higher than T. As a result, one should find a number of long-lived vortex-antivortex pairs in the anti-symmetric phase field ϕ_{a}, which would be visible in an interference measurement, at a temperature where there would be none in thermal equilibrium.

In conclusion of the section, we studied the phase-locking transition of 2D superfluids, within an renormalization group approach. We find that this transition is accompanied by an increase of the transition temperature.

We suggest that this effect can be used to probe the Kibble–Zurek mechanism in cold atom systems by rapidly changing the ratio T/T_c. When we include interactions between the layers we find additional phases, in which either the symmetric or the anti-symmetric sector is disordered, and the other sector stays superfluid or quasi-superfluid.

Bose–Fermi Mixtures in Two-Dimensional Optical Lattices

In the spirit of engineering many-body systems that are relevant in other fields, we now turn to atomic mixtures that resemble qualitatively, i. e. in terms of degrees of freedom of the system, electron–phonon systems. In two dimensions, these systems are actively studied and prove to be of considerable complexity. In order to study their atomic counterparts, Bose–Fermi mixtures in optical lattices, we use the powerful method of functional renormalization group equations, with which we can determine their phase diagrams in the weak-coupling limit in a systematic fashion. We find a rich competition of phases for both the square lattice and triangular lattice geometry that we consider.

In this section we consider mixtures of one bosonic type of atom and either two fermionic types that are SU(2) symmetric or spinless fermions. The Hamiltonian for a mixture on a square lattice is given by:

$$\begin{aligned} H = &-t_\mathrm{f} \sum_{\langle ij\rangle,s} f_{i,s}^\dagger f_{j,s} - t_\mathrm{b} \sum_{\langle ij\rangle} b_i^\dagger b_j \\ &- \sum_i (\mu_\mathrm{f} n_{\mathrm{f},i} + \mu_\mathrm{b} n_{\mathrm{b},i}) \\ &+ \sum_i \left[U_\mathrm{ff} n_{\mathrm{f},i,\uparrow} n_{\mathrm{f},i,\downarrow} + \frac{U_\mathrm{bb}}{2} n_{\mathrm{b},i} n_{\mathrm{b},i} + U_\mathrm{bf} n_{\mathrm{b},i} n_{\mathrm{f},i} \right], \end{aligned} \tag{31}$$

where $f_{i,s}^\dagger$ ($f_{i,s}$) creates (annihilates) a fermion at site i with pseudo-spin s ($s = \uparrow, \downarrow$), $b_i^\dagger$ (b_i) creates (annihilates) a boson at site i, $n_{\mathrm{f},i} = \sum_s f_{i,s}^\dagger f_{i,s}$ ($n_{\mathrm{b},i} = b_i^\dagger b_i$) is the fermion (boson) number operator, t_f and t_b are the fermionic and bosonic tunneling energies between neighboring sites, μ_f (μ_b) is the chemical potential for fermions (bosons), U_bb is the repulsion energy between bosons on the same site, U_ff is the repulsion energy between the two species of fermions, and U_bf is the repulsion energy between bosons and fermions. The two fermion species have been treated as a pseudo-spin-1/2 index ($\uparrow$ and $\downarrow$). The case of spinless fermions can be immediately obtained from (31) by ignoring one of the spin states. In momentum space, the Hamiltonian (31) is written as:

$$\begin{aligned} H = \sum_\mathbf{k} \Bigg\{ &(\epsilon_{\mathrm{f},\mathbf{k}} - \mu_\mathrm{f}) \sum_s f_{\mathbf{k},s}^\dagger f_{\mathbf{k},s} + (\epsilon_{\mathrm{b},\mathbf{k}} - \mu_\mathrm{b}) b_\mathbf{k}^\dagger b_\mathbf{k} \\ &+ \frac{U_\mathrm{ff}}{V} \rho_{\mathrm{f},\mathbf{k},\uparrow} \rho_{\mathrm{f},-\mathbf{k},\downarrow} + \frac{U_\mathrm{bb}}{2V} \rho_{\mathrm{b},\mathbf{k}} \rho_{\mathrm{b},-\mathbf{k}} + \frac{U_\mathrm{bf}}{V} \rho_{\mathrm{b},\mathbf{k}} \rho_{\mathrm{f},-\mathbf{k}} \Bigg\}, \end{aligned} \tag{32}$$

where $\rho_{\mathrm{f},\mathbf{k}} = \sum_{\mathbf{q},s} f_{\mathbf{k}+\mathbf{q},s}^\dagger f_{\mathbf{k},s}$ ($\rho_{\mathrm{b},\mathbf{k}} = \sum_\mathbf{q} b_{\mathbf{k}+\mathbf{q}}^\dagger b_\mathbf{k}$) is the fermion (boson) density operator, $\epsilon_{\mathrm{b/f},\mathbf{k}} = -2t_{\mathrm{b/f}}(\cos k_x + \cos k_y)$, is the bosonic/fermionic dispersion relation.

We consider the limit of weakly interacting bosons that form a BEC [62,104], where we assume that the zero momentum bosonic mode is macroscopically occupied, and the corresponding operator b_0 can be formally replaced by a real number $b_0 \to \sqrt{N_0}$, where N_0 is the number of condensed atoms. After this replacement we keep all terms that are quadratic in $b_\mathbf{k}$ (with $\mathbf{k} \neq 0$), and perform a Bogoliubov transformation, given by: $b_\mathbf{k} = u_\mathbf{k} \beta_\mathbf{k} + v_\mathbf{k} \beta_{-\mathbf{k}}^\dagger$, to diagonalize the bosonic Hamiltonian. The resulting eigenmodes $\beta_\mathbf{k}$ have a dispersion relation given by $\omega_\mathbf{k} = \sqrt{\epsilon_{\mathrm{b},\mathbf{k}}(\epsilon_{\mathrm{b},\mathbf{k}} + 2U_\mathrm{bb} n_\mathrm{b})}$, with the low-$\mathbf{k}$ limit $\omega_\mathbf{k} \sim v_\mathrm{b}|\mathbf{k}|$, with $v_\mathrm{b} = \sqrt{2t_\mathrm{b} U_\mathrm{bb} n_\mathrm{b}}$. The parameters $u_\mathbf{k}$ and $v_\mathbf{k}$ are given by: $u_\mathbf{k}^2 = (\omega_\mathbf{k} + \epsilon_{\mathrm{b},\mathbf{k}} + U_\mathrm{bb} n_\mathrm{b})/(2\omega_\mathbf{k})$ and $v_\mathbf{k}^2 = (-\omega_\mathbf{k} + \epsilon_{\mathrm{b},\mathbf{k}} + U_\mathrm{bb} n_\mathrm{b})/(2\omega_\mathbf{k})$.

The density fluctuations of the bosons are approximated by: $\rho_{\mathrm{b},\mathbf{k}} \approx \sqrt{N_0}(u_\mathbf{k} + v_\mathbf{k})(\beta_\mathbf{k} + \beta_{-\mathbf{k}}^\dagger)$, with $\mathbf{k} \neq 0$. The interaction between bosons and fermions is then given by $U_\mathrm{bf}\sqrt{N_0}/V \sum_\mathbf{k} (u_\mathbf{k} + v_\mathbf{k})(\beta_\mathbf{k} + \beta_{-\mathbf{k}}^\dagger)\rho_{\mathrm{f},-\mathbf{k}}$. As a next step we integrate out the bosonic modes and use an instantaneous approximation, leading to the following effective Hamiltonian:

$$\begin{aligned} H_\mathrm{eff.} = \sum_\mathbf{k} \Bigg\{ &(\epsilon_\mathbf{k} - \mu_\mathrm{f}) \sum_s f_{\mathbf{k},s}^\dagger f_{\mathbf{k},s} + \frac{U_\mathrm{ff}}{V} \rho_{\mathrm{f},\mathbf{k},\uparrow} \rho_{\mathrm{f},-\mathbf{k},\downarrow} \\ &+ \frac{1}{2V} V_{\mathrm{ind.},\mathbf{k}} \rho_{\mathrm{f},\mathbf{k}} \rho_{\mathrm{f},-\mathbf{k}} \Bigg\}, \end{aligned} \tag{33}$$

where the induced potential $V_{\mathrm{ind.},\mathbf{k}}$ is given by:

$$V_{\mathrm{ind.},\mathbf{k}} = -\tilde{V}/(1 + \xi^2(4 - 2\cos k_x - 2\cos k_y)), \tag{34}$$

with $\tilde{V}$ given by $\tilde{V} = U_\mathrm{bf}^2/U_\mathrm{bb}$, and ξ is the healing length of the BEC and is given by $\xi = \sqrt{t_\mathrm{b}/2n_\mathrm{b}U_\mathrm{bb}}$. This approach is only valid when $v_\mathrm{b} \gg v_\mathrm{f}$, so that the fermion–fermion interaction mediated by the bosons can be considered as instantaneous. Away from this limit, retardation effects are present. In this case, one has to consider the frequency dependence of the interaction explicitly [50,96,97]. The full effective interaction, including re-

tardation, is given by:

$$V_{\text{ind.}}(\omega, \mathbf{k}) = -\left[\frac{\tilde{V}}{1+\xi^2(4-2\cos k_x - 2\cos k_y)}\right]\frac{\omega_{\mathbf{k}}^2}{\omega^2+\omega_{\mathbf{k}}^2}\,, \quad (35)$$

and the static limit (34) is recovered when $\omega_{\mathbf{k}} \gg \omega$. Equation (33) describes the scattering of two fermions from momenta $\mathbf{k}_1$ and $\mathbf{k}_2$, that are scattered into momenta $\mathbf{k}_3$ and $\mathbf{k}_4$. Momentum conservation at the interaction vertex requires that $\mathbf{k}_4 = \mathbf{k}_1 + \mathbf{k}_2 - \mathbf{k}_3$, and hence the interaction vertex, $U(\mathbf{k}_1, \mathbf{k}_2, \mathbf{k}_3)$, depends on three momenta. Its bare value from (33) can be written as:

$$U(\mathbf{k}_1, \mathbf{k}_2, \mathbf{k}_3) = U_{\text{ff}} + V_{\text{ind.},\mathbf{k}_1-\mathbf{k}_3}\,. \quad (36)$$

For the case with retardation, there is dependence on both the momenta and frequencies of the electrons so we have $U(k_1, k_2, k_3)$, with $k_4 = k_1 + k_2 - k_3$, where $k_i = (\omega, \mathbf{k})$.

Starting from non-interacting fermions, we ask the general question of what new many-body phases can emerge when the system is subjected to a given interaction $U(\mathbf{k}_1, \mathbf{k}_2, \mathbf{k}_3)$. Our approach to address this question is the renormalization-group method, described in the next section.

Renormalization-Group Method

Starting with a microscopic model of interacting electrons on a lattice, the renormalization-group (RG) method provides the effective model at a given temperature or energy scale [89]. The RG is implemented by systematically tracing out high energy degrees of freedom in a region between Λ and $\Lambda + \mathrm{d}\Lambda$, where Λ is the energy cut-off of the problem. In this process, the vertex U is renormalized. At the initial value of the cut-off $\Lambda = \Lambda_0$, the value of U is given by its bare value. For the BFM system we describe here, it is given by (36). At one loop, the RG flow is obtained from a series of coupled integral-differential equations [106] for all the different interaction vertices $U(\mathbf{k}_1, \mathbf{k}_2, \mathbf{k}_3)$. The RG equations read:

$$\begin{aligned}\partial_\ell U_\ell(\mathbf{k_1}, \mathbf{k_2}, \mathbf{k_3}) = &-\int_{p,\omega} \partial_\ell[G_{p\ell}G_{k\ell}]U_\ell(\mathbf{k_1}, \mathbf{k_2}, \mathbf{k})U_\ell(\mathbf{p}, \mathbf{k}, \mathbf{k_3})\\ &-\int_{p,\omega} \partial_\ell[G_{p\ell}G_{q_1\ell}]U_\ell(\mathbf{p}, \mathbf{k_2}, \mathbf{q_1})U_\ell(\mathbf{k_1}, \mathbf{q_1}, \mathbf{k_3})\\ &-\int_{p,\omega} \partial_\ell[G_{p\ell}G_{q_2\ell}]\Big\{-2U_\ell(\mathbf{k_1}, \mathbf{p}, \mathbf{q_2})U_\ell(\mathbf{q_2}, \mathbf{k_2}, \mathbf{k_3})\\ &\qquad + U_\ell(\mathbf{p}, \mathbf{k_1}, \mathbf{q_2})U_\ell(\mathbf{q_2}, \mathbf{k_2}, \mathbf{k_3})\\ &\qquad + U_\ell(\mathbf{k_1}, \mathbf{p}, \mathbf{q_2})U_\ell(\mathbf{k_2}, \mathbf{q_2}, \mathbf{k_3})\Big\} \quad (37)\end{aligned}$$

where $\ell = \ln(\Lambda_0/\Lambda)$, $\mathbf{k} = \mathbf{k}_1 + \mathbf{k}_2 - \mathbf{p}$, $\mathbf{q}_1 = \mathbf{p} + \mathbf{k}_2 - \mathbf{k}_3$, $\mathbf{q_2} = \mathbf{p} + \mathbf{k}_1 - \mathbf{k}_3$, and $G_{k\ell} = \Theta(|\xi_{\mathbf{k}}| - \Lambda)/(i\omega - \xi_{\mathbf{k}})$ with $\xi_{\mathbf{k}} = \epsilon_{\text{f},\mathbf{k}} - \mu_{\text{f}}$ and $k = (\omega, \mathbf{k})$.

From the general interaction vertices $U(\mathbf{k}_1, \mathbf{k}_2, \mathbf{k}_3)$, the specific interaction channels, such as charge-density wave (CDW), antiferromagnetic (AF), and superconducting (BCS), can be obtained:

$$V^{\text{CDW}} = 4\,U_{\text{c}}(\mathbf{k}_1, \mathbf{k}_2, \mathbf{k}_1 + \mathbf{Q})\,, \quad (38)$$

$$V^{\text{AF}} = 4\,U_\sigma(\mathbf{k}_1, \mathbf{k}_2, \mathbf{k}_1 + \mathbf{Q})\,, \quad (39)$$

$$V^{\text{BCS}} = U(\mathbf{k}_1, -\mathbf{k}_1, \mathbf{k}_2)\,, \quad (40)$$

where we have used the notation: $U_{\text{c}} = (2 - \hat{X})U/4$, $U_\sigma = -\hat{X}U/4$ with $\hat{X}U(\mathbf{k}_1, \mathbf{k}_2, \mathbf{k}_3) = U(\mathbf{k}_2, \mathbf{k}_1, \mathbf{k}_3)$, and $\mathbf{Q}$ is the nesting vector, $\mathbf{Q} = (\pi, \pi)$.

In a numerical implementation, one discretizes the Fermi surface into M patches, and hence each of the interaction channels (38), (39), (40) is represented by an $M \times M$ matrix. At each RG step, we diagonalize each of these matrices. The channel with the largest eigenvalue (with the caveat that a BCS-channel needs to be attractive to drive a transition) corresponds to the dominant order. The elements of the eigenvector are labeled by the discrete patch indices around the Fermi surface and the symmetry of the order parameter is given by this angular dependence.

The RG method for interacting fermions has been extended to also include retardation effects, as for the case of interacting electrons which are also coupled to phonons in a crystal [96,97]. In this case: (i) the interaction vertices also depend on frequencies of the incoming and outgoing fermions, so the RG equations are written for given external frequencies and the integral over intermediate frequencies can not be done analytically, and (ii) there are important self-energy corrections (in particular the imaginary part of the self-energy is non-zero). Eliashberg equations for strong-coupling superconductivity has been derived with this method [96,97] for the case of electrons, with a circular Fermi surface, coupled to phonons. This method has also been applied to other electron–phonon problems [49,94], and to mixtures of cold atoms in an optical lattice [50].

Phase Diagram and Sub-Dominant Orders

The microscopic parameters in the Hamiltonian (31) determine the initial conditions for the RG flow, and the shape of the Fermi surface. With these, we write the RG flow equations and solve them numerically. We first discuss the case without retardation. For some parameters,

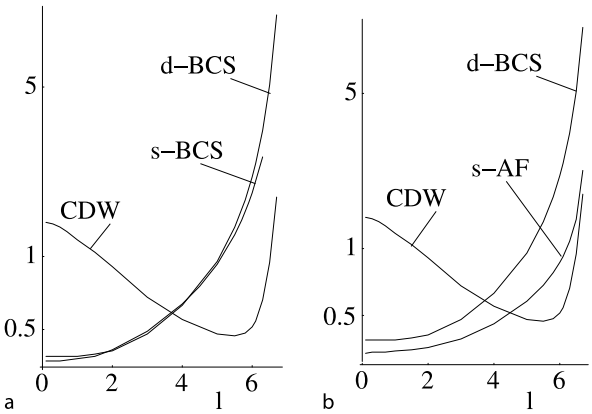

Ultracold Atomic Gases: Novel States of Matter, Figure 9
RG flow for the different effective interactions (in units of t_f) as a function of the RG parameter l ($\tilde{V}/t_f = 3$ and $\xi = 1$). a $U_{ff}/t_F = 0.5$; b $U_{ff}/t_f = 1.2$

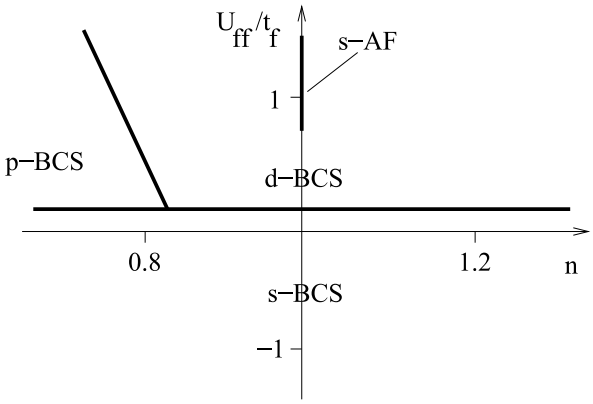

Ultracold Atomic Gases: Novel States of Matter, Figure 10
Phase diagram, interaction strength, U_{ff}/t_f, versus number of fermions per site, n, for a Fermi–Bose mixture in a square lattice in 2D ($\tilde{V}/t_f = 2$, $\xi = 1$)

we encounter a divergence in the RG flow, indicating the onset of ordering with a gap that is in the detectable regime, i. e. larger than $10^{-3} t_f$. In other regimes, where such a divergence is not reached, one can read off the dominant tendency of the RG flow. In Fig. 9 we show examples of RG flows as a function of ℓ. In Fig. 9a, we show the competition between d-wave and s-wave pairing, with d-wave being dominant and s-wave being subdominant. In Fig. 9b we show an example with dominant d-wave channel and subdominant AF channel. In both cases we find that for short distances (or high energies) CDW fluctuations are dominant, giving rise to a state that resembles the findings for high-T_c superconductors [33,34,99]. In some situations the many-body states are almost degenerate and small changes in the initial conditions (that is, changes in the form of the interactions) can be used to select one particular ground state.

With this procedure we determine the phase diagram of the system, which is shown in Fig. 10. We now discuss the general features of the phase diagram. In the absence of any coupling to the bosons, i. e. for $\tilde{V} = 0$, the system shows s-wave pairing for attractive interaction, $U_{ff} < 0$, and no ordering for $U_{ff} > 0$, i. e. Fermi liquid behavior, except for the special case of half-filling where Fermi surface nesting drives the system to AF order for repulsive interactions, and to s-wave pairing (degenerate with CDW) for attractive interaction. If we now turn on the interaction to the bosons, this picture is modified in the following way: The boundary of the s-wave regime is moved into the regime of positive U_{ff}, approximately to a value of U_{ff} where the effective interaction at the nesting vector $\mathbf{Q}$ between the fermions, $U_{ff} + V_{\text{ind.},\mathbf{Q}}$, is positive, i. e. for $U_{ff} \approx \tilde{V}/(1 + 8\xi^2)$. On the repulsive side, and away from half-filling, we find the tendency to form a paired state, either d-wave or p-wave. This tendency becomes weaker the further the system is away from half-filling. We typically find a gap in the vicinity of half-filling and further away from $\mu = 0$ we find only an increasing strength of the corresponding interaction channel. For the half-filled system, we find that for attractive interactions the degeneracy between s-wave pairing and CDW ordering is lifted, with s-wave pairing being the remaining type of order. For repulsive interactions, we find an intermediate regime of d-wave pairing, and for larger values of U_{ff} we obtain AF order.

The RG approach also allows the extraction of the many-body gaps in the system through a "poor man's scaling" analysis of the divergent flow: at the point where the coupling becomes of order of t_f the scaling parameter ℓ reaches the maximum value $\ell_c = \ln(t_f/\Delta)$, where Δ is the value of the gap. Hence, $\Delta/t_f \approx \exp\{-\ell_c\}$ can be obtained from the RG flows such as the ones in Fig. 9. In Fig. 11 we show the gaps of the problem as a function of U_{ff}/t_f in the half-filled case. One can see that as U_{ff} increases, from negative to positive values, the s-wave gap is replaced by a d-wave gap, and finally for an antiferromagnetic gap. As is apparent from this figure, the gap in the d-wave phase is much smaller than the gaps of the AF order and the s-wave pairing, and, furthermore, almost independent of the value of U_{ff}. The latter is the case because the U_{ff} term is a pure s-wave contribution to the interaction and therefore does not contribute to the d-wave channel. The d-wave channel has an initial contribution which is entirely due to the anisotropy of the induced interaction,

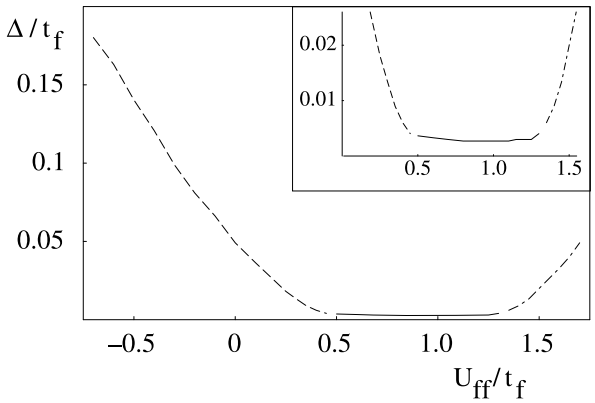

Ultracold Atomic Gases: Novel States of Matter, Figure 11
Many-body energy gaps at half-filling ($\mu = 0$), as a function of U_{ff}/t_f, for $\tilde{V}/t_f = 3$ and at a fixed value of the coherence length $\xi = 1$. *Dashed line*: *s*-wave gap; *continuous line*: *d*-wave gap; *dotted-dashed line*: antiferromagnetic gap. The *inset* shows a magnified plot of the *d*-wave regime

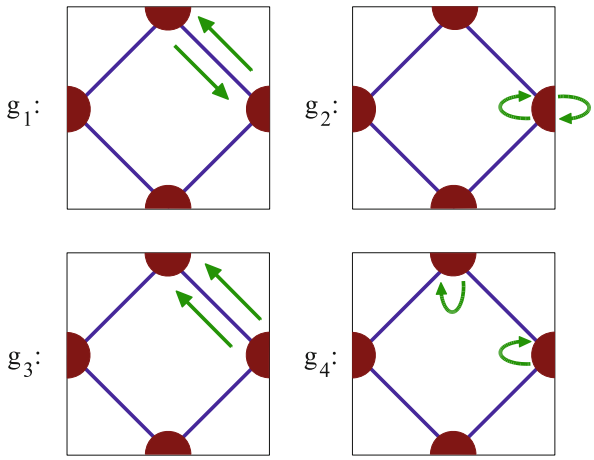

Ultracold Atomic Gases: Novel States of Matter, Figure 12
Relevant processes in the two-patch approximation

which gives only a small value, and as a consequence only a small value for the gap. The value of the gap (in units of t_f) can be numerically fitted with a BCS expression of the form $a\exp(-b/\tilde{V})$, with the parameters a and b given by $a = 0.31$ and $b = 14.2$.

For a system of spinless fermions, one can simply suppress one of the spin indices in (31) and (32). In this case there is a major simplification in the problem since U_{ff} is absent: in a spinless problem there can be only one fermion per site, as per Pauli's principle. Hence, in the absence of bosons, the spinless gas is non-interacting. The bosons, however, mediate the interaction between the fermions. Since the fermions are in different lattice sites the pair wavefunction has necessarily a node and hence, no *s*-wave pairing is allowed. In other words, in the spinless case the anti-symmetry of the wavefunction requires pairing in an odd angular momentum channel. In fact, we find that throughout the entire phase diagram the fermions develop *p*-wave pairing. At half-filling we find a similar behavior of CDW fluctuations on short scales, analogous to the flow shown in Fig. 9. One should point out that in real solids the conditions of "spinlessness" behavior is hard to achieve since it usually requires complete polarization of the electron gas, that is, magnetic energies of the order of the Fermi energy (a situation experimentally difficult to achieve in good metals). However, in cold atom lattices this situation can be easily accomplished with the correct choice of atoms.

Finally, when retardation is important, the numerical task of solving the RG flow equations become much more demanding. In addition to the discretization of the Fermi surface, one has to also discretize the frequency (for $T = 0$), or consider a certain number of Matsubara frequencies ($T \neq 0$). This has been done for this Bose–Fermi system only for a fixed density of fermions corresponding to one half [50]. In this case the Fermi surface has a diamond shape and scattering processes are dominated by the van Hove points (corners of the diamond) where the density of states is singular. The Fermi surface can therefore be approximated by the van Hove points only [86] so that he types of relevant processes are reduced, as shown in Fig. 12. Each of the processes still depend on frequencies: $g_i(\omega_1, \omega_2, \omega_3)$, for $i = 1, 2, 3, 4$. The phase diagram is shown in Fig. 13. Retardation leads to additional phases at half-filling and by tuning the lattice parameters, the system undergoes AF (or spin-density-wave SDW), *d*-wave SC pairing, *s*-wave-pairing, and CDW. In the limit of $v_b \gg v_f$ discussed previously, when retardation is not important, CDW does not become dominant (Fig. 10). It is at most degenerate with *s*-wave pairing for $U_{ff} < 0$. As the bosons become slower, there is stronger tendency for CDW formation (Fig. 13).

Quantum Frustration in Triangular Lattices

It is known that the geometric shape of the lattice is a crucial factor in determining the properties of interacting many-body systems. For instance, localized spins interacting antiferromagnetically on a triangular lattice suffer from the phenomenon of *frustration*, when antiferromagnetic order cannot be achieved because of the particular lattice structure. For itinerant fermionic systems, the lattice structure, together with the dispersion relation and the filling fraction, determine the shape of the

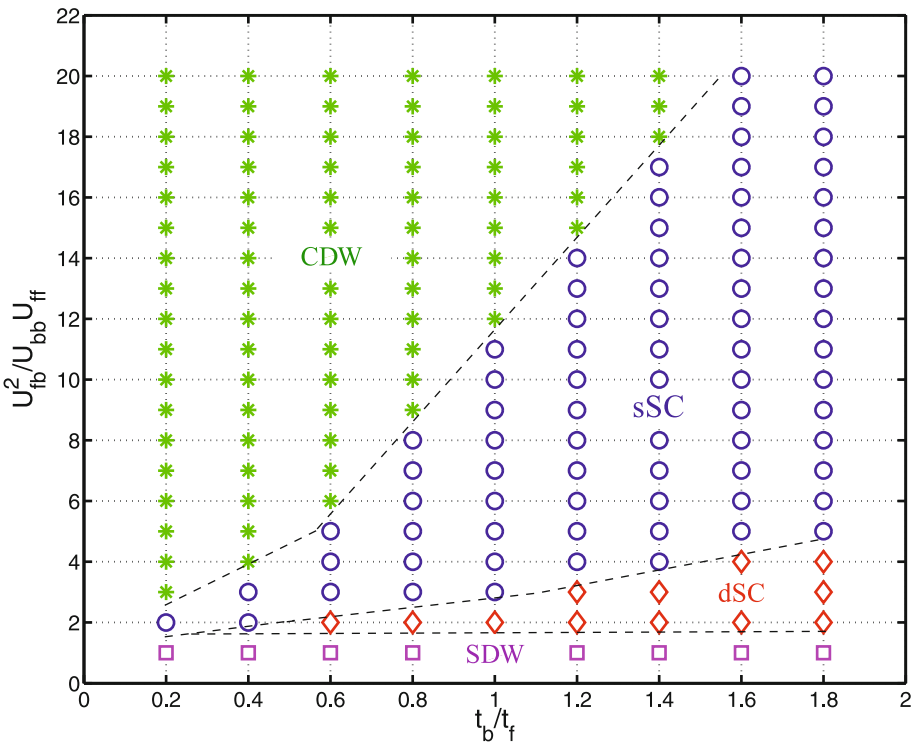

Ultracold Atomic Gases: Novel States of Matter, Figure 13
Phase diagram for $U_{ff} = 0.4t_f$, $U_{bb} = 0.8t_f$, and $n_b = 2.5$. *Blue circles* indicate *s*-wave SC, *red rhombuses* indicate *d*-wave SC, *magenta squares* AF (also called spin-density-wave SDW), and *green stars* CDW type of ordering. *Dashed lines* are guides to the eye

Fermi surface. The Fermi surface, by its turn, is a crucial factor in determining what type of orders the system can develop. Indeed, for the triangular lattice we consider in this section, which shows a rich and subtle competition between superconducting phases with different symmetries, small changes in the shape of the FS determine which pairing symmetry is dominant. This is a reflection of the "lattice frustration" on the superconducting phases. In solids, this intriguing lattice geometry is realized in materials such as cobaltates [93], transition metal dichalcogenides [105] and κ-(ET)$_2$X layered organic crystals [40] (if each lattice site is represented by one ET dimer [46]), and has been the subject of several theoretical studies [5,13,20,35,54,95,103,107].

In this section we consider a BFM on a triangular lattice. The geometry of the lattice under consideration here is shown in Fig. 15a. This system is described by a similar Hubbard model as for the square lattice. But now, besides the triangular geometry, we allow for two different values for the hopping amplitudes, for two types of lattice bonds, as indicated in Fig. 15a by dashed and continuous lines. $t_{f,a}$ and $t_{b,a}$ with $a = 1, 2$ are the fermionic and bosonic tunneling amplitudes between neighboring sites, where the index $a = 1$ ($a = 2$) refers to the continuous (dashed) bonds. For the description of the isotropic case we equate $t_{b/f,1}$ and $t_{b/f,2}$, and define $t_f \equiv t_{f,1} = t_{f,2}$ and $t_b \equiv t_{b,1} = t_{b,2}$. μ_f (μ_b) is the chemical potential for fermions (bosons), U_{bb}, U_{ff}, and U_{bf} are the on-site boson-boson, fermion–fermion and boson–fermion repulsion energy, respectively.

Just as for the case of a square lattice, we consider the limit of weakly interacting bosons, in which the bosons form a BEC, for which we use the same description. The resulting dispersion relation is now given by $\omega_{\mathbf{k}} = \sqrt{(\epsilon_{b,\mathbf{k}} - \epsilon_{b,0})(\epsilon_{b,\mathbf{k}} - \epsilon_{b,0} + 2U_{bb}n_b)}$, where the bare lattice dispersion is given by:

$$\begin{aligned}\epsilon_{b,k} = &- t_{b,1} 2\cos k_x \\ &- t_{b,2}(2\cos(k_x/2 + \sqrt{3}k_y/2) \\ &+ 2\cos(k_x/2 - \sqrt{3}k_y/2))\,.\end{aligned} \tag{41}$$

For small values of k_x and k_y, $\omega_{\mathbf{k}}$ can be expanded as: $\omega_{\mathbf{k}} \sim \sqrt{((2t_{b,1} + t_{b,2})k_x^2 + 3t_{b,2}k_y^2)U_{bb}n_b}$, which gives us

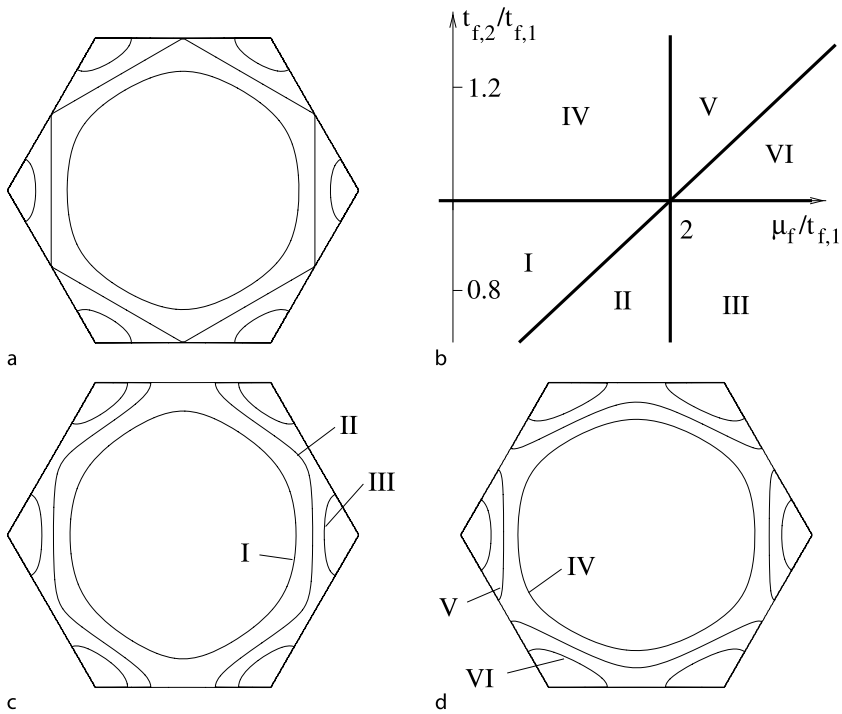

Ultracold Atomic Gases: Novel States of Matter, Figure 14

a Fermi surfaces for an isotropic lattice, for $\mu_f < 2t_{f,1/2}$, $\mu_f = 2t_{f,1/2}$ (*hexagonal shape*), and $\mu_f > 2t_{f,1/2}$ (*six disjoint arcs*). b Diagram of the different types of Fermi surfaces that can be created on an anisotropic lattice, by varying the ratio $t_{f,2}/t_{f,1}$ and μ_f. c Fermi surfaces for $t_{f,2} < t_{f,1}$, for $\mu_f < 4t_{f,2} - 2t_{f,1}$, $4t_{f,2} - 2t_{f,1} < \mu_f < 2t_{f,1}$, and $\mu_f > 2t_{f,1}$, corresponding to the regimes I–III, respectively. d Fermi surfaces for $t_{f,2} > t_{f,1}$, for $\mu_f < 2t_{f,1}$, $2t_{f,1} < \mu_f < 4t_{f,2} - 2t_{f,1}$, and $\mu_f > 4t_{f,2} - 2t_{f,1}$, corresponding to the regimes IV–VI, respectively

the two velocities $v_{b,x} = \sqrt{(2t_{b,1} + t_{b,2})U_{bb}n_b}$ and $v_{b,y} = \sqrt{3t_{b,2}U_{bb}n_b}$.

We again assume that these velocities of the condensate fluctuations are much larger than the Fermi velocity, which corresponds to the conditions $v_{b,x/y} > t_{f,1/2}$. Therefore, large bosonic hopping amplitudes, a bosonic density of $\approx 1-3$, and some intermediate value for $t_{f,1/2}$ will satisfy this requirement. As before, the bosonic modes can be integrated out, and we obtain an approximately non-retarded fermion–fermion interaction. The induced potential $V_{\text{ind.},\mathbf{k}}$ is given by: $V_{\text{ind.},\mathbf{k}} = -\tilde{V}/(1+\xi_1^2(2-2\cos k_x)+\xi_2^2(4-4\cos(k_x/2)\cos(\sqrt{3}k_y/2)))$ with $\tilde{V} = U_{bf}^2/U_{bb}$, and ξ_a are the healing lengths of the Bose–Einstein condensate (BEC) and are given by $\xi_a = \sqrt{t_{b,a}/2n_bU_{bb}}$ with $a = 1, 2$. We again arrive at a purely fermionic, non-retarded description of the same form as before. This is the effective model that we study with a numerical implementation of the functional renormalization group. For the isotropic case, perfect nesting occurs at 3/4-filling, with three possible nesting vectors: $\mathbf{Q}_1 = (0, 2\pi)$, $\mathbf{Q}_2 = (\pi, \sqrt{3}\pi)$, and $\mathbf{Q}_3 = (-\pi, \sqrt{3}\pi)$, leading to three different possible types of instabilities per density wave channel. For the anisotropic case, only $\mathbf{Q}_1$ can be a nesting vector, for the condition $\mu_f = 2t_{f,1}$. To determine the scale of the gaps, Δ, associated with each of these order parameters, we again use a 'poor man's' scaling estimate, specifically: $\Delta \approx \Lambda_0 e^{-\ell_c}$, where ℓ_c is the point at which the RG flow diverges and the instability occurs.

The RG is implemented numerically by discretizing the FS into M patches. For the results shown in this section, $M = 24$ or 36 was used. The CDW, AF and BCS channels are diagonalized at each RG step. The dominant instability is the channel that has an eigenvalue (divided by the dimension of the matrix) with the largest magnitude (for BCS one has to ensure that such eigenvalue is negative so that the channel is attractive). Each element of the corresponding eigenvector represents a given FS patch, and hence, the symmetry of the dominant order parameter is reflected on the patch (i. e., angular) dependence of each element around the FS. Using this method, we determine the phase diagram of the system in various limits.

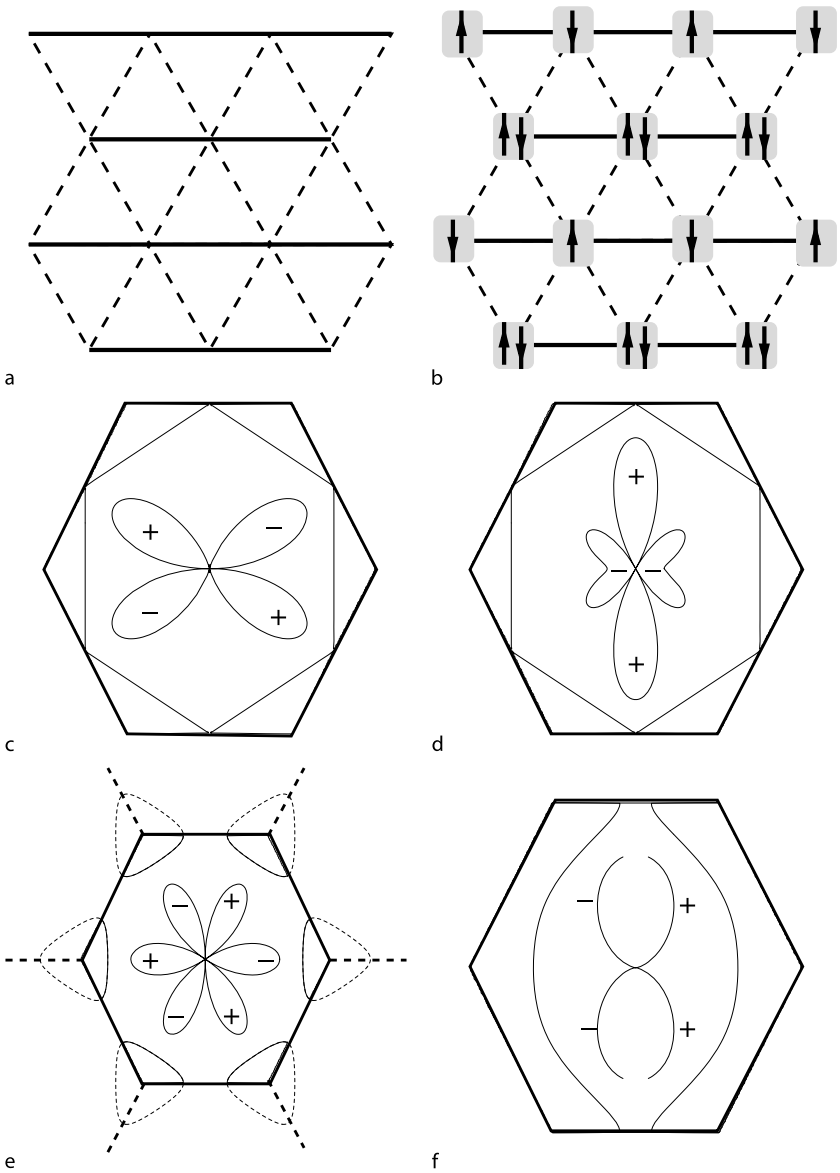

Ultracold Atomic Gases: Novel States of Matter, Figure 15

a Lattice geometry of the system. The continuous (*dashed*) bonds correspond to the hopping amplitudes $t_{b/f,1(2)}$. For $t_{b/f,1} = t_{b/f,2}$, the lattice is an isotropic triangular lattice. b schematic representation of the AF order corresponding to nesting vector Q_1. c, d Order parameters of the extended *d*-wave orders D_1 and D_2. e Order parameter of the *f*-wave phase. This order can also be interpreted as two *s*-wave paired hole states whose order parameters are out of phase by π. f Order parameter of the extended *p*-wave phase, that appears in anisotropic lattices

We first consider spin-1/2 fermions on an isotropic triangular lattice, i. e. with $t_{f,1} = t_{f,2} \equiv t_f$. The FS for such a lattice behaves as follows: For small filling the FS consists of one near-circular piece, which then approaches the shape of a hexagon as μ_f approaches the special value $\mu_f = 2t_f$. At this special chemical potential, which corresponds to 3/4-filling, the FS is nested with the three distinct nesting vectors $\mathbf{Q}_i$. For filling fractions larger than 3/4 the FS breaks into six disjoined arcs. Examples for these different regimes are shown in Fig. 14a. Without coupling to the BEC, the fermions form an *s*-wave pairing phase for attractive interactions, and a Fermi liquid phase for repulsive interactions (ignoring high angular momentum pairing phases predicted by the Kohn–Luttinger the-

orem [53] which would occur at energy scales much lower than the experimentally accessible regime), except for the specific case $\mu_f = 2t_f$, where the system shows AF order for repulsive interactions. A schematic picture of this order is shown in Fig. 15b for the nesting vector $\mathbf{Q}_1$. This behavior is similar to the one found for isotropic square lattice in the previous section [62]: *s*-wave pairing for attractive interaction, and Fermi liquid behavior for repulsive interaction, except at an special filling, for which we find AF order due to nesting. An interesting difference for the triangular lattice is the three-fold degeneracy of the AF phase, an indication of frustration.

When the coupling to the BEC is turned on, the isotropic triangular lattice shows a phase diagram of the type shown in Fig. 8. The *s*-wave pairing phase slightly extends into the regime of positive U_{ff}, because of the induced attractive interaction mediated by the bosonic fluctuations. The regime that showed Fermi liquid behavior in the absence of the induced interaction now shows a rich competition of various types of pairing. In the regime where the density is below half-filling, when the FS is approximately circular, the system shows *p*-wave pairing. For fillings larger than 3/4, when the FS consists of six disjoined parts, the fermions Cooper pair in a superconducting state with *f* symmetry. As shown in Fig. 15e, the FS in this regime can also be interpreted as two distinct near-circular Fermi surfaces of holes. In this interpretation each of these two fermionic systems is in an *s*-wave pairing phase, but the relative phase between the two order parameters is π. At 3/4-filling and large values of U_{ff}, the system still shows AF order. However, for smaller values of U_{ff}, and also for smaller fillings, two phases with degenerate extended *d* symmetry develop. These superconducting orders have a sizable *g*-wave component and are approximately given by:

$$\psi_{D_1} = \sin 2\theta + 0.5 \sin 4\theta \,, \tag{42}$$

$$\psi_{D_2} = \cos 2\theta - 0.5 \cos 4\theta \,. \tag{43}$$

These order parameters are shown in Fig. 15c and d. The shapes of the order parameters are energetically advantageous because, on the one hand, the order parameter maxima are located at points at which the system has a high density of states (the 'corners' of the FS). Hence, when the superconducting gap opens, there is a large gain of condensation energy coming from these regions on the FS. On the other hand, the *d*-wave state has lower kinetic energy than the *f*-wave, and hence is selected.

The phase diagram Fig. 8 has a number of similarities to the phase diagram for a BFM on a square lattice, such as

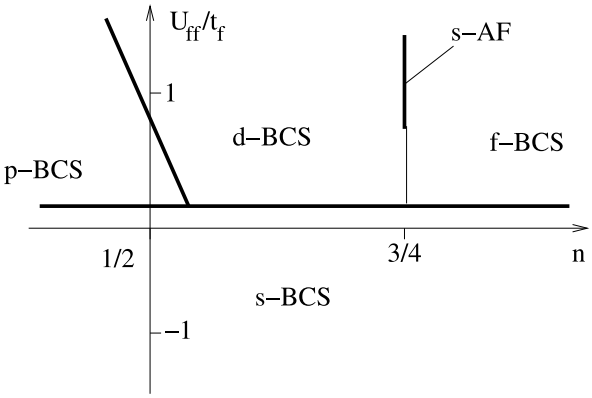

Ultracold Atomic Gases: Novel States of Matter, Figure 16
Phase diagram of a Bose–Fermi mixture on a 2D isotropic triangular lattice. The *vertical axis* corresponds to the interaction strength, U_{ff}/t_f, whereas the *horizontal axis* corresponds to the filling fraction of the fermions per site, *n*. The other parameters are given by $\tilde{V}/t_f = 3$, and $\xi_a = 1$ with $a = 1, 2$

the *s*- and the *p*-wave pairing phase, and the existence of AF order for a nested Fermi surface for large U_{ff}.

However, the competition of pairing orders for positive U_{ff} and intermediate and large filling is much richer, due to the more complex shape of the Fermi surface.

The energy gaps associated with these order parameters can be determined as we did in the previous section [62], by using a 'poor man's' scaling argument. We find for the *s*-wave pairing and the AF order, that they are around $0.1T_F$, where T_F is the Fermi temperature of the system. For most of the exotic phases, we energy gaps of the order of $0.01 - 0.001T_F$.

We now consider a BFM with spin-1/2 fermions on an anisotropic triangular lattice, i. e. with unequal hopping amplitudes, $t_{f(b),1} \neq t_{f(b),2}$. The shape of the FS behaves as follows: For $t_{f,2} > t_{f,1}$, as one increases the chemical potential, the FS first breaks into four arcs at $\mu_f = 2t_{f,1}$, and then breaks into six arcs at $\mu_f = 4t_{f,2} - 2t_{f,1}$, corresponding to the regimes IV–VI, in Fig. 14b and d. For $t_{f,2} < t_{f,1}$ the FS first breaks into two arcs at $\mu_f = 4t_{f,2} - 2t_{f,1}$, and then breaks into six arcs at $\mu_f = 2t_{f,1}$ corresponding to the regimes I–III, in Fig. 14b and c. At the special chemical potential $\mu_f = 2t_{f,1}$ the FS is still nested, but there is only one nesting vector along the direction of the bonds with hopping amplitude $t_{f,1}$. In the absence of the coupling to the BEC the phase diagram has a similar structure as for the isotropic case: *s*-wave pairing for attractive interaction, Fermi liquid behavior for repulsive interaction, with the exception of the nested FS at $\mu_f = 2t_{f,1}$ where one finds AF order (notice that in this case the filling is not 3/4).

When the coupling to the bosons is turned on, one generates an even more complicated competition of

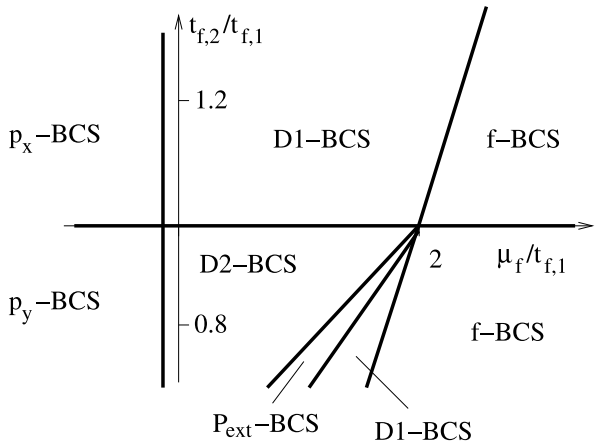

Ultracold Atomic Gases: Novel States of Matter, Figure 17
Phase diagram of a Bose–Fermi mixture on an anisotropic triangular lattice. The *vertical axis* corresponds to the ratio $t_{f,2}/t_{f,1}$, the *horizontal axis* corresponds to the chemical potential μ_f. The other parameters are given by $\tilde{V}/t_f = 3$, $U_{ff}/t_{f,1} = 2$, and $\xi_a = 1$ with $a = 1, 2$)

pairing phases for repulsive U_{ff} in the vicinity of the point $\mu_f = 2t_{f,1}$, as is shown in Fig. 17. Generally, for unequal hopping the degeneracy between D_1 and D_2 in (43), as well as p_x and p_y is lifted: In the regime with $t_{f,2} > t_{f,1}$ ($t_{f,2} < t_{f,1}$), D_1 (D_2) and p_x (p_y) dominate. For $t_{f,2} > t_{f,1}$, in the intermediate regime, in which the FS consists of four disjoined arcs, corresponding to the regime V in Fig. 14, the type of ordering changes from D_1 to f. For $t_{f,2} < t_{f,1}$, the type of pairing also eventually becomes f-wave, but first develops two other types of pairing, in the regime II in Fig. 14. Firstly, one finds an unusual extended p-wave symmetry, which is schematically shown in Fig. 15f. Its wavefunction is of the form:

$$\psi_{P_{ext}} = \begin{cases} \sin^2\theta & -\pi/2 < \theta < \pi/2 \\ -\sin^2\theta & \pi/2 < \theta < 3\pi/2\,. \end{cases} \tag{44}$$

The second type of pairing that appears before the system develops f-wave pairing is D_1. These unusual pairing states are energetically favorable because of the anisotropic shape of the FS. For the regime in which the FS has just barely broken up into two arcs, the order parameter assumes p-wave symmetry and the maxima are located along the y-axis, where the density of states is highest. As the region of open FS widens (see Fig. 15f), this pairing becomes energetically unfavorable, and the system develops D_1-pairing, so that the maxima of the order parameter can again be located near the point of highest density of states. The energy gaps associated with these order parameters are of the same order of magnitude as for the isotropic lattice.

Finally, we consider a BFM with spinless fermions on an isotropic lattice. Due to the absence of s-wave scattering between fermions of the same spin state, there is no direct interaction, that is, $U_{ff} = 0$. Hence, in the absence of bosons, the spinless gas is non-interacting. The boson fluctuations, however, mediate an induced interaction between the fermions. Due to the anti-symmetry of the Cooper pair wavefunction, pairing occurs in an odd angular momentum channel. We find a competition between p and f-wave pairing symmetry. For small to intermediate filling ($n < 0.65$), p-wave pairing dominates. For larger fillings, for which the FS first approaches the shape of a hexagon and then breaks up into six arcs, the system shows f-wave pairing. Since these larger fillings of fermions are typically realized in the center of an atomic trap, this result would suggest a comparatively easy way to create an exotic pairing state experimentally. In contrast to this, a spinless BFM on a square lattice only shows p-wave pairing, since for the quadrangular shape of its FS, channels of higher angular momentum are of no advantage energetically.

The many-body states discussed in this section can be observed through various methods: AF order could be revealed in time-of-flight images and Bragg scattering [91], noise correlations [3,18,29,61] can be used to detect the various pairing phases, laser stirring experiments [72,82] can be used to detect the phase boundary between AF order and pairing. The short-scale CDW fluctuations should give a signature in a photo-association measurement. RF spectroscopy [12] can be used to quantify the gaps of the various phases.

Conclusions

In this article we studied the phase diagrams of various low-dimensional ultra-cold atom systems. In Sect. "One-Dimensional Lattices" we studied atomic mixtures in one dimension, using Luttinger liquid theory. We argued that a Bose–Fermi mixture can be naturally looked at as a Luttinger liquid of polarons, and we discussed the rich phase diagrams of commensurate mixtures. In Sect. "Phase-Locking Transition of Coupled Low-Dimensional Superfluids", we studied the phases of two coupled two-dimensional superfluids at finite temperature. We found that the critical temperature of the phase-locked phase is significantly increased over its bare value, which we propose to use for realizing the Kibble–Zurek mechanism. When interactions between the two superfluids are present, we find additional phases which are partially superfluid, and partially disordered. In Sect. "Bose–Fermi Mixtures in Two-Dimensional Optical Lattices", we used

the powerful method of functional renormalization group equations to determine the phases of Bose–Fermi mixtures in two-dimensional optical lattices. We found an intricate competition of orders, including new types of exotic pairing for triangular lattices. In all these sections, ideas how to probe our predictions were also given.

Bibliography

Primary Literature

1. Albus AP et al (2003) Phys Rev A67:063606
2. Alexandrov AS, Mott SN (1995) Polarons and Bipolarons. World Scientific, Singapore
3. Altman E, Demler E, Lukin M (2004) Probing many-body states of ultracold atoms via noise correlations. Phys Rev A 70:013603
4. Anderson MH, Ensher JR, Matthews MR, Wieman CE, Cornell EA (1995) Observation of Bose–Einstein condensation in a dilute atomic vapor below 200 nanokelvin. Science 269:198
5. Baskaran G (2003) Electronic model for CoO_2 layer based systems: chiral resonating valence bond metal and superconductivity. Phys Rev Lett 91:097003
6. Benfatto L et al (2007) Kosterlitz-Thouless behavior in layered superconductors: the role of the vortex-core energy. arXiv:cond-mat/0609287
7. Bijlsma MJ et al (2000) Phys Rev A 61:053601
8. Cazalilla MA (2004) Phys J B 37:1–47
9. Cazalilla MA, Ho AF (2003) Phys Rev Lett 91:150403
10. Cazalilla MA, Ho AF, Giamarchi T (2005) Phys Rev Lett 95:226402
11. Chaikin PM, Lubensky TC (1995) Principles of condensed matter physics. Cambridge University Press, Cambridge
12. Chin C, Bartenstein M, Altmeyer A, Riendl S, Jochim S, Hecker Denschlag J, Grimm R (2004) Observation of the pairing gap in a strongly interacting Fermi gas. Science 305:1128
13. Choy TP, Galanakis D, Phillips P (2007) Proposed insulating ground state of $Na_{0.5}CoO_2$: Squaring the triangle. Phys Rev B 75:073103
14. Davis KB, Mewes M-O, Andrews MR, NJ van Druten, Durfee DS, Kurn DM, Ketterle W (1995) Bose–Einstein condensation in a gas of sodium atoms. Phys Rev Lett 75:3969
15. de Pue MT, McCormick C, Winoto SL, Oliver S, Weiss DS (1999) Unity occupation of sites in a 3D optical lattice. Phys Rev Lett 82:2262
16. Engelsberg S, Varga BB (1964) Phys Rev 136:A1582
17. Fertig CD et al (2004) Strongly inhibited transport of a 1D Bose gas in a lattice. arXiv:cond-mat/0410491
18. Fölling S, Gerbier F, Widera A, Mandel O, Gericke T, Bloch I (2005) Spatial quantum noise interferometry in expanding ultracold atom clouds. Nature 434:481
19. Fuchs JN, Recati A, Zwerger W (2004) Phys Rev Lett 93:090408
20. Gan JY, Chen Y, Zhang FC (2006) Superconducting pairing symmetries in anisotropic triangular quantum antiferromagnets. Phys Rev B 74:094515
21. Gensemer SD, Jin DS (2001) Phys Rev Lett 87:173201
22. Giamarchi T (2004) Quantum Physics in one dimension. Clarendon Press, Oxford
23. Görlitz A et al (2001) Phys Rev Lett 87:130402
24. Gogolin AO, Nerseyan AA, Tsvelik AM (1998) Bosonization and Strongly Correlated Systems. Cambridge University Press, Cambridge
25. Goldwin J, Inouye S, Olsen ML, Newman B, DePaola BD, Jin DS (2004) Measurement of the interaction strength in a Bose–Fermi mixture with ^{87}Rb and ^{40}K. Phys Rev A 70:021601
26. Greiner M, Bloch I, Mandel O, Hänsch TW, Esslinger T (2001) Exploring phase coherence in a 2D lattice of Bose–Einstein condensates. Phys Rev Lett 87:160405
27. Greiner M, Mandel O, Esslinger T, Hänsch TW, Bloch I (2002) Quantum phase transition from a superfluid to a Mott insulator in a gas of ultracold atoms. Nature 415:39
28. Greiner M, Regal CA, Jin DS (2003) Emergence of a molecular Bose–Einstein condensate from a Fermi gas. Nature 426:537
29. Greiner M, Regal CA, Stewart JT, Jin DS (2005) Probing pair-correlated fermionic atoms through correlations in atom shot noise. Phys Rev Lett 94:110401
30. Hadzibabic Z, Krüger P, Cheneau M, Battelier B, Dalibard JB (2006) Nature 441:1118
31. Hadzibabic Z, Stock S, Battelier B, Bretin V, Dalibard J (2004) Phys Rev Lett 93:180403
32. Haldane FDM (1981) Phys Rev Lett 47:1840
33. Hanaguri T, Lupien C, Kohsaka Y, Lee D-H, Azuma M, Takano M, Takagi H, Davis JC (2004) A 'checkerboard' electronic crystal state in lightly hole-doped $Ca_{2-x}Na_xCuO_2Cl_2$. Nature 430:1001
34. Hoffman JE, Hudson EW, Lang KM, Madhavan V, Eisaki H, Uchida S, Davis SC (2002) A four unit cell periodic pattern of quasi-particle states surrounding vortex cores in $Bi_2Sr_2CaCu_2O_{8+\delta}$. Science 295:466
35. Honerkamp C (2003) Instabilities of interacting electrons on the triangular lattice. Phys Rev B 68:104510
36. Hubbard J (1963) Electron correlations in narrow energy band. Proc Soc R Lond A276:238
37. Isacsson A, Girvin SM (2005) Phys Rev A 72:053604
38. Isacsson A, Cha M-C, Sengupta K, Girvin SM (2005) Phys. Rev. B 72:184507
39. Jaksch D, Bruder C, Cirac JI, Gardiner CW, Zoller P (1998) Cold bosonic atoms in optical lattices. Phys Rev Lett 81:3108
40. Jérome D (1991) The physics of organic superconductors. Science 252:1509
41. Jo G-B, Shin Y, Will S, Pasquini TA, Saba M, Ketterle W, Pritchard DE, Vengalattore M, Prentiss M (2007) Long phase coherence time and number squeezing of two Bose–Einstein condensates on an atom chip. arXiv:cond-mat/0608585
42. Jochim S, Bartenstein M, Altmeyer A, Hendl G, Riedl S, Chin C, Denschlag JH, Grimm R (2003) Science 302:2101
43. Jones K, Julienne P, Lett P, Phillips WD, Tiesinga E, Williams C (1996) Measurement of the atomis Na(3P) lifetime and of retardation in the interaction between two atoms bound in a molecule. Europhys Lett 35:85
44. Kane C, Fisher MPA (1992) Phys Rev Lett 68:1220
45. Kibble TWB (1976) Phys J A 9:1387
46. Kino H, Fukuyama H (1995) Electronic states of conducting organic κ-(BEDT-TTF)$_2$. Phys XJ Soc Jpn 64:2726
47. Kinoshita T, Wenger T, Weiss DS (2004) Science 305:1125
48. Kitaev AY (2000) Unpaired Majorana fermions in quantum wires. arXiv:cond-mat/0010440
49. Klironomos FD, Tsai S-W (2006) Phonon-mediated tuning of instabilities in the Hubbard model at half-filling. Phys Rev B 74:205109
50. Klironomos FD, Tsai S-W (2007) Pairing and density-wave

phases in Boson–Fermion mixtures at fixed filling. arXiv:cond-mat/0702660
51. Kogut JB (1979) Rev Mod Phys 51:659
52. Köhl M, Moritz H, Stöferle T, Günter, Esslinger T (2005) Fermionic atoms in a three dimensional optical lattice: observing Fermi surfaces, dynamics, and interactions. Phys Rev Lett 94:080403
53. Kohn W, Luttinger JM (1965) New mechanism for superconductivity. Phys Rev Lett 15:524
54. Lee S-S, Lee PA (2005) $U(1)$ Gauge theory of the Hubbard model: spin liquid states and possible application to κ-(BEDT-TTF)$_2$Cu$_2$(CN)$_3$. Phys Rev Lett 95:036403
55. Lett PD, Julienne PS, Phillips WD (1995) Photoassociative spectroscopy of laser-cooled atoms. Annu Rev Phys Chem 46:423
56. Maddaloni P et al (2000) Phys Rev Lett 85:2413
57. Mahan GD (1990) Many-particle physics. Plenum Press, New York
58. Mandel O, Greiner M, Widera A, Rom T, Hänsch TW, Bloch I (2003) Phys Rev Lett 91:010407
59. Mandel O, Greiner M, Widera A, Rom T, Hänsch TW, Bloch I (2003) Nature 425:937
60. Mathey L, Wang D-W, Hofstetter W, Lukin MD, Demler E (2004) Luttinger liquid of polarons in one-dimensional boson–fermion mixtures. Phys Rev Lett 93:120404
61. Mathey L, Altman E, Vishwanath A (2008) Noise correlations in one-dimensional systems of ultra-cold fermions. Phys Rev Lett 100:240401
62. Mathey L, Tsai S-W, Castro Neto AH (2006) Competing types of order in two-dimensional Bose–Fermi mixtures. Phys Rev Lett 97:030601
63. Mathey L (2007) Commensurate mixtures of ultra-cold atoms in one dimension. Phys Rev B 75:144510
64. Mathey L, Wang D-W (2007) Phase diagrams of one-dimensional Bose–Fermi mixtures of ultra-cold atoms. Phys Rev A 75:013612
65. Mathey L, Tsai S-W, Castro Neto AH (2007) Exotic superconducting phases of ultracold atom mixtures on triangular lattices. Phys Rev B 75:144510
66. Mathey L, Polkovnikov A, Castro Neto AH (2008) Phase-locking transition of coupled low-dimensional superfluids. Europhys Lett 81:10008
67. Mckenzie RH (1997) Similarities between organic and cuprate superconductors. Science 278:820
68. Modugno G, Roati G, Riboli F, Ferlaino F, Brech RJ, Inguscio M (2002) Collapse of a degenerate Fermi gas. Science 297:2240
69. Modugno G, Ferlaino F, Heidemann R, Roati G, Inguscio M (2003) Production of a Fermi gas of atoms in an optical lattice. Phys Rev A 68:011601
70. Moritz H, Stöferle T, Günter K, Köhl M, Esslinger T (2005) Phys Rev Lett 94:210401
71. Mukhopadhyay R, Kane CL, Lubensky TC (2001) Phys Rev B 64:045120. CSO'Hern, Lubensky TC, Toner J (1999) Phys Rev Lett 83:2745
72. Onofrio R, Raman C, Vogels JM, Abo-Shaeer JR, Chikkatur AP, Ketterle W (1999) Observation of superfluid flow in a Bose–Einstein condensed gas. Phys Rev Lett 85:2228
73. Ospelkaus C, Ospelkaus S, Sengstock K, Bongs K (2006) Interaction-driven dynamics of ^{40}K-^{87}Rb fermion–boson gas mixtures in the large-particle-number limit. Phys Rev Lett 96:020401
74. Ospelkaus C, Ospelkaus S, Humbert L, Ernst P, Sengstock K, Bongs K (2006) Ultracold heteronuclear molecules in a 3optical D lattice. Phys Rev Lett 97:120402
75. Ospelkaus S, Ospelkaus C, Wille O, Succo M, Ernst P, Sengstock K, Bongs K (2006) Localization of bosonic atoms by fermionic impurities in a three-dimensional optical lattice. Phys Rev Lett 96:180403
76. Ospelkaus S, Ospelkaus C, Humbert L, Sengstock K, Bongs K (2006) Tuning of heteronuclear interactions in a degenerate Fermi–Bose mixture. Phys Rev Lett 97:120403
77. Paredes B, Widera A, Murg V, Mandel O, Foelling S, Cirac I, Shlyapnikov GV, Hänsch TW, Bloch I (2004) Nature 429:277
78. Partridge GB, et al (2005) Pairing and phase separation in a polarized fermi gas. arXiv:cond-mat/0511752
79. Phillips WD, Ekstrom C, Goldin W, Rolston SL (1996) Laser cooling of neutral atoms for frequency standards. In: Bergquist J (ed) Symposium on Frequency Standards and Metrology. World Scientific, Singapore, pp 5–10
80. Polkovnikov A, Altman E, Demler E (2006) Proc Natl Acad Sci USA 103:6125
81. Polkovnikov A (2005) Phys Rev B 72:161201(R). Zurek WH, Dorner U, Zoller P (2005) Phys Rev Lett 95:105701. Dziarmaga J (2005) Phys Rev Lett 95:245701
82. Raman C, Köhl M, Onofrio R, Durfee DS, Kuklewicz CE, Hadzibabic Z, Ketterle W (1999) Evidence for a critical velocity in a Bose–Einstein condensed gas. Phys Rev Lett 83:2502
83. Recati A, Fedichev PO, Zwerger W, Zoller P (2003) Phys Rev Lett 90:020401
84. Sadler LE et al (2006) Nature 443:312
85. Scherer DR et al (2006) Vortex formation by interference of multiple trapped Bose–Einstein condensates. arXiv:cond-mat/0610187
86. Schulz HJ (1987) Superconductivity and antiferromagnetism in the two-dimensional Hubbard model – scaling theory. Europhys Lett 4:609
87. Schumm T, Hofferberth S, Andersson LM, Wildermuth S, Groth S, Bar-Joseph I, Schmiedmayer J, Krüger P (2005) Nature Phys 1:57
88. Sengupta P, Pryadko LP (2005) Quantum degenerate Bose-Fermi mixtures on 1D optical lattices. arXiv:cond-mat/0512241
89. Shankar R (1994) Renormalization group approach to interacting fermions. Rev Mod Phys 68:129
90. Solyom J (1979) Adv. Phys 28:201
91. Stenger J, Inouye S, Chikkatur AP, Stamper-Kurn DM, Pritchard DE, Ketterle W (1999) Bragg spectroscopy of a Bose–Einstein condensate. Phys Rev Lett 82:4569
92. Stöferle T, Moritz H, Schori C, Köhl M, Esslinger T (2004) Transition from a strongly interacting 1D superfluid to a Mott insulator. Phys Rev Lett 92:130403
93. Takada K, Sakurai H, Takayama-Muromachi E, Izumi F, Dilanian RA, Sasaki T (2003) Nature 422:53
94. Tam K-M, Tsai S-W, Campbell DK, Castro Neto AH (2007) Retardation effects in the Holstein–Hubbard chain at half filling. Phys Rev B 75:161103
95. Tsai S-W, Marston JB (2001) κ-(BEDTTTF)$_2$X organic crystals: Superconducting versus anti-ferromagnetic instabilities in the Hubbard model on an anisotropic triangular lattice. Can. Phys J 79:1463
96. Tsai S-W, Castro Neto AH, Shankar R, Campbell DK (2005)

Renormalization group approach to strong-coupled superconductors. Phys Rev B 72:054531
97. Tsai S-W, Castro Neto AH, Shankar R, Campbell DK (2005) Renormalization group approach to superconductivity: from weak to strong electron–phonon coupling. Philos Mag 86:2631
98. Tsuchiya S, Griffin A (2003) Damping of Bogoliubov Excitations in Optical Lattices. arXiv:cond-mat/0311321
99. Vershinin M, Misra S, Ono S, Abe Y, Ando Y, Yazdani A (2004) Local ordering in the pseudogap state of the high-T_c superconductor $Bi_2Sr_2CaCu_2O_{8+\delta}$. Science 303:1995
100. Vichi L et al (1999) Phys Rev A 60:4734
101. Voit J, Schulz HJ (1987) Phys Rev B 36:968. ibid 37:10068 (1988)
102. Voit J (1995) Rep Prog Phys 58:977
103. Vojta M, Dagotto E (1999) Indications of unconventional superconductivity in doped and undoped triangular antiferromagnets. Phys Rev B 59:713
104. Wang D-W, Lukin MD, Demler E (2005) Engineering superfluidity in Bose–Fermi mixtures of ultracold atoms. Phys Rev A 72:(R)051604
105. Withers RL, Wilson JA (1986) An examination of the formation and characteristics of charge-density waves in inorganic materials with special reference to the two- and one-dimensional transition-metal chalcogenides. Phys J C 19:4809
106. Zanchi D, Schulz HJ (2000) Weakly correlated electrons on a square lattice: Renormalization-group theory. Phys Rev B 61:13609
107. Zhou A, Wang Z (2006) Charge and spin order on the triangular lattice – Na_xCoO_2 at $x = 0.5$. arXiv:cond-mat/0608068
108. Zurek WH (1985) Nature 317:505
109. Zwierlein MW, Stan CA, Schunck CH, Raupach SMF, Gupta S, Hadzibabic Z, Ketterle W (2003) Phys Rev Lett 91:250401
110. Zwierlein M et al (2005) Fermionic Superfluidity with Imbalanced Spin Populations and the Quantum Phase Transition to the Normal State. arXiv:cond-mat/0511197

Books and Reviews

Bloch I, Dalibard J, Zwerger W (2007) Many-body physics with ultracold gases. arXiv:0704.3011v1
Leggett AJ (2001) Bose–Einstein condensation in the alkali gases: Some fundamental concepts. Rev Mod Phys 73:307

Unconventional Computing, Introduction to

Andrew Adamatzky
University of the West of England, Bristol, UK

Unconventional Computing deals with computing and information processing derived from or implemented in physical, chemical and biological systems. As Toffoli said once "a computing scheme that today viewed as unconventional may well be so because its time hasn't come yet – or is already gone" [1].

Mechanical and analogue computers are characteristics representatives of such computing schemes. When mechanical computation concerned the unconventional computers can be traced back to many centuries old harmonic analyzers and synthesizers, Napier's bones, and Pascal's wheeled calculator, and they are revived recently in self-assembling devices and molecular machines (see ► Mechanical Computing: The Computational Complexity of Physical Devices).

In 1876 Lord Kelvin envisaged that a computation by directly exploiting law of Nature [2] and invented differential analyzer. Ideas of analog computation emerged, flourished, almost deceased by 1980s and then were resurrected in 1990s in ever growing field of computing based on continuous representations by means of continuous processes (see ► Analog Computation). This also branched into theory of computing with light and related continuous state machines (see ► Optical Computing).

Chemical and molecular media and substrates are now widely explored as prototypes of future non-standard computing devices. They can be classified into the following groups. First, models based interpretations of chemical reactions as computing processes, including autocatalytic polymer chemistries, chemistries inspired by Turing machines, lattice molecular systems (see ► Artificial Chemistry). Second, computers which utilize replication of macro-molecules. Here DNA and other polymer molecules are basic elements of computing devices, they solve Hamiltonian path problem, simulate implementation of chess problem, and binary arithmetic (see ► DNA Computing) and also molecular finite state machines, therapeutic and diagnostic automata (see ► Molecular Automata). Chemical computers of the third type compute by interactions between propagating diffusive and phase wave fronts in chemical media.

When waves, e. g. in excitable chemical medium, are confined to geometrical restrictions of channels and junctions one implement diodes, frequency transformers, logical gates and chemical sensors (see ► Computing in Geometrical Constrained Excitable Chemical Systems). Waves propagating in unconstrained, or free-space, chemical systems are also proved to be capable for implementation of logical circuits, and robot control and computational geometry (see ► Reaction-Diffusion Computing).

While going into domains of physics we must highlight two more types of computing devices: soliton-based computers and quantum-computers. The soliton-based devices compute by colliding self-preserved solitary waves, which change their state or trajectories in result of the collision and thus are capable of implementing basic logical gates (see ► Computing with Solitons). The quantum

computers are based on the laws of quantum mechanics, such as superposition and entanglement, interpreted in terms of logical operations (see ► Quantum Computing).

Consequently not only the laws of physics can be exploited in computation but reversely computing and computers themselves can be analyzed in terms of physical laws, e. g. computer equivalents of the first and second laws of thermodynamics, thermodynamics of digital and analog computers (see ► Thermodynamics of Computation). Fundamental microscopic physical properties of natural systems are reflected in the models of reversible computing (see ► Reversible Computing) which also forms the underlying paradigm of thermodynamically efficient computation.

The next range of unconventional computers in our – very conditional, and somewhat illusory – classification of non-standard computing devices would be those relying on biological substrates (in addition to DNA computing). They are bacterial and cellular computers (see ► Bacterial Computing, ► Cellular Computing) employing biochemistry, genetic circuitry and inter- and intra-cellular communication for transformation of information, immune-computers, which mimic behavior of immune system (see ► Immunecomputing), and computing based on comparmentalization of a computing medium with membranes (see ► Membrane Computing).

There is also a family of computers classified not by implementation substrate but some other characteristics. For instance, nano-computers are based on technology employing devices and wires with feature sizes in the order of a few nano-meters (see ► Nanocomputers). Amorphous computers are built of a collection of computational particles, with no a priori knowledge of their positions or orientations, dispersed irregularly on a surface or throughout a volume (see ► Amorphous Computing).

Evolving unconventional computers can learn, and programmed, to reconfigure their physical structure to meet certain computational demands, so far we have examples of evolving computing abilities of liquid crystals, conducting and electro-activated polymers, voltage controlled colloids (see ► Evolution in Materio).

Biological, chemical and other 'wet' substrates are indeed exciting prototypes for future computing devices. However, there is still a great potential for further enhancement and miniaturization of hardware systems, e. g. hardware analogs of reaction-diffusion systems, digital CMOS quasi-chemical chips, devices based on minority-carrier transport in semiconductors, networks of single-electron oscillators (see ► Unconventional Computing, Novel Hardware for).

Bibliography

1. Toffoli T (1998) Programmable matter methods. Future Gener Comput Syst 16:187–201
2. Thomson W (1876) On an instrument for calculating integral of the product of two given functions (Lord Kelvin). Proc R Soc 24:266–275

Unconventional Computing, Novel Hardware for

Tetsuya Asai
Hokkaido University, Sapporo, Japan

Article Outline

Glossary
Definition of the Subject
Introduction
Constructing Electrical Analog of Reaction-Diffusion Systems
Digital CMOS Reaction-Diffusion Chips
Analog CMOS Reaction-Diffusion Chip
Reaction-Diffusion Computing Devices Based on Minority-Carrier Transport in Semiconductors
Single-Electron Reaction-Diffusion System
Collision-Based RD Computers
Future Directions
Bibliography

Glossary

Analog circuit An electronic circuit that operates with currents and voltages that vary continuously with time and have no abrupt transitions between levels. Since most physical quantities, e. g., velocity and temperature, vary continuously, as does audio, an analog circuit provides the best means of representing them.

Current mirror A circuit that copies single input current to single (or multiple) output nodes. Two types of current mirrors exist; nMOS for current sinks and pMOS for current sources. Combining both types of current mirrors, one can invert a direction of currents; e. g., sink to source or source to sink.

Digital circuit An electronic circuit that can take on only a finite number of states. Binary (two-state) digital circuits are the most common. The two possible states of a binary circuit are represented by the binary digits, or bits, 0 and 1. The simplest forms of digital circuits are built from logic gates, the building blocks of the digital computer.

Diode A device that allows current flow only in one direction. Chemical diode allows for propagation of chemical waves only in one direction.

Flip-flop circuit A synchronous bistable device where the output changes state only when the clock input is triggered. That is, changes in the output occur in synchronization with the clock.

Floating-gate transistor A device consisting of a control gate, floating gate and the thin oxide layer; when floating gate is given an electrical charge, the charge is trapped in the insulating think oxide layer. The transistors are used as non-volatile storage devices because they store electrical charge for a long time without powering.

LSI, large-scale integration circuit An electronic circuit built on a semiconductor substrate, usually one of single-crystal silicon. It contains from 100 to 1000 transistors. Some LSI circuits are analog devices; an operational amplifier is an example. Other LSI circuits, such as the microprocessors used in computers, are digital devices.

Minority-carrier transport A physical phenomenon in forwardly-biased semiconductor *p*-*n* junctions. Minority carriers are generated in both area of *p*- and *n*-type semiconductors. For *p*-type semiconductors, the minority carriers are electrons, while they are holes in *n*-type semiconductors. Once minority carriers are generated, they diffuse among the semiconductor and finally disappears by the recombination of electrons and holes.

nMOS FET Abbreviation of *n*-type metal-oxide-semiconductor field effect transistor, where semiconductor is negatively charged so the transistors are controlled by movement of electrons; these transistors have three modes of operation: cut-off, triode, and saturation (active).

pMOS FET A device which works by analogy to nMOS FET but the transistors are moved on and off by movement of electron vacancies.

Single-electron circuit An electrical circuit that is functionally constructed by controlling movements of single electrons. Single-electron circuit consists of tunneling junctions and electrons are controlled by using physical phenomena called the Coulomb blockade.

Definition of the Subject

Natural systems give us examples of amorphous, unstructured devices, capable of fault-tolerant information processing, particularly with regard to the massive parallel spatial problems that digital processors have difficulty with. For example, reaction-diffusion (RD) chemical systems have the unique ability to efficiently solve combinatorial problems with natural parallelism [5]. In liquid-phase parallel RD processors (RD chemical computers), both the data and the results of the computation are encoded as concentration profiles of the reagents. The computation is performed via the spreading and interaction of the wave fronts. In experimental chemical processors, data are represented by local disturbances in the concentrations, and computation is accomplished via the interaction of waves caused by the local disturbances.

The RD chemical computers operate in parallel since the chemical medium's micro-volumes update their states simultaneously, and the molecules diffuse and react in parallel. We see a similar parallelism in cellular automata (CA). Various RD systems can be modeled in terms of CA, including the Belousov–Zhabotinsky (BZ) reaction [5,30], the Turing system [62], a precipitating BZ system for computation of Voronoi diagram [1,2], and so on. A two-dimensional CA is particularly well suited for the coming generation of massively parallel machines, in which a very large number of separate processors act in parallel. If an elemental processor in the CA is constructed from a smart processor and photosensor, various CA algorithms can easily be used to develop intelligent image sensors.

Implementing RD systems in hardware has several advantages. Hardware RD systems are very useful in simulating RD phenomena, even if the phenomena never occur in nature. This implies that a hardware system is a possible candidate for developing an artificial RD system that is superior to a natural system. For instance, hardware RD systems can operate at much faster speeds than actual RD systems. The velocity of chemical waves in a BZ reaction is $O(10^{-2})$ m/s [56], while that of a hardware RD system will be over a million times faster than that of the BZ reaction, independent of system size. This property is useful for developers of RD applications because every RD application benefits from high speed operations. These properties encouraged us to develop novel hardware for unconventional (RD-based) computing.

Introduction

This chapter presents an overview of the semiconductor implementation of reaction-diffusion (RD) computers in large-scale integrated (LSI) circuits for unconventional computing. There, we see how to model RD processes in LSI circuits and discuss several designs of RD digital chips, based on cellular-automaton models of RD and excitable systems. Feasibility of a RD digital chip is demonstrated in the construction of a Voronoi diagram and decomposition

of images. The chapter concludes with analogue RD chips, where closer to physical reality nonlinear characteristics of chemical systems are employed. We see designs of RD chips based on Oregonator, Turing and so on. Moreover, functionality of analogue RD chips in feature extraction and fingerprint reconstruction tasks are exemplified.

A RD chip consists of i) reaction circuits that emulate elementary interactions between neurons (or chemical substances) and ii) diffusion devices that imitate synapses (or chemical diffusion of the substances). RD chips were mostly designed by digital, analog, or mixed-signal complementally metal-oxide-semiconductor (CMOS) circuits of cellular neural networks (CNNs) or cellular automata (CA). Electrical cell circuits were designed to implement several CA and CNN models of RD systems [8,17,20,38], as well as fundamental RD equations [18,21,24,33,50]. Each cell is arranged on a 2D square or hexagonal grid and is connected with adjacent cells through coupling devices that transmit a cell's state to its neighboring cells, as in conventional CAs. For instance, an analog-digital hybrid RD chip [17] was designed for emulating a conventional CA model for BZ reactions [30]. A precipitating BZ system for computation of Voronoi diagram [1,2] was also implemented on an analog-digital hybrid RD chip [20]. A full-digital RD processor [38] was also designed on the basis of a multiple-valued CA model, called *excitable lattices* [5]. Furthermore, a RD CA processor for complex image processing has been proposed [19]. It performs quadrilateral-object extraction based on serial and parallel CA algorithms. An analog cell circuit was also designed to be equivalent to spatial-discrete Turing RD systems [24]. A full-analog RD chip that emulates BZ reactions has also been designed and fabricated [21]. Furthermore, blueprints of non-CMOS RD chips have been designed; i. e., a RD device based on minority-carrier transport in semiconductor devices [18]. In the following sections, we see how to construct an artificial RD system on *solid-state media*, and to develop some applications using the solid-state RD system that could cope with conventional digital computers.

Constructing Electrical Analog of Reaction-Diffusion Systems

The behavior of RD systems, or the spatiotemporal patterns of chemical concentration, can be expressed by the reaction-diffusion equation, a partial differential equation with chemical concentrations as variables:

$$\frac{\partial \mathbf{u}}{\partial t} = \mathbf{f}(\mathbf{u}) + D\Delta\mathbf{u}\,, \quad [\mathbf{u} = (u_1, u_2, u_3, \ldots)]\,, \qquad (1)$$

where t is time, $\mathbf{u}$ is the vector of chemical concentrations,

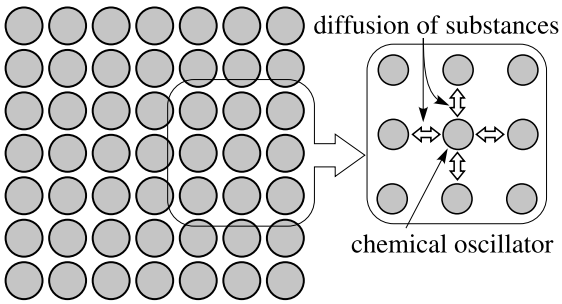

Unconventional Computing, Novel Hardware for, Figure 1
Simplified model of RD systems, consisting of many chemical oscillators. Each oscillator has variables corresponding to chemical concentrations $u_1, u_2, u_3, \ldots$ in Eq. (1) and interacts with its neighbors through diffusion of substances

u_i is the concentration of the ith substance, and D is the diagonal matrix of diffusion coefficients. Nonlinear function $\mathbf{f}(\mathbf{u})$ is the reaction term that represents the reaction kinetics of the system. Spatial derivative $D\Delta\mathbf{u}$ is the diffusion term that represents the change of $\mathbf{u}$ due to the diffusion of the substance. A greater number of variables results in more complex dynamics and a more complicated dissipative structure. A simple reaction-diffusion system with few variables, however, will still exhibit dynamics similar to biological activity.

An RD system can be considered an aggregate of coupled chemical oscillators, or a chemical cellular automaton, as described in Fig. 1. Each oscillator represents the local reaction of chemical substances and generates nonlinear dynamics $\mathrm{d}\mathbf{u}/\mathrm{d}t = \mathbf{f}(\mathbf{u})$ that corresponds to reaction kinetics in Eq. (1). The oscillator interacts with its neighbors through nonlocal diffusion of substances; this corresponds to the diffusion term in Eq. (1) and produces dynamics $\mathrm{d}\mathbf{u}/\mathrm{d}t = D\Delta\mathbf{u}$. Because of diffusion, all oscillators correlate with one another to generate synchronization and entrainment. Consequently, the system as a whole produces orderly dissipative structures on a macroscopic level. The size of each oscillator, or the size of the local space in which chemical concentrations are roughly uniform, depends on the diffusion coefficients and reaction velocities in the system. It is several micrometers in diameter in many liquid RD systems; therefore, even a tiny RD system in a test tube contains millions of oscillators.

An electrical analog of RD systems can be created by using electrical oscillation circuits instead of chemical oscillators and coupling these circuits with one another in a way that imitates diffusion. Variables are the electrical potential of nodes in the oscillation circuits in this electrical RD system. The system will produce electrical dissipative structures, i. e., orderly spatiotemporal patterns of node potentials, under appropriate conditions.

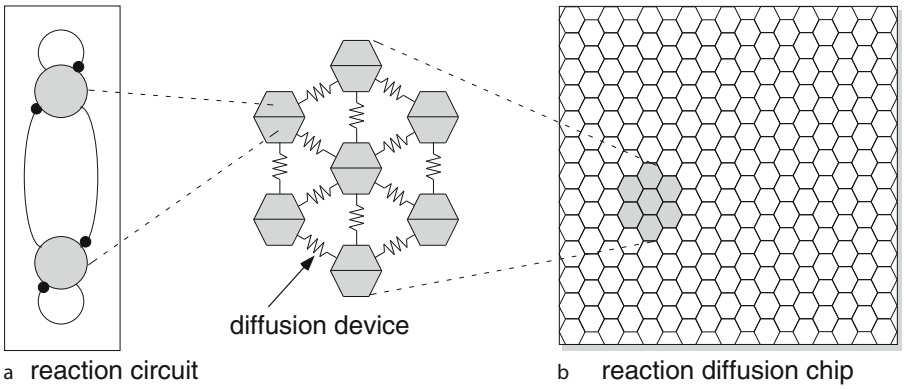

Unconventional Computing, Novel Hardware for, Figure 2
Basic construction of RD chip

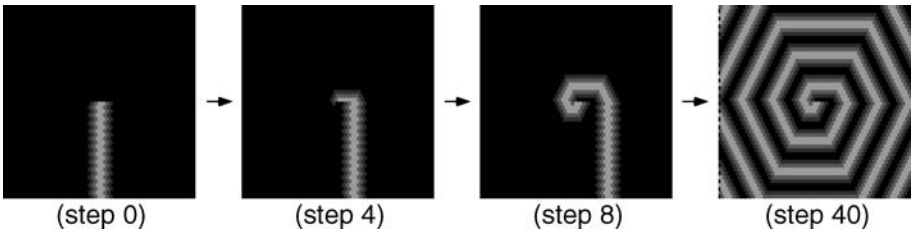

Unconventional Computing, Novel Hardware for, Figure 3
Excitatory modelock operations of RD circuit [17]

The key to building an electrical RD system is to integrate a large number of oscillation circuits on a chip with coupling subcircuits. A large arrangement of oscillators (e. g., 1000 × 1000 or more) is needed to generate complex, varied dissipative structures as observed in chemical RD systems. Oscillators constructed by micro- or nanoscale circuits are thus useful to achieve such large scale integration. Such circuits can generate nonlinear oscillation through a simple circuit structure, so it can effectively be used in producing small oscillators for electrical RD systems.

Digital CMOS Reaction-Diffusion Chips

A Reaction-Diffusion Circuit Based on Cellular-Automaton Processing Emulating the Belousov–Zhabotinsky Reaction

The Belousov–Zhabotinsky (BZ) reaction provides us important clues to control 2D phase-lagged stable synchronous patterns in excitable medium. Because of the difficulty in computing RD systems in large systems using conventional digital processors a cellular-automaton (CA) circuit that emulates the BZ reaction was proposed [17]. In the circuit, a two-dimensional array of parallel processing cells, shown in Fig. 2, is responsible for the emulation, and its operation rate is independent of the system size. The operations of the CA circuit were demonstrated by using a simulation program with integrated circuit emphasis (SPICE). In the circuit's initial state, cells adjacent to inactive cells were in a refractory period (step 0 in Fig. 3). The inactive cells adjacent to the white bar in Fig. 3 were suppressed by adjacent cells in the refractory period (cells in the white bar). The inactive cells then entered an active, inactive, or refractory period, depending on the degree of the refractory condition. When the inactive cells were in an active or inactive period, the tip of the bar rotated inward (step 4 to 8 in Fig. 3), resulting in the generation of the modelock (spiral patterns) typically observed in the BZ reaction (step 40 in Fig. 3). A hexagonal distortion of the propagating waves was generated by interactions between adjacent cells. These results indicated that the RD chip could be easily integrated into existing digital systems and can be used to clarify RD systems, aiming at developing further novel applications.

Reaction-Diffusion Chip Implementing Excitable Lattices with Multiple-Valued Cellular Automata

A RD chip was fabricated based on a multiple-valued CA model of excitable lattices [38]. The experiments

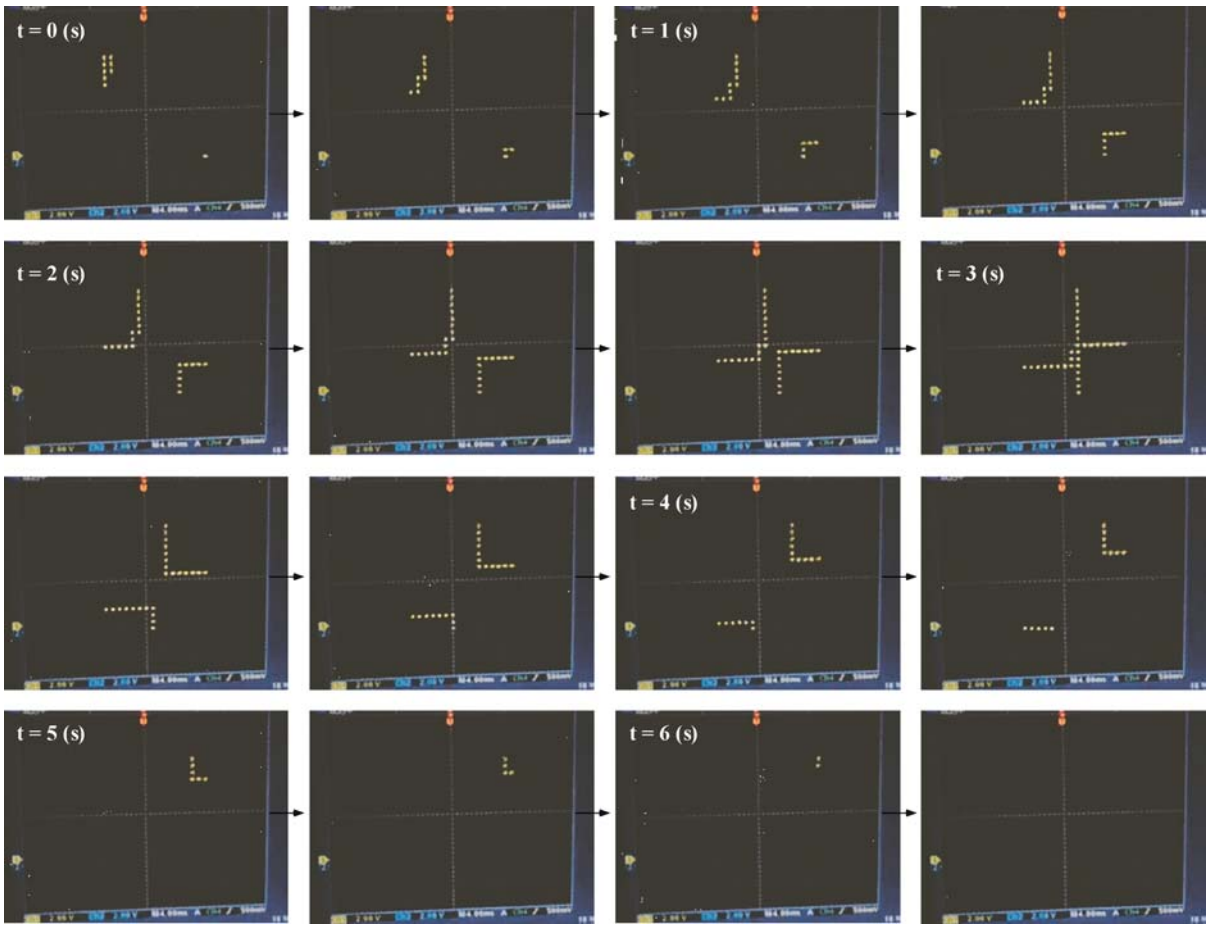

Unconventional Computing, Novel Hardware for, Figure 4
Snapshots of recorded movie obtained from fabricated RD chip [38]

confirmed the expected operations, i. e., excitable wave propagation and annihilation. One could obtain a binary stream from the common output wire by selecting each cell sequentially. Using a conventional displaying technique, the binary stream was reconstructed on a 2-D display. Figure 4 shows snapshots taken from the recorded movie. Each dot represents an excitatory cell where EXC is logical "1". In the experiment, the supply voltage were set at 5 V, and the system clock was set at low frequency (2.5 Hz) so that "very-slow" spatiotemporal activities could be observed visually (the low frequency was used only for the visualization, and was not the upper limit of the circuit operation). Pin-spot lights were applied to several cells at top-left and bottom right corners of the chip. The circuit exhibited the expected results; i. e., two excitable waves of excited cells triggered by the corner cells propagated toward the center and disappeared when they collided. This result suggests that if we use a more microscopic process and a large number of cells were implemented, we would observe the same complex (BZ-like) patterns, as observed in the original excitable lattices [5].

This chip can operate much faster than real chemical RD systems, even when the system clock frequency is $O(1)$ Hz, and is much easier to use in various experimental environments. Therefore, the chip should encourage RD application developers who use such properties of excitable waves to develop unconventional computing schemes, e. g., chemical image processing, pattern recognition, path planing, and robot navigation.

Silicon Implementation of a Chemical Reaction-Diffusion Processor for Computation of Voronoi Diagram

RD chemical systems are known to realize sensible computation when both data and results of the computation

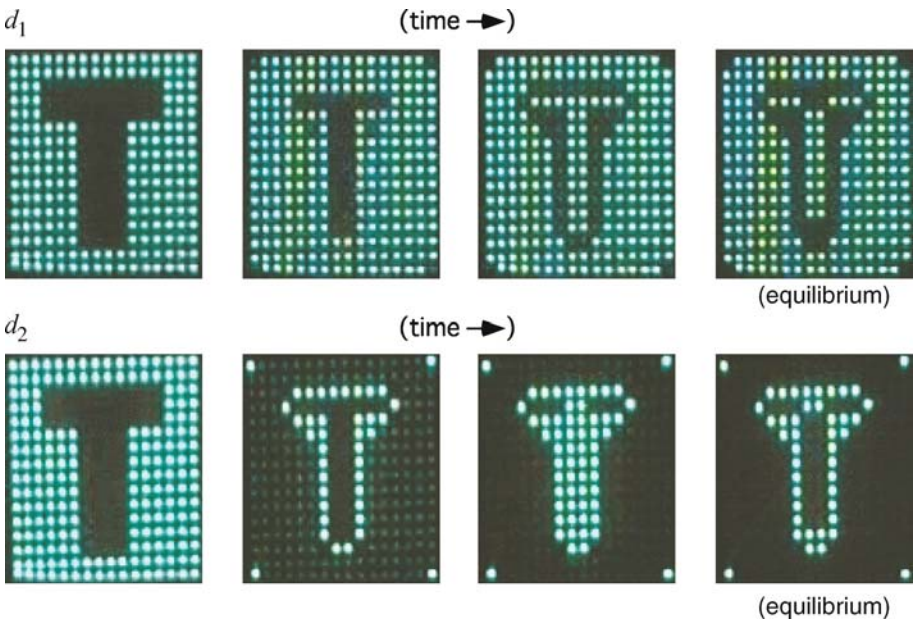

Unconventional Computing, Novel Hardware for, Figure 5
Skeleton operation with "T" shape [20]

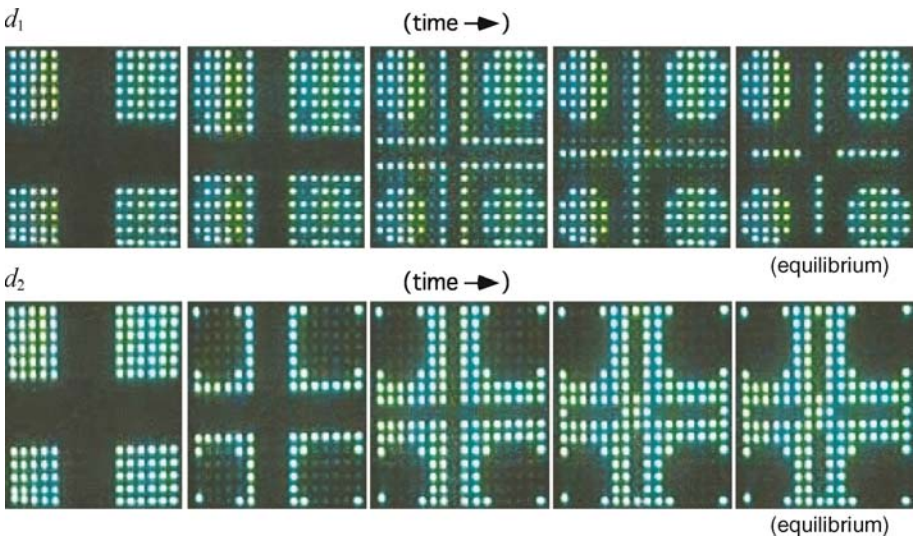

Unconventional Computing, Novel Hardware for, Figure 6
Skeleton operation with "+" shape [20]

are encoded in concentration profiles of chemical species; the computation is implemented via spreading and interaction of either diffusive or phase waves, while a silicon RD chip is an electronic analog of the chemical RD systems.

A prototype RD chip implementing a chemical RD processor for a well-known NP-complete problem of computational geometry – computation of a Voronoi diagram was fabricated. Here we see experimental results for fabricated RD chips and compare the accuracy of information processing in silicon analogs of RD processors and their experimental 'wetware' prototypes [20]. Figures 5 and 6 show examples of skeleton operation of a T and '+' shaped images. As initial images, a glass mask was prepared where 'T' and '+' areas were exactly masked. Therefore, cells under the 'T' and '+' areas are initially resting and the rest are initially excited. At its equilibrium, skeletons of 'T' and '+' were successfully obtained.

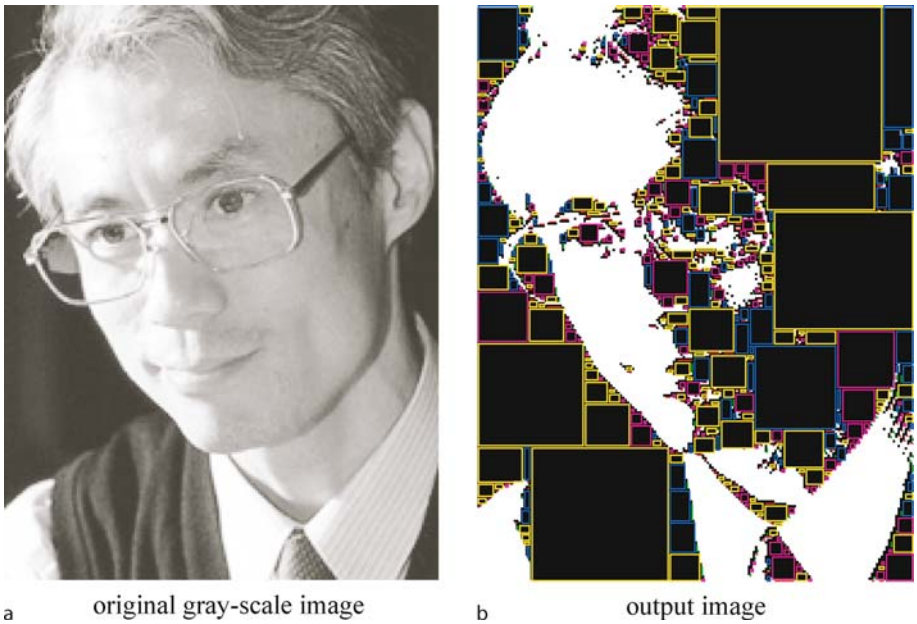

Unconventional Computing, Novel Hardware for, Figure 7
Simulation results for 181 × 238 image; a original image, b mixed image of quantized image given to CA LSI and detected quadrilateral objects [19]

A Quadrilateral-Object Composer for Binary Images with Reaction-Diffusion Cellular Automata

A CA LSI architecture that extracted quadrilateral objects from binary images was proposed in [19] with a serial combination of parallel CA algorithms, based on RD chemical systems model. Each cell in the CA was implemented by a simple digital circuit called an elemental processor. The CA LSI can be constructed by a large number of elemental processors and their controllers operating in serial and parallel.

Figure 7a demonstrates object extraction for a natural image. The image was quantized, and given to the CA LSI. Figure 7b show the results. The maximum boxes were correctly detected in order, as predicted. The input bitmap image that consisted of 181 × 238 pixels was decomposed of 1020 quadrilateral objects. The bitmap image occupied 43,078 bits (5385 bytes) on memory, while the objects used 4080 bytes (8-bit address of 4 corners × 1020 boxes). The important thing is not discussing the compression rate between bitmap images and extracted objects, but that bitmap images were represented by small number of vector objects, which facilitates picture drawing in terms of the drawing speed if we have variable box window.

One of the most important application targets for the proposed chip is a computer-aided design (CAD) system for LSIs. Conventional LSI CAD tools use polygons to represent device structures. However, recent LSIs include not only polygon patterns but also graphical patterns, consisting of large number of dots, usually imported from image files such as JPEGs, to implement complex analog structures. In the mask manufacturing process, exposing a large number of dot patterns is quite a time-consuming task. Recently, electron beam (EB) lithography systems that can expose wide areas through a quadrilateral window have been produced on a commercial basis. The proposed LSI can produce efficient stream files from binary image files that can easily be handled by the new EB systems, by developing simple software that converts the box format, produced by the proposed LSI, to a conventional stream format.

Analog CMOS Reaction-Diffusion Chip

Analog Reaction-Diffusion Chip with Hardware Oregonator Model

Silicon devices that imitate the autocatalytic and dissipative phenomena of RD systems were developed [21]. Numerical simulations and experimental results revealed that an RD device could successfully produce concentric and spiral waves in the same way as natural RD systems. These results encouraged us to develop new applications based on natural RD phenomena using hardware RD devices.

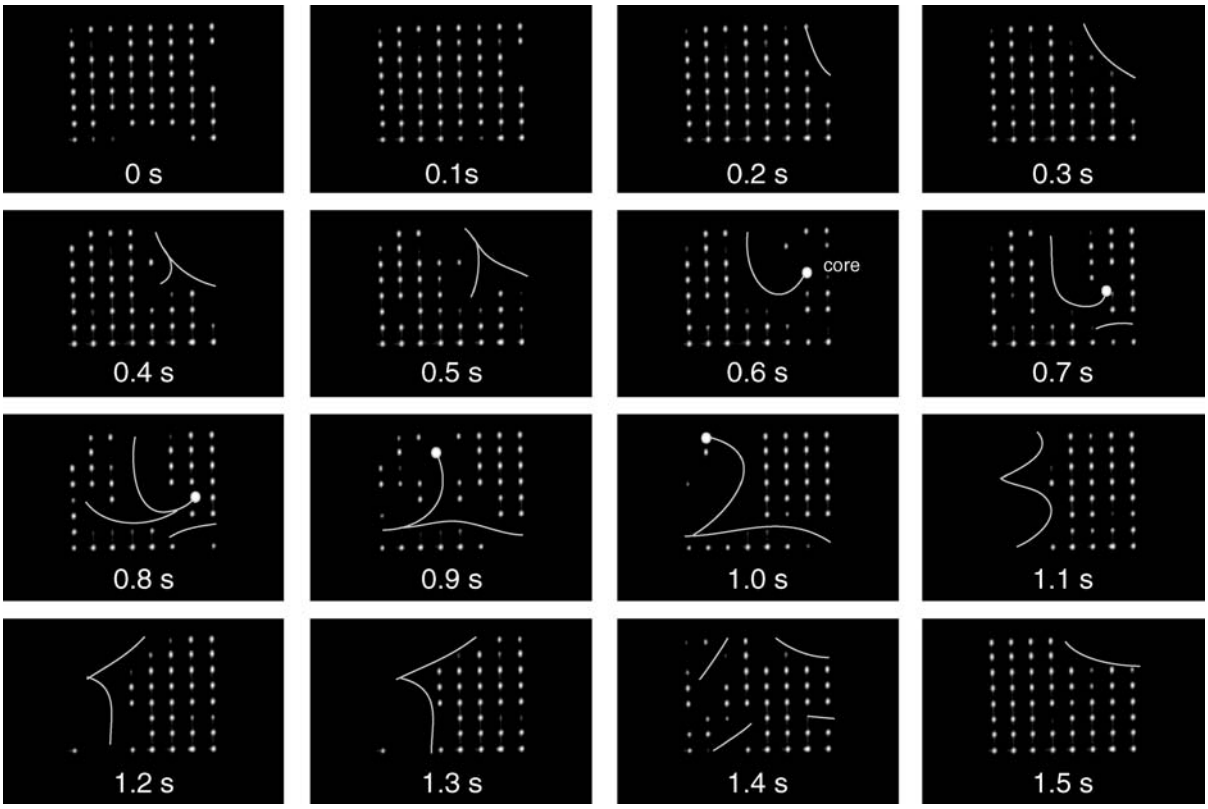

Unconventional Computing, Novel Hardware for, Figure 8
Spiral patterns on RD chip (weak connections between cells) [21]

Figure 8 presents an example where some spiral (modelock) patterns of cell clusters were observed. Snapshots were taken with at intervals of 100 ms. The active-cell clusters and cores of the spirals are superimposed with the figure by white curves and white circles, respectively. Although observing "beautiful" spirals as in chemical RD systems is difficult because of the small number of cells, the appearance and disappearance of small sections of spiral waves were successfully observed.

RD devices and circuits are useful not only for hardware RD systems but also for constructing modern neurochips. The excitatory and oscillatory behaviors of an RD device and circuit are very similar to actual neurons that produce sequences of identically shaped pulses in time, called *spikes*. Recently, Fukai demonstrated that an inhibitory network of spiking neurons achieves robust and efficient neural competition on the basis of a novel timing mechanism of neural activity [28]. A network with such a timing mechanism may provide an appropriate platform to develop analog LSI circuits and could overcome problems with analog devices, namely their lack of precision and reproducibility.

Striped and Spotted Pattern Generation on RD Cellular Automata

A novel RD model that is suitable for LSI implementation and its basic LSI architecture were proposed in [55]. The model employs linear diffusion fields of activators and inhibitors and a discrete transition rule after diffusion. Image-processing LSI circuits based on pattern formation in RD systems were developed. Continuous diffusion fields and an analog state variable were introduced to improve the Young's local activator-inhibitor model [62]. A model pattern diagram was produced on a 2D parameter space through extensive numerical simulations. The spatial frequency and form (striped or spotted) could be controlled with only two parameters. Theoretical analysis of the one dimensional model proved that i) spatial distribution given by a periodic square function is stable at the equilibrium and ii) the spatial frequency is inversely proportional to the square root of a diffusion coefficient of the inhibitors.

A basic circuit for the proposed model was designed, i. e., an RD LSI based on the analog computing method

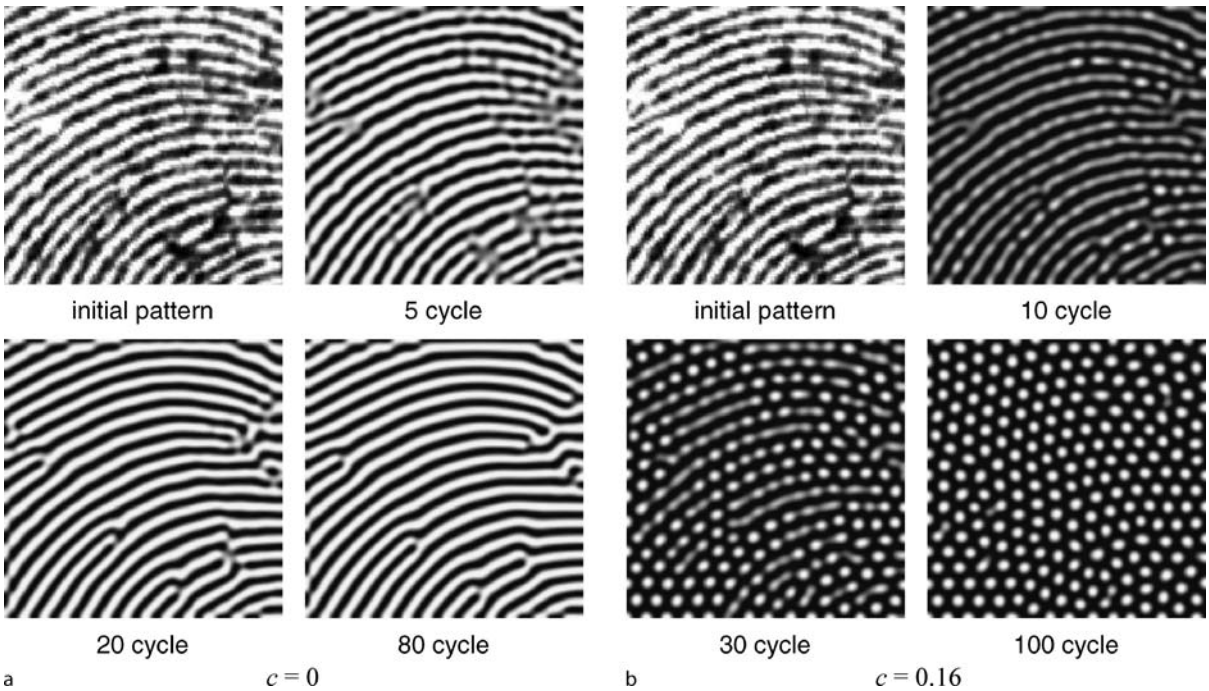

Unconventional Computing, Novel Hardware for, Figure 9
Snapshots of pattern formation from initial fingerprint image [55]

where the concentration of chemicals was represented by a two-dimensional voltage distribution and the cell voltage was diffused step by step. By mimicking two diffusion fields with the proposed model in one diffusion circuit on the LSI, one can reduce the area of the unit cell circuit.

Figure 9a has snapshots of pattern formation in the circuit. One can estimate that the system produces striped patterns from the theory [55]. Therefore, a fingerprint pattern was used as an initial input. Noisy local patterns were repaired by their surrounding striped patterns, as time increased. The circuit required 50 cycles (8000 clocks) to reach equilibrium. Figure 9b shows the results for spot pattern generation. The same initial input as in Fig. 9a was given to the circuit. As expected from the theory, spotted patterns were obtained. The pattern formation process was the same as in Fig. 9a where noisy local spots were restored by surrounding global spotted patterns. Therefore, this circuit would be suitable for restoring regularly-arranged spotted patterns such as polka-dot patterns. The system took 100 cycles (16,000 clocks) until it reached equilibrium to restore the spotted patterns.

Reaction-Diffusion Computing Devices Based on Minority-Carrier Transport in Semiconductors

A massive parallel computing device was designed [18] based on principles of information processing in RD chemical media [4,5] (Figs. 10 and 11). This device imitates auto-catalytic and dissipative phenomena of the chemical RD systems, however comparing to real chemical medium the semi-conductor analog of RD computers, functions much faster. Operational characteristics of the RD silicon devices and feasibility of the approach on several computational tasks are shown in [18]. The results indicate that the proposed RD device will be a useful tool for developing novel hardware architectures based on RD principles of information processing.

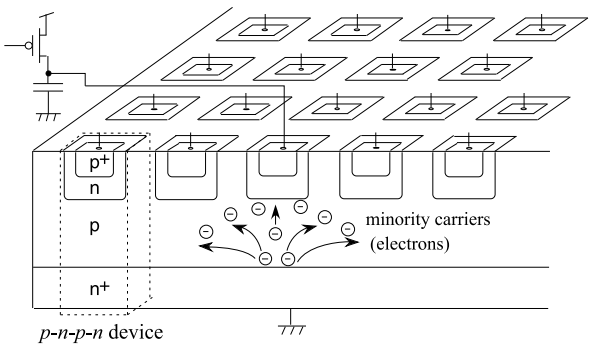

Unconventional Computing, Novel Hardware for, Figure 10
Construction of two-dimensional RD device with vertical *p-n-p-n* device [18]

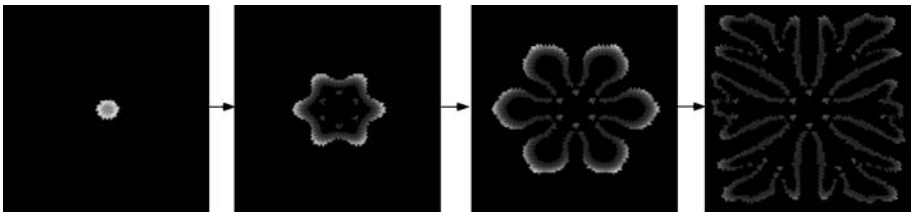

Unconventional Computing, Novel Hardware for, Figure 11
Simulation results of RD device producing multiplicating patterns [18]

Practical value of RD chemical systems are significantly reduced by low speed of traveling waves which makes real-time computation senseless. One of the cost-efficient options to overcome the speed-limitations of RD computers while preserving unique features of wave-based computing is to implement RD chemical computers in silicon. The velocity of traveling wavefronts in typical reaction diffusion systems, e. g., BZ reaction, is 10^{-2} m/s [56], while that of a hardware RD system will be over a million times faster than that of the BZ reaction, independent of system size [7]. The increase in speed will be indispensable for developers of RD computers. Moreover, if a RD system is implemented in integrated circuits, then we would be able to artificially design various types RD spatio-temporal dynamics and thus develop parallel computing processors for novel applications. Basing on experimental evidences of RD-like behavior, namely traveling current density filaments [41], in *p-n-p-n* devices a novel type of semiconductor RD computing device, where minority carriers diffuse as chemical species and reaction elements are represented by *p-n-p-n* diodes, was proposed.

Single-Electron Reaction-Diffusion System

This section introduces a single-electron device that is analogous to the RD system. This electrical RD device consists of a two-dimensional array of single-electron nonlinear oscillators that are combined with one another through diffusive coupling. The device produces animated spatiotemporal patterns of node voltages, e. g., a rotating spiral pattern similar to that of a colony of cellular slime molds and a dividing-and-multiplying pattern that reminds us of cell division. A method of fabricating actual devices by using self-organized crystal growth technology is also described. The following is an excerpt from [43]. For details, see the reference.

Figure 12 shows an electrical oscillator constructed by a single-electron circuit. It consists of tunneling junction C_j and high resistance R connected in series at node 1 and biased by positive voltage V_{dd}. This circuit is an elementary component of single-electron circuits known as the single-electron transistor (SET) cell (see [31] for detailed explanation). A SET cell only has a single variable, voltage V_1 of node 1, but it can be oscillatory or excitatory in operation – which is indispensable in creating RD systems – because the node voltage can produce a discontinuous change because of electron tunneling. In continuous-variable systems such as chemical reaction systems, two or more variables are needed for oscillatory and excitatory operations.

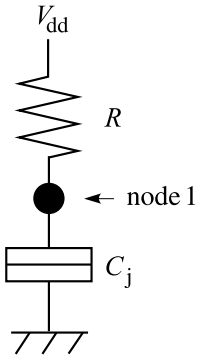

Unconventional Computing, Novel Hardware for, Figure 12
Single-electron oscillator (a SET cell) consisting of tunneling junction C_j, high resistance R connected at node 1, and positive bias voltage V_{dd}

The SET cell operates as a nonlinear oscillator at the low temperatures at which the Coulomb-blockade effect occurs. It is oscillatory (astable) if $V_{dd} > e/(2C_j)$ (e is elementary charge) and produces nonlinear oscillation in voltage at node 1 (Fig. 13a). The node voltage gradually increases as junction capacitance C_j is charged through resistance R, then drops discontinuously because of electron tunneling through the junction, again gradually increasing to repeat the same cycles. In contrast, the oscillator is excitatory (monostable) if $V_{dd} < e/(2C_j)$ and produces single-pulse operation excited by an external trigger (Fig. 13b). A modified Monte Carlo method is used for the simulation. Kuwamura and his colleagues [35] have given details

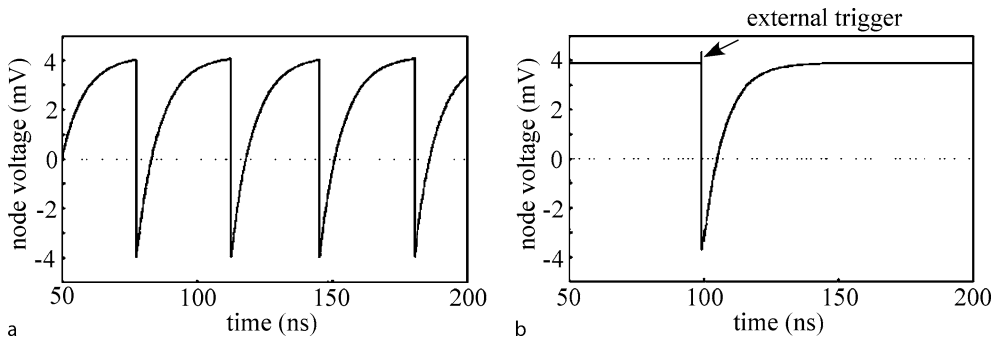

Unconventional Computing, Novel Hardware for, Figure 13
Operation of the oscillator. Waveforms of node voltage are shown for a self-induced oscillation and b monostable oscillation, simulated with following set of parameters: tunneling junction capacitance $C_j = 20$ aF, tunneling junction conductance = 1 μS, high resistance R = 400 MΩ, and zero temperature. Bias voltage $V_{dd} = 4.2$ mV for self-induced oscillation, and $V_{dd} = 3.8$ mV for monostable oscillation

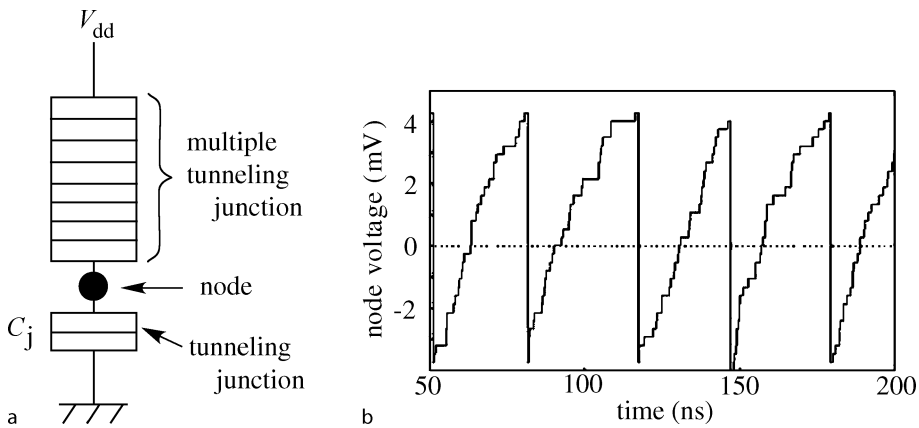

Unconventional Computing, Novel Hardware for, Figure 14
Single-electron oscillator with a multiple tunneling junction: a circuit configuration, and b simulated self-induced oscillation. Parameters are: capacitance of single tunneling junction $C_j = 10$ aF, conductance of the single tunneling junction = 1 μS, 30 tunnelling junctions in the multiple tunneling junction, capacitance and conductance of a tunneling junction in the multiple tunneling junction are 300 aF and 50 nS, bias voltage $V_{dd} = 8.6$ mV, and zero temperature

of this method. Also see Appendix in [59]. For constructing electrical RD systems, oscillatory oscillators and excitatory ones, or both, can be used.

The oscillator exhibits discontinuous, probabilistic kinetics resulting from electron tunneling. The kinetics is given in the form of

$$\frac{dV_1}{dt} = \frac{V_{dd} - V_1}{RC_j} - \frac{e}{C_j}\delta\left(V_1 - \frac{e}{2C_j} - \Delta V\right),$$

where $\delta(\cdot)$ represents a discontinuous change in node voltage caused by electron tunneling. Probabilistic operation arises from the stochastic nature of tunneling; i. e., a time lag (a waiting time) exists between when junction voltage exceeds tunneling threshold $e/(2C_j)$ and when tunneling actually occurs. This effect is represented by delay term ΔV in the equation. Because the value of ΔV has probabilistic fluctuations in every tunneling event and cannot be expressed in analytical form, so Monte Carlo simulation is necessary for studying the behavior of the oscillator.

In fabricating actual oscillators, a high resistance of hundreds of mega-ohms or more is not easy to implement on an LSI chip. A better way is to use a multiple tunneling junction, i. e., a series of many tunneling junctions, instead of high resistance (Fig. 14a). This structure also enables oscillatory and excitatory operations to be obtained because sequential electron tunneling through a multiple tunneling junction has a similar effect to current flowing at high

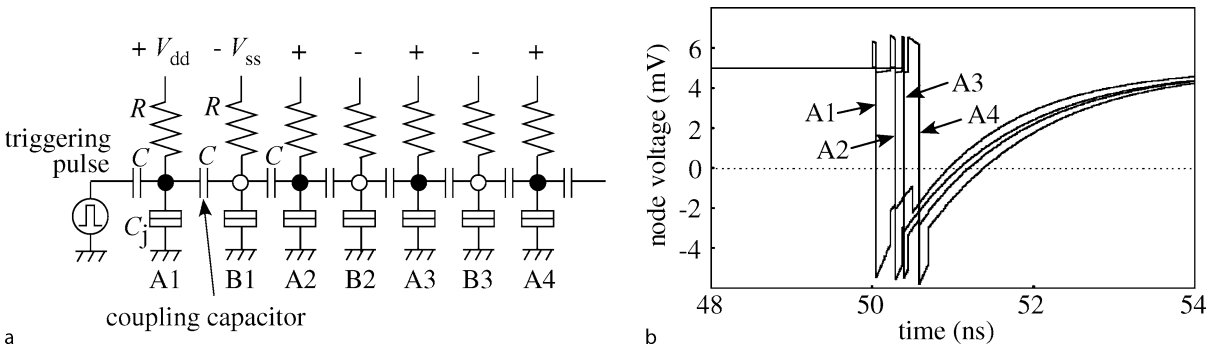

Unconventional Computing, Novel Hardware for, Figure 15

Diffusive connection of oscillators. a One-dimensional chain of oscillators (A1, A2, ...) with intermediary cells (B1, B2, ...) and coupling capacitors *C*. For study of the transmission of tunneling, a triggering pulse generator is connected to the left end. b Transmission of tunneling through the chain of excitatory oscillators. The waveform of node voltage is plotted for each oscillator. A triggering pulse was applied to the leftmost oscillator, and tunneling started at the oscillator to transmit along the chain with delay. Jumps in curves A1–A4 result from electron tunneling in oscillators A1–A4. Simulated with a set of parameters: $C_j = 10$ aF, $C = 2$ aF, $R = 77$ MΩ, tunneling junction conductance = 5 μS, $V_{dd} = 5$ mV, $-V_{ss} = -5$ mV, and zero temperature

resistance (Fig. 14b). In the following sections, however, the high-resistance SET cell (Fig. 12) is used to construct electrical RD systems because less computing time is required in simulating RD operation. One can expect that the knowledge obtained from high-resistance RD systems will be able to be applied to RD systems consisting of multiple-junction oscillators.

To construct RD systems, oscillators have to be connected with one another so that they will interact through "diffusive" coupling to generate synchronization and entrainment. To do this, the oscillators are connected by means of intermediary oscillation cells and coupling capacitors. Figure 15a illustrates the method of connection with a one-dimensional chain of oscillators. The oscillators (SET cells denoted by A1, A2, ..., with their nodes represented by closed circles) are connected with their neighboring oscillators through intermediary oscillation cells (SET cells denoted by B1, B2, ..., with their nodes represented by open circles) and coupling capacitors *C*. One can use an excitatory SET cell biased with a negative voltage $-V_{ss}$ as the intermediary oscillation cell. An excitatory SET cell biased with a negative voltage $-V_{ss}$ is used here as the intermediary oscillation cell.

When electron tunneling occurs in an oscillator in this structure, the node voltage of the oscillator changes from positive to negative, and this induces, through coupling capacitor *C*, electron tunneling in an adjacent intermediary cell. The induced tunneling changes the node voltage of the intermediary cell from negative to positive, and this induces electron tunneling in an adjacent oscillator. In this way, electron tunneling is transmitted from one oscillator to another along the oscillator chain. There is a time lag between two tunneling events in two neighboring oscillators as if these oscillators interacted through diffusion. This phenomenon is not diffusion itself and cannot be expressed in the form $D\Delta\mathbf{u}$ in Eq. (1) but can be used as a substitute for diffusion.

The transmission of tunneling with delay is illustrated in Fig. 15b with simulated results for a chain of excitatory oscillators with intermediary cells. Electron tunneling was induced in the leftmost oscillator by a triggering pulse, and it was transmitted to the right along the chain with delay. In other words, an excitation wave of tunneling traveled to the right along the chain. Its delay in traveling from one oscillator to a neighbor has probabilistic fluctuations because of the stochastic nature of tunneling, but this is not a problem for applications to RD systems.

An electrical RD system can be constructed by connecting oscillators into a network by means of intermediary cells and coupling capacitors (Fig. 16). Each oscillator is connected to its neighboring 4 oscillators by means of 4 intermediary cells and coupling capacitors. This is a two-dimensional RD system. A three-dimensional RD system can also be constructed in a similar way by arranging oscillators into a cubic structure and connecting each oscillator with its 6 neighboring oscillators by means of 6 intermediary cells and coupling capacitors.

In the single-electron RD system, the node voltage of each oscillator changes temporally as the oscillators operate through mutual interactions. Consequently, a two-dimensional spatiotemporal pattern of the node voltages is produced on the RD system. Since this voltage pattern corresponds to the dissipative structure in chemical RD systems, it can be called an "electrical dissipative structure".

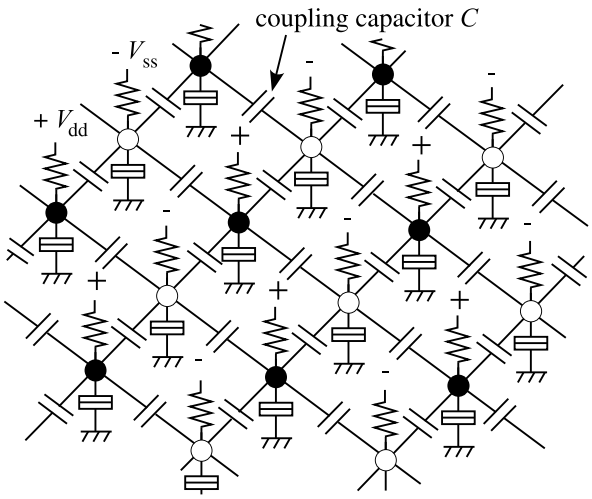

Unconventional Computing, Novel Hardware for, Figure 16
Two-dimensional RD system consisting of the network of single-electron oscillators. Each oscillator (closed-circle node) is connected with 4 neighboring oscillators by means of 4 intermediary cells (open-circle nodes) and coupling capacitors

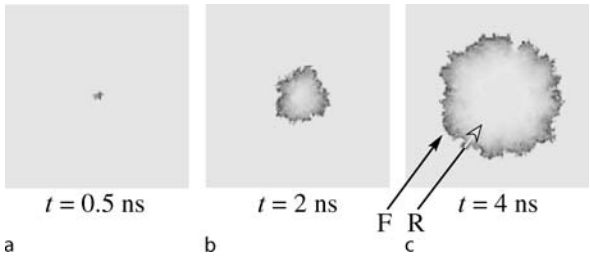

Unconventional Computing, Novel Hardware for, Figure 17
Expanding circular pattern in the single-electron RD system. Snapshots for three time steps. Simulated with parameters: tunneling junction capacitance $C_j = 1$ aF, tunneling junction conductance = 1 μS, high resistance $R = 137.5$ MΩ, coupling capacitance $C = 1$ aF, bias voltage $V_{dd} = 16.5$ mV, $-V_{ss} = -16.5$ mV, and zero temperature

A variety of electrical dissipative structures are produced from different sets of system parameters. To understand the behavior of an electrical RD system entirely, a phase diagram for the system must be drawn, i. e., a diagram that depicts – in the multidimensional space of system parameters – what kind of dissipative structure will appear for each set of parameter values. However, a phase diagram for the RD system cannot be drawn without a long numerical computer simulation because its reaction-diffusion kinetics cannot be expressed in analytical form. Instead, few examples of electrical dissipative structures simulated with a few sample sets of parameter values are demonstrated.

Although a single-electron RD system differs greatly from chemical RD systems in terms of reaction-diffusion kinetics, it can produce dissipative structures similar to those of chemical RD systems. Here, three examples are exhibited, i. e., an expanding circular pattern, a rotating spiral pattern, and a dividing-and-multiplying pattern. The following will have the results simulated for a RD system consisting of 201 × 201 excitatory oscillators and 200 × 200 intermediary cells.

Expanding Circular Pattern

A single-electron RD system consisting of excitatory oscillators is in a stable uniform state as it stands. Once a triggering signal is applied to an oscillator in the system, an excitation wave of tunneling starts at the oscillator and propagates in all directions to form an expanding circular pattern. This can be seen in Fig. 17; the node voltage of each oscillator is represented by a gray scale: the light shading means high voltage, and the dark means low voltage. The front F of the wave is the region where tunneling just occurred and, therefore, the node voltage of the oscillators is at the lowest negative value. The front line is uneven or irregular because the velocity of the traveling wave fluctuated in each direction throughout the process because of the stochastic waiting time of tunneling.

After the excitation wave passed through, the node voltage of each oscillator gradually increased to return to its initial value, the positive bias voltage. This is indicated in the figure by the light shading on the rear R of the wave. If a triggering signal is applied repeatedly to one oscillator, a concentric circular wave – called a target pattern in chemical RD systems – will be generated.

Rotating Spiral Pattern

This pattern appears when an expanding circular wave is chipped by external disturbance, thereby making an endpoint to appear in the wave front. With this endpoint acting as a center, the wave begins to curl itself to form a rotating spiral pattern (Fig. 18). The principle of curling is similar to that in chemical RD systems.

In this example, a triggering signal was applied to the middle oscillator on the left of the RD system. When an excitation wave started and expanded a little, the lower half of the wave was chipped by resetting the node voltage of oscillators to zero (Fig. 18a). After that, the RD system was left to operate freely, and a rotating spiral pattern of node voltages automatically generated as can be seen in Figs. 18b–f.

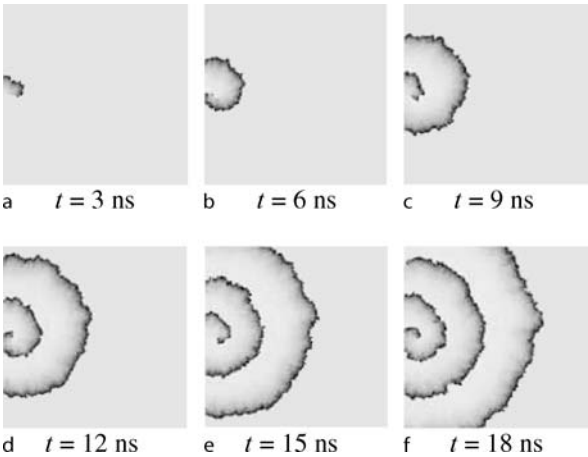

Unconventional Computing, Novel Hardware for, Figure 18
Rotating spiral pattern. Snapshots for six time steps. Simulated with the same parameters as used for Fig. 17

Dividing-and-Multiplying Pattern

This pattern appears when the coupling between oscillators is weak (i. e., small coupling capacitance or low bias voltage). When this happens, electron tunneling in an oscillator cannot be transmitted to all four adjacent intermediary cells; e. g., tunneling can be transmitted to the right and left cells but not to the upper and lower cells. As a result, an expanding node-voltage pattern splits into pieces, and each piece again expands to split again. This produces dividing-and-multiplying patterns (Fig. 19). The principle of division is different from that in chemical RD systems,

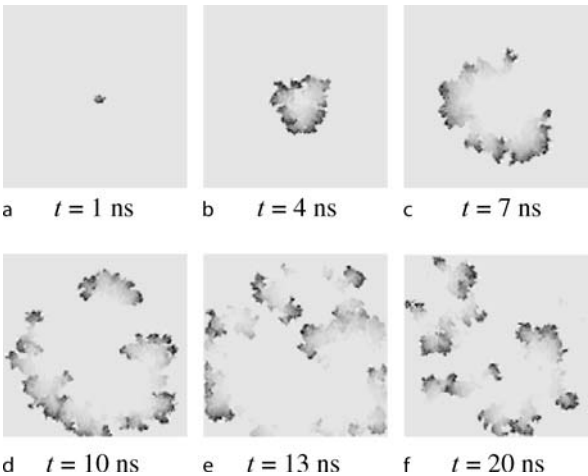

Unconventional Computing, Novel Hardware for, Figure 19
Dividing-and-multiplying pattern. Snapshots for six time steps. Simulated with the same parameters as used for Fig. 17 except that $R = 150.5\,\mathrm{M\Omega}$, $V_{dd} = 15.8\,\mathrm{mV}$, and $-V_{ss} = -15.8\,\mathrm{mV}$

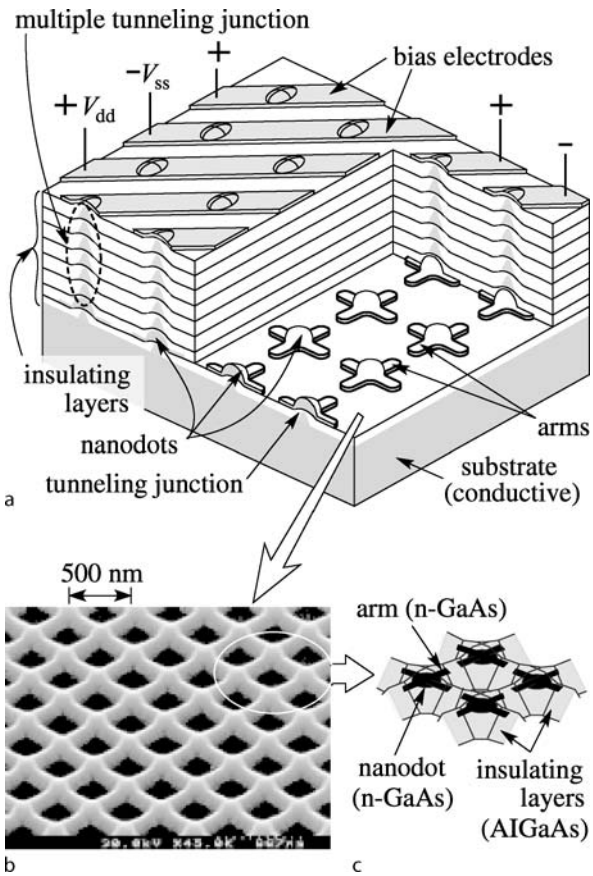

Unconventional Computing, Novel Hardware for, Figure 20
Device structure for the single-electron RD system. a Three-dimensional and cross-sectional schematics; b SEM photograph of a two-dimensional array of GaAs nanodots with coupling arms and tunneling junctions; c schematic diagram of the nanodots with coupling arms

but the behavior of created patterns is somewhat similar. In a way, we may consider that there are electrical microbes consisting of negative voltages living on the RD system, eating positive charges on nodes as food, and propagating so that they can will spread all over the system.

The unit element in this RD system is a single-electron oscillator coupled with four neighbors. The multiple-tunneling-junction oscillator (Fig. 14) is preferable for this element because it can be made without high resistance, which is difficult to implement on an LSI chip. Arranging such oscillators into a two-dimensional array produces an RD system, so the next task is to fabricate many identical oscillators on a substrate. Figure 20a shows the three-dimensional and cross-sectional schematics for the structure of the device. Each oscillator consists of a conductive nanodot (minute dot) with four coupling arms, and there is

a tunneling junction between the nanodot and the conductive substrate beneath it. Many series-connected junctions run between the nanodot and a positive-bias or a negative-bias electrode. Capacitive coupling between neighboring oscillators can be achieved by laying their coupling arms close to each other.

The key in this construction is to prepare a large arrangement of nanodots with coupling arms and tunneling junctions. A process technology that could be used to fabricate the RD-system structure was previously proposed and demonstrated [42]. This technology uses self-organized crystal growth achieved by selective-area metalorganic vapor-phase epitaxy (SA-MOVPE), and it can be used to fabricate GaAs nanodots with arms and tunneling junctions on a GaAs substrate by making use of the dependence of the crystal-growth rate on crystal orientation (for detailed explanation, see [36] and [37]). With this technology, a nanodot with four coupling arms can be formed automatically in a self-organizing manner. This technology can also be used to automatically create the structure for multiple tunneling junctions on nanodots simply by repeating the growth of an *n*-type GaAs layer and an insulating AlGaAs layer. Using such a process, the formation of GaAs nanodots with their arms and tunneling junctions beneath them was succeeded, in the form of a two-dimensional array on a substrate (Figs. 20b and c), though the technology is not yet perfect and a complete device has not been fabricated yet. An improved process technology to form GaAs nanodots with arms and multiple tunneling junctions is now under development, where the arms and multiple tunneling junctions are arranged regularly with a smaller pitch of 100 nm or less (corresponding to 1010 oscillators/cm^2). With the improved process technology, we will be able to integrate coupled single-electron oscillators on a chip and proceed from there to develop reaction-diffusion LSIs.

Collision-Based RD Computers

Present digital LSI systems consist of a number of combinational and sequential logic circuits as well as related peripheral circuits. A well-known basic logic circuit is a two-input NAND circuit that consists of four metal-oxide semiconductor field-effect transistors (MOS FETs) where three transistors are on the current path between the power supply and the ground. Many complex logic circuits can be constructed by not only populations of a large number of NAND circuits but also special logic circuits with a small number of transistors (there are more than three transistors on the current path) compared with NAND-based circuits.

A straight-forward way to construct low-power digital LSIs is to decrease the power-supply voltage because the power consumption of digital circuits is proportional to the square of the supply voltage. In complex logic circuits, where many transistors are on the current paths, the supply voltage cannot be decreased due to stacking effects of transistors' threshold voltages, even though the threshold voltage is decreasing as LSI fabrication technology advances year by year. On the other hand, if two-input basic gates that have the minimum number of transistors (three or less) on the current path are used to decrease the supply voltage, a large number of the gates will be required for constructing complex logic circuits.

The Reed–Muller expansion [40,48], which expands logical functions into combinations of AND and XOR logic, enables us to design 'specific' arithmetic functions with a small number of gates, but it is not suitable for arbitrary arithmetic computation. Pass-transistor logic (PTL) circuits use a small number of transistors for basic logic functions but additional level-restoring circuits are required for every unit [52]. Moreover, the acceptance of PTL circuits into mainstream digital design critically depends on the availability of tools for logic, physical synthesis, and optimization. Current-mode logic circuits also use a small number of transistors for basic logic, but their power consumption is very high due to the continuous current flow in turn-on states [15]. Subthreshold logic circuits where all the transistors operate under their threshold voltage are expected to exhibit ultra-low power consumption, but the operation speed is extremely slow [53]. Binary decision diagram logic circuits are suitable for next-generation semiconductor devices such as single-electron transistors [16,51], but not for present digital LSIs because of the use of PTL circuits.

To address the problems above concerning low-power and high-speed operation in digital LSIs, a method of designing logic circuits with collision-based fusion gates, which is inspired by collision-based RD computing (RDC) [6,7], is described. In the following sections, we see a new interpretation of collision-based RDC, especially concerning directions and speeds of propagating information quanta. We also see basic logical functions constructed by collision-based fusion gates, and discuss the number of transistors in classical and fusion-gate logic circuits [60].

Collision-Based Reaction-Diffusion Computing for Digital LSIs

Adamatzky proposed how to realize arithmetical scheme using wave fragments traveling in a RD medium where ex-

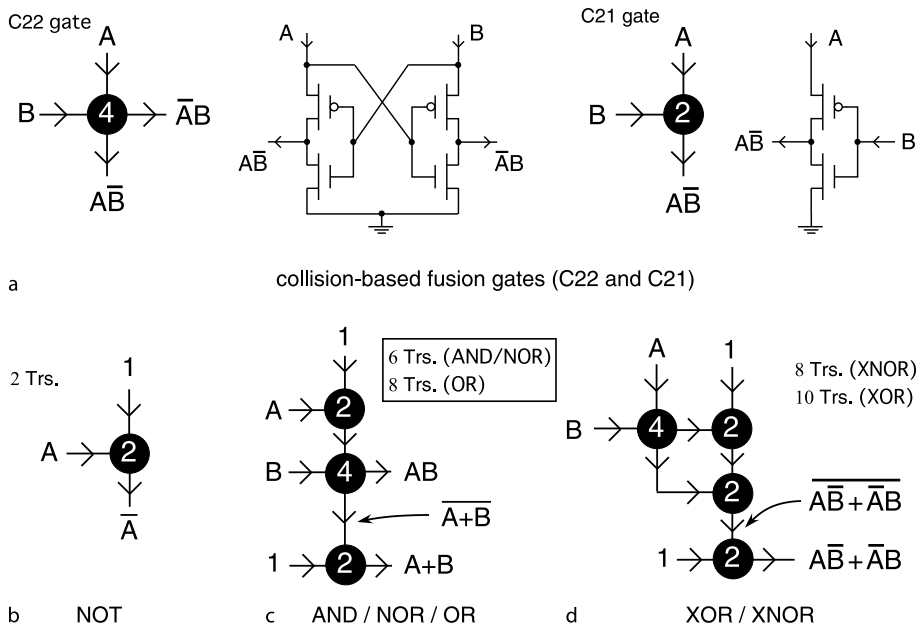

Unconventional Computing, Novel Hardware for, Figure 21
Construction of collision-based fusion gates [60]. a Definition of 2-in 2-out (C22) and 2-in 1-out (C21) gates and their corresponding circuits; b NOT; c AND, NOR, and OR; d XOR and XNOR functions

citable chemical waves disappear when they collide each other [6,7]. His cellular-automaton model mimicked localized excitable waves (wave fragments) traveling along columns and rows of the lattice and along diagonals. The wave fragments represented values of logical variables where logical operations were implemented when wave fragments collided and were annihilated or reflected as a result of the collision. One can achieve basic logical gates in the cellular-automaton model, and build an arithmetic circuit using the gates [6].

The cellular-automaton model for basic logic gates has been implemented on digital LSIs [7]. Each cell consisted of several tens of transistors and was regularly arranged on a 2D chip surface. To implement a one-bit adder, for example, by collision-based cellular automata, at least several tens of cells are required to allocate sufficient space for the collision of wave fragments [6]. This implies several hundreds of transistors are required for constructing just a one-bit adder. Direct implementation of the cellular automaton model is therefore a waste of chip space, as long as the single cell space is decreased to the same degree of chemical compounds in spatially-continuous RD processors.

What happens if wave fragments travel in 'limited directions instantaneously'? Our possible answers to this question are depicted in Fig. 21. Figure 21a shows 2-in 2-out (C22) and 2-in 1-out (C21) units representing two perpendicular 'limited' directions of wave fragments, i. e., North-South and West-East fragments. The number of MOS transistors in each unit is written inside the black circle in the figure. The input fragments are represented by values A and B where A (or B) = '1' represents the existence of a wave fragment traveling North-South (or West-East), and A (or B) = '0' represents the absence of wave fragments. When A = B = '1' wave fragments collide at the center position (black circle) and then disappear. Thus, East and South outputs are '0' because of the disappearance. If A = B = '0', the outputs will be '0' as well because of the absence of the fragments. When A = '1' and B = '0', a wave fragment can travel to the South because it does not collide with a fragment traveling West-East. The East and South outputs are thus '0' and '1', respectively, whereas they are '1' and '0', respectively, when A = '0' and B = '1'. Consequently, logical functions of this simple 'operator' are represented by $\bar{A}B$ and $A\bar{B}$, as shown in Fig. 21a left. We call this operator a collision-based 'fusion gate', where two inputs correspond to perpendicular wave fragments, and one (or two) output represents the results of the collision (transparent or disappear) along the perpendicular axes. Figures 21b to d represent basic logic circuits constructed by combining several fusion gates. The simplest example is shown in Fig. 21b where the NOT function

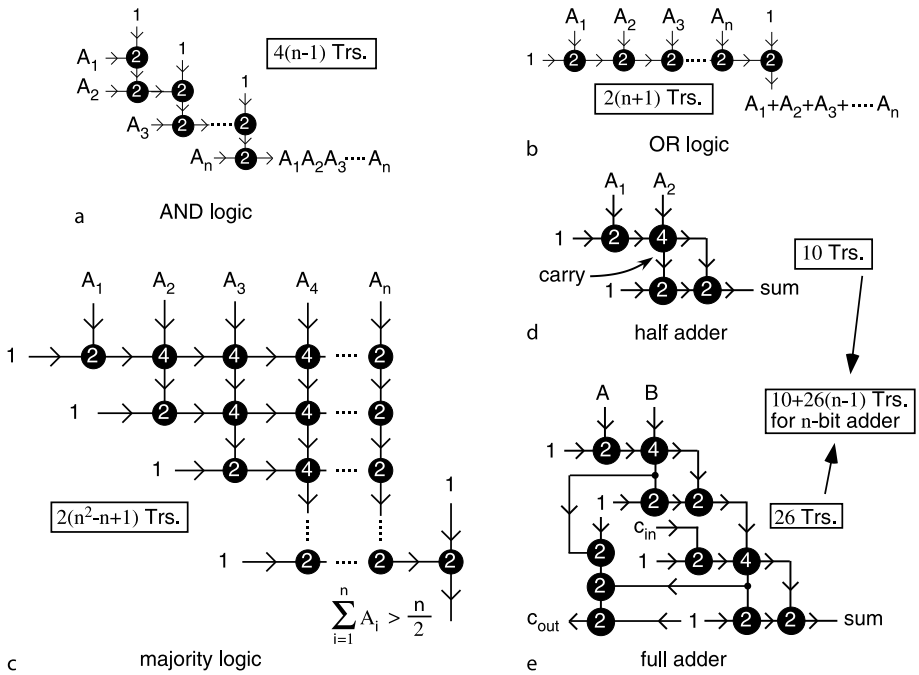

Unconventional Computing, Novel Hardware for, Figure 22
Fusion gate architectures of multiple-input functions [60]; a AND, b OR, c majority logic gates. Half and full adders are shown in d and e, respectively

is implemented by a C21 gate (2 transistors). The North input is always '1', whereas the West is the input (A) of the NOT function. The output appears on South node ($\overline{A}$). Figure 21c represents a combinational circuit of three fusion gates (two C21 gates and one C22 gate) that produces AND, NOR, and OR functions. Exclusive logic functions are produced by three (for XNOR) or four (for XOR) fusion gates as shown in Fig. 21d. The number of transistors for each function is depicted in the figure (inside the white boxes).

A collision-based fusion gate receives two logical inputs (A and B) and produces one (C21) or two (C22) logical outputs; i. e., $A\overline{B}$ for C21, $\overline{A}B$ and $A\overline{B}$ for C22. Unit circuits for C22 and C21 gates receive logical (voltage) inputs (A and B) and produce these logic functions. The minimum circuit structure is based on PTL circuits where a single-transistor AND logic is fully utilized. For instance, in Fig. 21a right, a pMOS pass transistor is responsible for the $\overline{A}B$ function, and an additional nMOS transistor is used for discharging operations. When the pMOS transistor receives voltages A and B at its gate and drain, respectively, the source voltage approaches $\overline{A}B$ at equilibrium. If a pMOS transistor is turned off, an nMOS transistor connected between the pMOS transistor and the ground discharges the output node, which significantly increases the upper bound of the operation frequency. When A = B = '0', the output voltage is not completely zero because of the threshold voltage of the MOS transistors, however, this small voltage shift is restored to logical '0' at the next input stage. Therefore additional level-restoring circuits are unnecessary for this circuit.

Figure 22 shows constructions of multiple-input logic functions with fusion gates. In classical circuits, two-input AND and OR gates consist of six transistors. To decrease the power supply voltage for low-power operation, a small number of transistors (three or less) should be on each unit's current path. Since each unit circuit has six transistors, n-input AND and OR gates consist of $6(n-1)$ transistors ($n \geq 2$). On the other hand, in fusion gate logic [(a) and (b)], a n-input AND gate consisted of $4(n-1)$ transistors, whereas $2(n+1)$ transistors were used in an n-input OR gate. Therefore, in case of AND logic, the number of transistors in fusion gate circuits is smaller than that of classical circuits. The difference will be significantly expanded as n increases. Figure 22c shows fusion gate implementation of majority logic circuits with multiple inputs. Again, in classical circuits, the number of transistors on each unit's current path is fixed to three. For n-bit inputs (n must be an odd number larger than 3), the number of transistors in the classical circuit was $30 + 36(n-3)^2$,

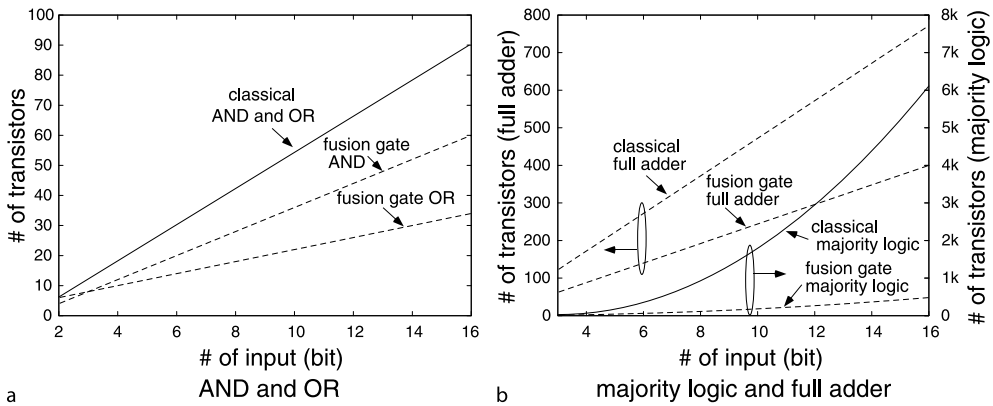

Unconventional Computing, Novel Hardware for, Figure 23
Total number of transistors in classical and collision-based (CB) multiple-input logic gates [60]

while in the fusion gate circuit, it was $2(n^2 - n + 1)$, which indicates that the collision-based circuit has a great advantage in the number of transistors. Half- and full adders constructed by fusion gate logic are illustrated in Figs. 22d and e. The number of transistors in a classical half adder was 22, while it was 10 in a fusion gate half adder (Fig. 22d). For n-bit full adders ($n \geq 1$), the number of transistors in a classical circuit was $50n - 28$, while it was $26(n - 1) + 10$ in a fusion gate circuit (Fig. 22e). Again, the fusion gate circuit has a significantly smaller number of transistors, and the difference will be increased as n increases.

Figure 23 summarizes the comparison of the number of transistors between classical and fusion gate logic. The number of transistors in fusion gate logic was always smaller than that of transistors in classical logic circuits, especially in majority logic gates.

Future Directions

Before starting any computation one should input data-information in the RD medium. A parallel input is an essential feature of an edge-cutting parallel computing architecture. Serial inputs, so common for vast majority of massively-parallel processors, dramatically decrease performance of the computing devices, particularly those operating in transducer mode, where information is constantly fed into the processor (e. g. in tasks of image processing). Experimental RD chemical computers, at least in certain case, may well have analogs of parallel inputs. It has been demonstrated widely that applying light of varying intensity we can control excitation dynamic in BZ-medium [22,27,32,44], wave velocity [49], patter formation [58]. Of particular interest are experimental evidences of light-induced back propagating waves, wavefront splitting and phase shifting [61]; we can also manipulate medium's excitability by varying intensity of the medium's illumination [23]. In fact, optical input of data-information has been already used at the beginning of RD research [34]. This was proved to particularly important in experiments in image processing in BZ-medium-based computing devices [34,45,46,47]. We are not aware of any rigorous experimental results demonstrating a possibility of optical inputs of RD semi-conductor devices there is however a simulation-related evidence of a possibility of optical parallel inputs. Paper [39] discusses particulars of a photo-response, photon-induced generation of electron-hole pairs in *p-n-p-n* devices, depending on primary color components in the stimulating input because elementary processors can also act as color sensors.

There exists a possibility of parallel optical outputs on semiconductor devices. Technologies for integrating optoelectronic devices and electronic circuitry are fully developed, but limited hybrid integration is available commercially at present. An important problem of such integration is that pursuing it involves simultaneous development of sophisticated technologies for optoelectronic devices (III-V semiconductors) and silicon integrated circuits. Indeed, recent development in optoelectronic integrated circuits (OEICs) enables us to implement light-emitting devices (LEDs) on silicon substrate by controlling defects at III-V/silicon interface. For example, Furukawa et al. demonstrated that lattice-matched and defect-free GaPN epilayers can be grown on silicon with a thin GaP buffer layer [29]. The task is enormous and as a practical matter only small scale OEICs have been demonstrated. While the integration levels of III-V OEICs have remained low, the degree of integration in commercial GaAs inte-

grated circuits has reached LSI levels in recent years. These advances offer a route to achieving much higher levels of optoelectronic integration through epitaxial growth of III-V heterostructures on GaAs-based LSI electronics.

Most experimental prototypes of chemical excitable computing devices suffer from difficulties with representation of results of wave interaction. This is because being excited a medium's micro-volume becomes refractory and then recovers back to the resting state. Excitation wave-fronts usually annihilate in the result of collision. Therefore, experimental excitable RD computers require some external devices, like digital camera, to record their spatio-temporal dynamics. Thus, e. g. to compute a collision-free path around obstacles in thin-layer BZ-medium one must record snapshots of BZ-medium's activity and then analyze this series of snapshots to extract results of the computation [11,14]. This is the cost we pay for reusable (because the excitable medium eventually returns to resting state) RD processors. Another option of preserving results of computation may be to employ non-excitable RD media, where a precipitate is formed (or do not formed) in the result of diffusion wave interaction with a substrate (or competition of several wave fronts for the substrate) [9,10,13,25]. Precipitation is an analog of infinite memory. The feature is priceless however makes experimental prototypes simply disposable, in contrast to excitable media the precipitate-forming media can be used just once.

RD semiconductor computers, because they are essentially man-made devices, may allow us to combine reusability and rich space-time dynamics of excitable RD media with low post-processing costs of precipitate-forming RD media. This can be done by embedding a lattice of oscillatory semiconductor elements into a lattice of excitatory semiconductor elements. The excitatory elements (EEs) will form a substrate to support traveling excitation waves while oscillatory elements (OEs) will play a role of rewritable memory. For example, to represent sites of wave-front collision we must adjust an activation threshold of OEs in such manner that front of a single wave will not trigger OEs, however when two or more wave-fronts collide the OEs at the sites of collision are triggered and continue oscillate even when the wave-fronts annihilate.

What computational tasks can be realized in RD semiconductor devices? Most primitive operations of image processing (see overview in [5]), e. g. detection of contour and enhancement, are straightly mapped onto the silicon architecture. Silicon implementation of RD (precipitate formation based) algorithms for computational geometry – Voronoi diagram [13,25,26] and skeletonization [12] – requires embedding of oscillatory elements in the lattice of excitatory *p-n-p-n* devices; the oscillating elements will represent bisectors of a Voronoi diagram and segments of a skeleton.

Universal computation can be realized in RD semiconductor devices using two approaches. Firstly, by employing collision-based mode of computation in excitable media [3], where functionally complete sets of Boolean gates are implemented by colliding waves. In collision-based mode, however we must force the medium to be in a sub-excitable regime which may pose some problems from fabrication point of view. Secondly, we can 'physically' embed logical circuits, namely their diagram-based representations, into the excitable medium [54,57]. In this we employ particulars of photo-response of *p-n-p-n* elements and project the logical circuit onto the medium as pattern of heterogeneous illumination.

Bibliography

1. Adamatzky A (1994) Reaction–diffusion algorithm for constructing discrete generalized Voronoi diagram. Neural Netw World 6:635–643
2. Adamatzky A (1996) Voronoi–like partition of lattice in cellular automata. Mathl Comput Modeling 23:51–66
3. Adamatzky A (1998) Universal dynamical computation in multi-dimensional excitable lattices. Int J Theor Phys 37:3069–3108
4. Adamatzky A (2000) Reaction-diffusion and excitable processors: A sense of the unconventional. Parallel Distrib Comput Theor Pract 3:113–132
5. Adamatzky A (2001) Computing in nonlinear media and automata collectives. Institute of Physics Publishing, Bristol
6. Adamatzky A (ed) (2002) Collision-based computing. Springer, London
7. Adamatzky A, De Lacy Costello B, Asai T (2005) Reaction-diffusion computers. Elsevier, Amsterdam
8. Adamatzky A, Arena P, Basile A, Carmona-Galán R, De Lacy Costello B, Fortuna L, Frasca M, Rodríguez-Vázquez A (2004) Reaction-diffusion navigation robot control: From chemical to VLSI analogic processors. IEEE Trans Circuit Syst I 51:926–938
9. Adamatzky A, De Lacy Costello BPJ (2002) Experimental logical gates in a reaction-diffusion medium: The XOR gate and beyond. Phys Rev E 66:046112
10. Adamatzky A, De Lacy Costello BPJ (2003) On some limitations of reaction-diffusion computers in relation to Voronoi diagram and its inversion. Phys Lett A 309:397–406
11. Adamatzky A, De Lacy Costello BPJ (2002) Collision-free path planning in the Belousov-Zhabotinsky medium assisted by a cellular automaton. Naturwissenschaften 89:474–478
12. Adamatzky A, De Lacy Costello B, Ratcliffe NM (2002) Experimental reaction-diffusion pre-processor for shape recognition. Phys Lett A 297:344–352
13. Adamatzky A, Tolmachiev D (1997) Chemical processor for computation of skeleton of planar shape. Adv Mater Optics Electron 7:135–139

14. Agladze K, Magome N, Aliev R, Yamaguchi T, Yoshikawa K (1997) Finding the optimal path with the aid of chemical wave. Physica D 106:247–254
15. Alioto M, Palumbo G (2005) Model and design of bipolar and MOS current-mode logic: CML, ECL and SCL digital circuits. Springer, Berlin
16. Asahi N, Akazawa M, Amemiya Y (1998) Single-electron logic systems based on the binary decision diagram. IEICE Trans Electron E81-C:49–56
17. Asai T, Nishimiya Y, Amemiya Y (2002) A CMOS reaction-diffusion circuit based on cellular-automaton processing emulating the Belousov–Zhabotinsky reaction. IEICE Trans Fundam E85-A:2093–2096
18. Asai T, Adamatzky A, Amemiya Y (2004) Towards reaction-diffusion computing devices based on minority-carrier transport in semiconductors. Chaos Solit Fractals 20:863–876
19. Asai T, Ikebe M, Hirose T, Amemiya Y (2005) A quadrilateral-object composer for binary images with reaction-diffusion cellular automata. Int J Parallel Emergent Distrib Syst 20:57–68
20. Asai T, De Lacy Costello B, Adamatzky A (2005) Silicon implementation of a chemical reaction-diffusion processor for computation of Voronoi diagram. Int J Bifurc Chaos 15:3307–3320
21. Asai T, Kanazawa Y, Hirose T, Amemiya Y (2005) Analog reaction-diffusion chip imitating the Belousov–Zhabotinsky reaction with hardware Oregonator model. Int J Unconv Comput 1:123–147
22. Beato V, Engel H (2003) Pulse propagation in a model for the photosensitive Belousov–Zhabotinsky reaction with external noise. In: Schimansky-Geier L et al (eds) Noise in complex systems and stochastic dynamics. Proc SPIE 5114:353–362
23. Brandtstädter H, Braune M, Schebesch I, Engel H (2000) Experimental study of the dynamics of spiral pairs in light-sensitive Belousov–Zhabotinskii media using an open-gel reactor. Chem Phys Lett 323:145–154
24. Daikoku T, Asai T, Amemiya Y (2002) An analog CMOS circuit implementing Turing's reaction-diffusion model. Proc Int Symp Nonlinear Theor Appl 809–812
25. De Lacy Costello B, Adamatzky A (2003) On multitasking in parallel chemical processors: experimental findings. Int J Bifurc Chaos 13:521–533
26. De Lacy Costello B, Adamatzky A, Ratcliffe N, Zanin AL, Liehr AW, Purwins HG (2004) The formation of Voronoi diagrams in chemical and physical systems: Experimental findings and theoretical models. Int J Bifurc Chaos 14:2187–2210
27. Flessels JM, Belmonte A, and Gáspár V (1998) Dispersion relation for waves in the Belousov–Zhabotinsky reaction. J Chem Soc Faraday Trans 94:851–855
28. Fukai T (1996) Competition in the temporal domain among neural activities phase-locked to subthreshold oscillations. Biol Cybern 75:453–461
29. Furukawa Y, Yonezu H, Ojima K, Samonji K, Fujimoto Y, Momose K, Aiki K (2001) Control of N content of GaPN growun by molecular beam epitaxy and growth of GaPN lattice-matched to Si(100) substrate. Jpn J Appl Phys 41:528–532
30. Gerhardt M, Schuster H, Tyson JJ (1990) A cellular automaton model of excitable media. Physica D 46:392–415
31. Gravert H, Devoret MH (1992) Single charge tunneling – Coulomb blockade phenomena in nanostructures. Plenum, New York
32. Grill S, Zykov VS, Müller SC (1996) Spiral wave dynamics under pulsatory modulation of excitability. J Phys Chem 100:19082–19088
33. Karahaliloglu K, Balkir S (2005) Bio-inspired compact cell circuit for reaction-diffusion systems. IEEE Trans Circuits Syst II Express Briefs 52:558–562
34. Kuhnert L, Agladze KL, Krinsky VI (1989) Image processing using light-sensitive chemical waves. Nature 337:244–247
35. Kuwamura N, Taniguchi K, Hamakawa C (1994) Simulation of single-electron logic circuits. IEICE Trans Electron J77-C-II:221–228
36. Kumakura K, Nakakoshi K, Motohisa J, Fukui T, Hasegawa H (1995) Novel formation method of quantum dot structures by self-limited selective area metalorganic vapor phase epitaxy. Jpn J Appl Phys 34:4387–4389
37. Kumakura K, Motohisa J, Fukui T (1997) Formation and characterization of coupled quantum dots (CQDs) by selective area metalorganic vapor phase epitaxy. J Crystal Growth 170:700–704
38. Matsubara Y, Asai T, Hirose T, Amemiya Y (2004) Reaction-diffusion chip implementing excitable lattices with multiple-valued cellular automata. IEICE Electron Express 1:248–252
39. Mohajerzadeh S, Nathan A, Selvakumar CR (1994) Numerical simulation of a p-n-p-n color sensor for simultaneous color detection. Sens Actuators A 44:119–124
40. Muller DE (1954) Application of boolean algebra to switching circuit design and to error detection. IRE Trans Electr Comp EC-3:6–12
41. Niedernostheide FJ, Kreimer M, Kukuk B, Schulze HJ, Purwins HG (1994) Travelling current density filaments in multilayered silicon devices. Phys Lett A 191:285–290
42. Oya T, Asai T, Fukui T, Amemiya Y (2002) A majority-logic nanodevice using a balanced pair of single-electron boxes. J Nanosci and Nanotech 2:333–342
43. Oya T, Asai T, Fukui T, Amemiya Y (2005) Reaction-diffusion systems consisting of single-electron circuits. Int J Unconv Comput 1:123–147
44. Petrov V, Ouyang Q, Swinney HL (1997) Resonant formation in a chemical system. Nature 388:655–657
45. Rambidi NG (1998) Neural network devices based on reaction-duffusion media: An approach to artificial retina. Supramol Sci 5:765–767
46. Rambidi NG, Yakovenchuk D (2001) Chemical reaction-diffusion implementation of finding the shortest paths in a labyrinth. Phys Rev E63:0266071–0266076
47. Rambidi NG, Shamayaev KE, Peshkov GY (2002) Image processing using light-sensitive chemical waves. Phys Lett A 298:375–382
48. Reed IS (1954) A class of multiple-error-correcting codes and their decoding scheme. IRE Trans Inform Th PGIT-4:38–49
49. Schebesch I, Engel H (1998) Wave propagation in heterogeneous excitable media. Phys Rev E 57:3905–3910
50. Serrano-Gotarredona T, Linares-Barranco B (2003) Log-domain implementation of complex dynamics reaction-diffusion neural networks. IEEE Trans Neural Networks 14:1337–1355
51. Shelar RS, Sapatnekar SS (2001) BDD decomposition for the synthesis of high performance PTL circuits. Workshop Notes IEEE IWLS 2001 298–303
52. Song M, Asada K (1998) Design of low power digital VLSI circuits based on a novel pass-transistor logic. IEICE Trans Electron E81-C:1740–1749

53. Soeleman H, Roy K, Paul BC (2001) Robust subthreshold logic for ultra-low power operation. IEEE Trans VLSI Syst 9:90–99
54. Steinbock O, Toth A, Showalter K (1995) Navigating complex labyrinths: optimal paths from chemical waves. Science 267:868–871
55. Suzuki Y, Takayama T, Motoike IN, Asai T (2007) Striped and spotted pattern generation on reaction-diffusion cellular automata: Theory and LSI implementation. Int J Unconv Comput 3:1–13
56. Tóth Á, Gáspár V, Showalter K (1994) Propagation of chemical waves through capillary tubes. J Phys Chem 98:522–531
57. Tóth Á, Showalter K (1995) Logic gates in excitable media. J Chem Phys 103:2058–2066
58. Wang J (2001) Light-induced pattern formation in the excitable Belousov–Zhabotinsky medium. Chem Phys Lett 339:357–361
59. Yamada T, Akazawa M, Asai T, Amemiya Y (2001) Boltzmann machine neural network devices using single-electron tunneling. Nanotechnology 12:60–67
60. Yamada K, Asai T, Hirose T, Amemiya Y (2008) On digital LSI circuits exploiting collision-based fusion gates. Int J Unconv Comput 4:45–59
61. Yoneyama M (1996) Optical modification of wave dynamics in a surface layer of the Mn-catalyzed Belousov–Zhabotinsky reaction. Chem Phys Lett 254:191–196
62. Young DA (1984) A local activator-inhibitor model of vertebrate skin patterns. Math Biosci 72:51–58